The Star Formation Histories of Red-Sequence Galaxies

by

Steven Allanson

A thesis
presented to the University of Waterloo
in fulfillment of the
thesis requirement for the degree of
Master of Science
in
Physics

Waterloo, Ontario, Canada, 2009

I hereby declare that I am the sole author of this thesis. This is a true copy of the thesis, including any required final revisions, as accepted by my examiners.

I understand that my thesis may be made electronically available to the public.

Abstract

This thesis addresses the challenge of understanding the typical star formation histories of red sequence galaxies, using linestrength indices, mass-to-light ratios and redshift evolution as complementary constraints on their stellar age distribution. We first construct simple parametric models of the star formation history that bracket a range of scenarios, and fit these models to the linestrength indices of low-redshift cluster red-sequence galaxies. For giant galaxies, we confirm the downsizing trend, i.e. the stellar populations are younger, on average, for lower σ galaxies. We find, however, that this trend flattens or reverses at $\sigma \lesssim 70\mathrm{km\,s^{-1}}$. We then compare predicted stellar mass-to-light ratios with dynamical mass-to-light ratios derived from the Fundamental Plane, or by the SAURON group. For galaxies with $\sigma \sim 70$ $\mathrm{km\,s^{-1}}$, models with a late "frosting" of young stars and models with exponential star formation histories have stellar mass-to-light ratios that are larger than observed dynamical mass-to-light ratios by factors of 1.7 and 1.4, respectively, and so are rejected. The single stellar population (SSP) model is consistent with the Fundamental Plane, and requires a modest amount of dark matter (between 20% to 30%) to account for the difference between stellar and dynamical mass-to-light ratios. A model in which star formation was "quenched" at intermediate ages is also consistent with the observations, although in this case less dark matter is required for low mass galaxies. We also find that the contribution of stellar populations to the "tilt" of the Fundamental Plane is highly dependent on the assumed star-formation history: for the SSP model, the tilt of the FP is driven primarily by stellar-population effects. For a quenched model, two-thirds of the tilt is due to stellar populations and only one third is due to dark matter or non-homology. Comparing to high redshift cluster data, we find again the SSP and quenched models, as well as a model where strangulation begins at intermediate ages after a period of constant star formation, are preferred. They predict the recent faint-end build up of the red sequence, along with observed dwarf-to-giant ratios. Only the SSP model appears to predict the observed M/L evolution, but only if selection effects are carefully modeled.

Acknowledgements

I would like to thank Michael Hudson for his ongoing support and guidance. Honourable mentions go to Michael Balogh, David Gilbank, and Ting Lu. I would also like to thank Sean McGee for fielding my random oddball questions about all things astronomy, without excessive violence.

Dedication

This is dedicated to you, me, her, that guy, and the man behind the curtain; Bill Hicks, George Carlin, Mitch Hedberg, Chris Farley, John Candy, Billy Mays, Farrah Fawcett, Captain Planet, and Cottage Cheese.

Contents

List of Tables

List of Figures

Chapter 1

Introduction

The research presented in this thesis attempts to model the star formation histories of red-sequence galaxies. Specifically, observed absorption linestrength indices of emission-free galaxies in the Shapley Supercluster are fit to spectral synthesis models. Using various assumed star formation history models, we fit these line indices and find associated ages and chemical abundances. Observables are produced and compared to literature, which help narrow down how red-sequence galaxies form in terms of the star formation histories.

In this chapter, a summary of general concepts regarding galaxy formation and evolution is presented. Focus is put on the processes that could quench star formation in a galaxy, and what causes the galaxy to then migrate to the red-sequence. Next, a summary of stellar population synthesis modeling is presented, explaining chemical abundances and enrichment and what drives their evolution in modeling. We will show how we intend to use modeled absorption line indices and various predicted observables as constraints on star formation history. Lastly we discuss the colour-magnitude relation and origin of the red-sequence.

1.1 An Overview of Galaxy Formation and Evolution

In recent years, the vast increase in the precision of cosmological measurements has led to a largely agreed upon cosmological model of the universe. In the late 1990's, two separate teams (Perlmutter et al., 1999; Riess et al., 1998) made precise measurements of the luminosities and redshifts of distant supernovae and concluded that the universe is accelerating with time. This led to the postulate that the energy density of the universe

is dominated by a dark energy, essentially acting as a pressure which counteracts gravity. Further precision measurements of the fluctuations in the temperature of the microwave background (Komatsu et al., 2009) combined with large scale clustering of galaxies (Cole et al., 2005; Tegmark et al., 2004) and weak lensing measurements of the cosmological shear (Hoekstra et al., 2006) have complemented each other to come to the consensus of a Λ Cold Dark Matter (ΛCDM) universe. In this model, while the dark energy is the dominant energy contribution to the universe, the mass density is dominated by cold dark matter. In this model, the initial perturbations in the density of the universe cause the dark matter to collapse into small halos at high redshift. These small halos gradually merge with each other to build up larger structures 'hierarchically' (Toomre, 1977; White & Rees, 1978). However, the processes which cause the baryonic material to form into the galaxies we see today still contain some mysteries. This thesis is an attempt to understand some of these processes.

The fundamental property of baryonic matter that causes it to behave differently from dark matter is the ability to undergo radiative cooling. During the process of collapse, dark matter halos erase their substructure while the baryonic material is shock heated to the virial temperature. However, unlike dissipationless dark matter, the baryonic material can dissipate some of this energy through the emission of energetic photons. If this radiative cooling proceeds fast enough, then the baryons will contract to the centre of the dark matter potential well. The infalling gas is eventually halted by the conservation of angular momentum and forms a rotationally supported disk of gas near the centre of the dark matter halo. Some of this gas further cools and fragments into stars. The process of radiative cooling naturally leads to the formation of spinning disks of stars and gas like those observed as spiral galaxies (Fall & Efstathiou, 1980).

The formation of these disk galaxies at the centres of the dark matter halos occurs only if the baryons can radiate away their kinetic energy faster than the halo collapses. The radiative cooling timescale is largely determined by two things: the virial temperature of the gas, i.e. how much energy it originally contains, and the cooling rate, or how quickly it loses that energy. The virial temperature is uniquely determined by the total mass of the halo and the redshift at which that halo collapsed (White & Rees, 1978). While the cooling rate has a strong temperature and gas metallicity dependence, the dominant form of cooling for most dark matter halos is direct line cooling following collisional excitation or ionization (Blumenthal et al., 1984).

In small halos, those with virial temperatures of $T < 10^4$ K (Blumenthal et al., 1984), the gas particle collisions do not have high enough energy to ionize hydrogen, and the cooling rate drops to almost zero. Most galaxies are formed initially in halos with virial temperatures of $10^4 < T < 10^6$ K, where the cooling is very efficient. Unfortunately the

efficiency of their expected cooling, coupled with the cosmological model which forms small halos first, predicts that all the gas is completely cooled in these low mass objects at high redshift and that the luminosity of the universe should be dominated by dwarf galaxies. The fact that these predictions are not observed is known as the 'overcooling' problem or 'cooling catastrophe' (Larson, 1974; White & Rees, 1978).

It appears that the solution to the 'overcooling' problem is additional, unaccounted for source of heating, or energy injection. When the gas initially cools, some of it will form stars. Not long after the formation of these first stars, the most massive ones will use all their available fuel and explode in a supernova. The energy from this supernova explosion is transferred into the surrounding gas either by direct heating or from blowing out the gas in large winds. For this gas to cool and form additional stars it must radiate not only the energy from its initial shock heating but also this additional supernova related energy. Some of this gas will be completely blown out of the galaxy and this preferentially happens in the lowest mass galaxies, because they don't have potential wells as significant as more massive galaxies. This reduces the efficiency of star formation in the lowest mass halos and resolves the 'overcooling' problem. This model has additional support in that it explains the mass metallicity relations of galaxies (Dekel & Silk, 1986).

For extremely massive halos, like galaxy clusters and groups where the virial temperatures are $T > 10^6$ K (Blumenthal et al., 1984), the cooling is dominated by the relatively inefficient process of bremsstrahlung radiation. For these halos, the cooling timescale is much larger than the dynamical timescale for the gas as a whole. However, because bremsstrahlung radiation is strongly density dependent, the cooling timescale is actually very short at the centres of the massive clusters. This implies that gas should cool at the centre of galaxy clusters in significant quantities in so-called 'cooling flows' (Fabian, 1994). This predicts that at the centre of galaxy clusters there should be extremely massive galaxies which are actively forming stars at a high rate. However, while the centres of clusters do have massive galaxies, for the most part these galaxies are not forming stars and are less massive than predicted (Fabian, 1994; Edwards et al., 2007). This has led to the suggestion that feedback from the massive black holes at the centre of these galaxies is regulating the gas cooling by injecting energy into the surrounding gas (Schawinski et al., 2006). More generally, the recently discovered correlation between the size of the bulge of a galaxy and the size of its central black hole (Ferrarese & Merritt, 2000; Tremaine et al., 2002) has suggested that energy injection from the black hole may limit the size of all massive galaxies. Indeed, in some scenarios star formation is quenched in galaxies through merger-induced black hole growth and subsequent AGN jet feedback (Hopkins et al. 2006). The merger causes a morphological transformation from two disk galaxies to a single triaxial elliptical galaxy (Toomre & Toomre, 1972; Barnes & Hernquist, 1992), and

the future gas for star formation is blown out of the halo causing the resultant galaxy to be a non-star forming elliptical galaxy.

However, this picture implies that morphological transformations occur at the same time as the cessation of star formation. While observations at low redshift largely find that spiral galaxies are star forming and spheroidal galaxies are non-star forming (Blanton et al., 2003; Baldry et al., 2004), this is not so clear at higher redshift. Indeed Poggianti et al. (1999), have shown that the morphological transformation may occur after the galaxy stops forming stars. For this reason many researchers have suggested that environmental processes which remove gas for future star formation but do not affect the morphological makeup of the galaxy are principally responsible for causing galaxies to stop forming stars. One physical mechanism for removing the gas from the galaxies is ram pressure stripping (Gunn & Gott, 1972). Essentially when a galaxy falls into a more massive halo, the gas in the main halo causes a drag force on the gas in the smaller halo. If the galaxy's self gravity is not strong enough to resist this drag force then the gas is removed. In one popular form of this ram pressure stripping, 'strangulation' (Larson et al., 1980; Balogh & Morris, 2000), the infalling galaxy is able to retain its cold gas, but its more loosely held hot gas halo is removed. This delays the timescale over which the star formation is truncated, because new gas is not able to cool and replenish the cold gas supply. In these types of scenarios, the morphological transformation would be caused later by either disk fading, disk instabilites or subsequent mergers.

Evidence of these processes which shape the star formation histories of galaxies can be found in their spectra, In this thesis, we wish to focus our efforts towards those galaxies whose star formation has ceased, and are thus currently passively evolving. These galaxies are predominantly red and of early-type (E+S0). Their passive evolution leaves essentially an archaeological history of their stellar make-up, retaining much information about their origins. It is this that we wish to investigate in this thesis.

1.2 Overview of Stellar Population Studies

We wish to fit stellar population models to absorption line indices of sets of red-sequence galaxies using assumed star formation histories, to understand their age distributions and chemical abundances. Modern stellar population models are computed using evolutionary population synthesis (EPS) of spectral and photometric properties of stellar populations (Maraston, 1998). The main goal in this type of study is to model systems which cannot be resolved to individual stars easily. This can be used to narrow down ages of the unresolved stellar populations, as well as to understand their chemical abundances and model

their star formation histories. The most notable models to date are those of Bruzual & Charlot (2003) and Maraston (1998, 2005). These studies employ the Simple, or Single Stellar Population (SSP) model which assumes a single age and metal abundance. These are calibrated with globular clusters because they are the simplest stellar systems with well known ages and abundances (Maraston, 2003, 2005). These calibrations are required because of some intrinsic assumptions required. For example, the initial mass function (IMF) (the distribution of mass in the population), is usually of a power-law type with a 'knee' at a certain mass. This knee mass is debated and strongly affects predicted mass-to-light ratios. These calibrated SSP models can then be applied to more complex systems such as galaxies. Briefly, there are 2 main components to generating a set of stellar population models. First, stellar evolutionary tracks are required to follow the evolution of chemical content, luminosities, temperatures, and surface gravities through the stellar phases (Main Sequence, Red Giant Branch, Asymptotic Giant Branch, etc) as a function of mass and age. Many discrepant sets of tracks exist in the literature, which is evidence of the ongoing debate. Second, stellar model atmospheres are required to link the parameters generated by the stellar tracks to flux (Maraston, 2003). A stellar atmosphere is defined as the outer stellar layers where the optical depth $\tau < 1$, or optically thin. These layers define the emitted flux and subsequent absorption features, and thus an integrated spectral energy distribution (SED) can be generated for the whole modeled stellar system. Recent works present these SEDs in isochrones of given metallicity over a span of ages, which can be interpolated and fit to data.

This procedure has been used and refined for over 30 years, beginning with the pioneering work of Crampin & Hoyle (1961); Tinsley (1968) in using broadband colours to narrow down ages of extragalactic stellar systems. This was rudimentary, although it laid the groundwork for much more complex stellar population synthesis models. More recently, the studies of Thomas et al. (2005) have generated Lick indices for various non-solar chemistries. Using observed spectra, it is these Lick indices to which we wish to compare. Next we discuss the study of stellar absorption lines, and their application to our star formation history study.

1.2.1 Stellar Absorption Line Studies

Broadband colours are not good discriminants of stellar populations because of the age-metallicity degeneracy (Worthey, 1994). These degeneracies can be broken by using stellar absorption lines (Worthey, 1994; Thomas et al., 2003). Recent results suggest that metallicity (proportion of elements other than H, He, relative to the sun), α-enhancement (proportion of α-elements (N, O, Mg, Ca, Na, Ne, S, Si, Ti) to Fe peak elements (Cr, Mn,

Fe, Co, Ni, Cu, Zn), relative to the sun - see Equation 1.1) and age vary along the mass or velocity dispersion sequence (Caldwell et al., 2003; Nelan et al., 2005; Thomas et al., 2005), and also vary as a function of environment (Thomas et al., 2005; Smith et al., 2006, 2009b).

$$\left[\frac{Z}{H}\right] = \log\left(\frac{Z}{H}\right) - \log\left(\frac{Z}{H}\right)_{\odot} \;\; ; \;\; \left[\frac{\alpha}{Fe}\right] = \log\left(\frac{\alpha}{Fe}\right) - \log\left(\frac{\alpha}{Fe}\right)_{\odot} \tag{1.1}$$

A limitation of the above analyses is that, in general, the absorption line indices are sensitive only to weighted mean stellar age, with a weighting that strongly favours the most recent star formation (Serra & Trager, 2007). The indices provide only weak information about the range of stellar ages within a galaxy. For convenience, then, stellar population ages are often quoted as the equivalent age of a Single Stellar Population. In practice, other scenarios have been studied. For example, Trager et al. (2000) considered "frosting" models in which a small (few percent) "icing" of young stars on top of a "cake" of older stars yields a young luminosity-weighted age; Thomas et al. (2002, 2005) modeled star formation histories as a Gaussian in age; Bell et al. (2003) assume an exponential star formation history; Kauffmann et al. (2003) model SDSS galaxies as a combination of an exponential with small bursts; and Harker et al. (2006) considered models in which star formation starts early and is later quenched. In terms of predicting the line indices, these scenarios are largely, but not completely, degenerate, as we will show in Section 3.2.1.

However, it may be possible to break these degeneracies using other, complementary, observations. One approach is via chemical abundances: because different elements are produced by different progenitors at various times, it is possible (in principle) to use the abundances as a clock (e.g. Thomas et al., 2005). In practice, however, there are a large number of unknowns (masses of progenitors, yields, gas inflows and outflows) which render the quantitative conversion of element abundances into time-scales problematic. An alternative approach is to compare the predictions of various star-formation history scenarios against other observational relations besides line indices. At low redshifts, the observables include the slope of the colour-magnitude relation (hereafter CMR), the tilt of the Fundamental Plane (hereafter FP) and the scaling of mass-to-light ratios with mass or velocity dispersion. At higher redshift, one can compare the predictions for the evolution of the zero-point, slope and scatter of the CMR and FP, and of the red-sequence dwarf-to-giant ratio.

In this thesis we fit the observed linestrength indices adopting six generic models of the star formation history. Previous studies (Trager et al., 2000; Bernardi et al., 2005) find velocity dispersion to be the "driving parameter" of stellar populations. Smith et al. (2009a),

using the same spectroscopic data as in this work, not only confirm velocity dispersion to be the primary parameter of stellar populations, but find *no* additional dependence of the stellar populations on stellar mass. Therefore, for each model we assume a mean scaling and intrinsic scatter in metallicity, α-enhancement and "age", all assumed to be functions of velocity dispersion. Here, "age" is some parameter related to the timescale of star formation, the definition differing from model to model. Having constrained the scalings via the line strength data, we generate synthetic clusters using the stellar population parameters to determine mass-to-light ratios, colours, magnitudes etc. For these synthetic clusters, we construct the CMR and FP relations and compare these to observational data from low redshift rich clusters, under the assumption that these relations are universal for rich clusters (López-Cruz et al., 2004; McIntosh et al., 2005).

1.2.2 Colour-Magnitude Relation

The colour-magnitude relation is a strong indication of a galaxy's current state of star formation. It relates the general colour of the galaxy with its luminosity, and Figure 1.1 shows the general picture of the CMR. Galaxies which are currently star forming appear much bluer than those that are not, and in general reside in the 'blue cloud'. This relative blue colour is caused by an abundance of young, luminous blue stars. Figure 1.2 shows the evolution of a synthetic spectral energy distribution (SED) for a galaxy with a single burst of star formation (Sparke & Gallagher, 2000). Immediately following the star burst, we see characteristic absorption lines of O and B stars from core helium burning, indicative of very recent star formation. When star formation is shut off (observable even only after $\sim$ 100Myr), galaxies quickly migrate through the 'green valley' (inferred from the apparent low density of galaxies here) to the tight 'red-sequence'. Figure 1.2 shows the relative reddening of old populations. Very little evolution can be seen in colour between even a 1Gyr old burst and a 10Gyr old burst. This is the origin of the red-sequence. The Balmer lines ($H\delta, H\gamma, H\beta$) show strong evolution between these ages however and can be used to distinguish ages of old populations. It is also important to note here that early-types, namely elliptical galaxies, have a characteristic lack of luminous blue stars, which indicates an important correlation between morphology, colour, and evolutionary stage. This correlation may be coincidental, or it more likely indicates that a morphological transformation and the cessation of star formation occur around the same time.

It is this tight red-sequence in which we are interested. Can we exploit this evident correlation to further understand their star formation histories? The CMR has been studied extensively and will be discussed further in Section 5.2 as a method to help distinguish star formation history models.

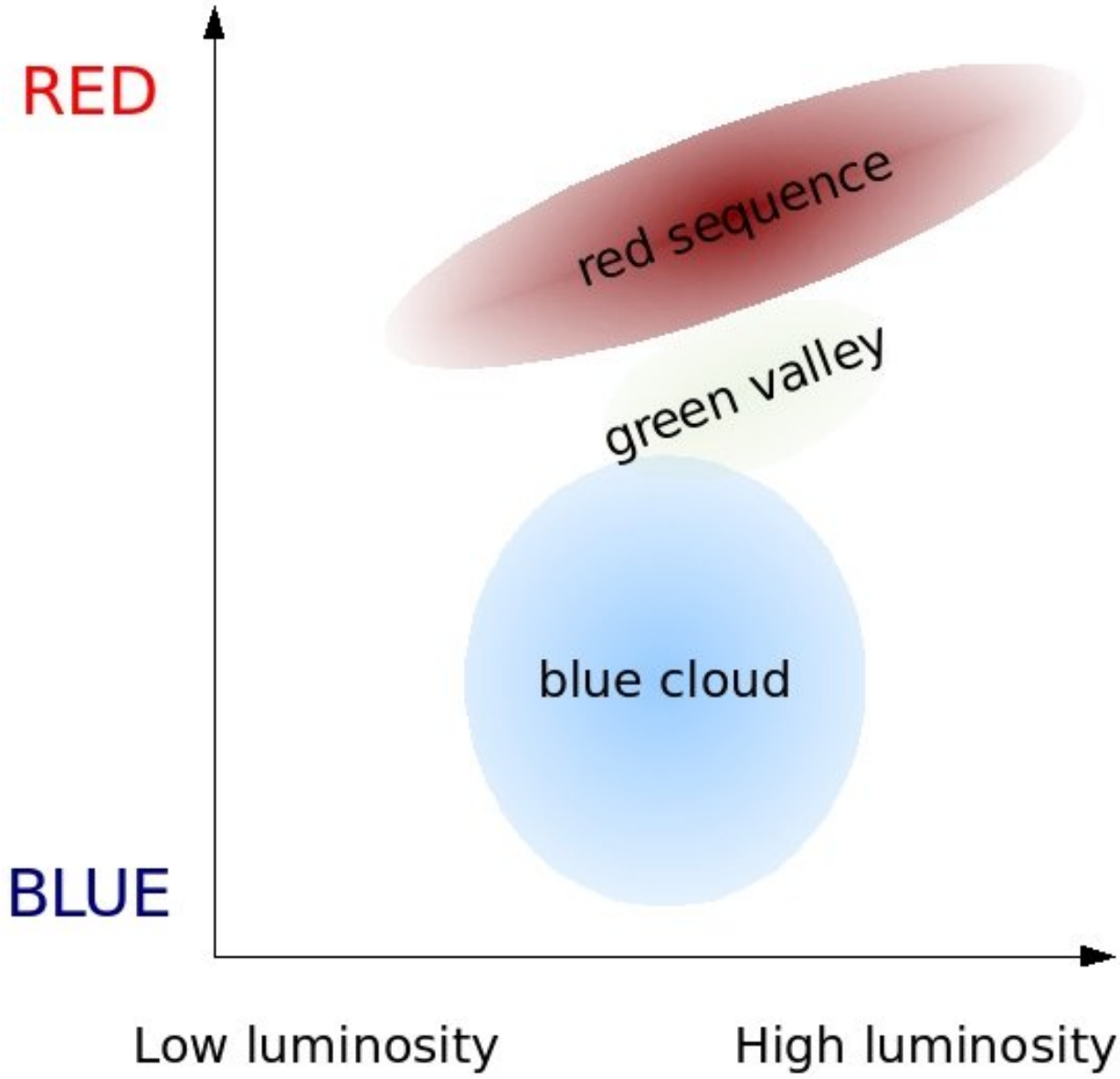

Figure 1.1 General picture of the colour-magnitude relation, relating a galaxy's relative colour with its luminosity. Young star-forming galaxies exist in the blue cloud. Shortly after star formation shuts off, they migrate quickly through the green valley to the red-sequence. This sequence hosts all non star forming early-type galaxies.

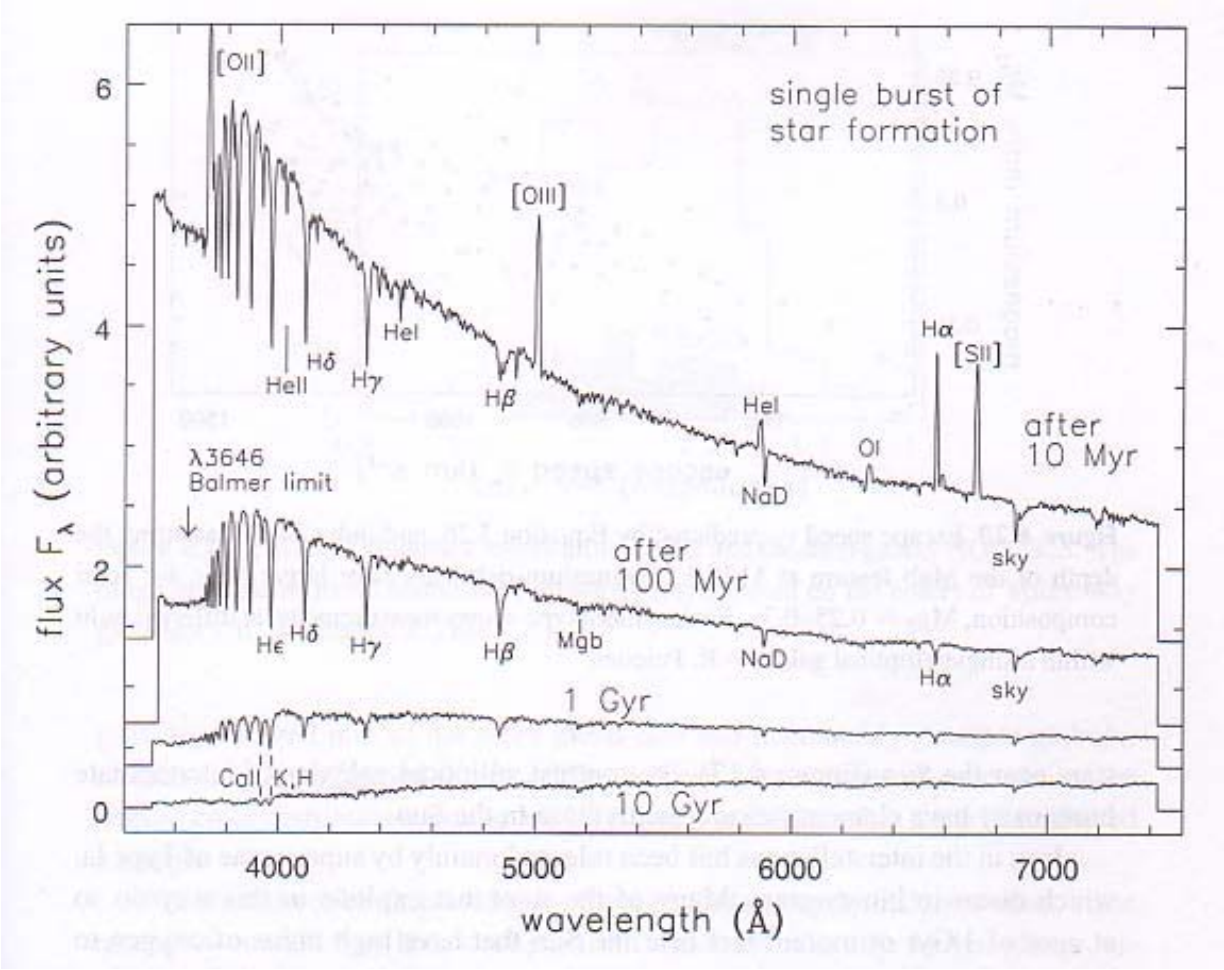

Figure 1.2 Temporal evolution of a synthetic spectral energy distribution of a galaxy with a single burst of star formation (Figure 6.19 Sparke & Gallagher, 2000). Immediately following the star burst, the SED is heavily weighted towards the blue, indicative of O and B star helium core burning. As time progresses, the colour reddens. After 1Gyr, very little evolution is seen in colour, although the Balmer lines evolve strongly. This is the origin of the red-sequence.

Through the so-called Faber-Jackson relation (Faber & Jackson, 1976), which relates velocity dispersion (σ) and magnitude of early-types, the CMR may also be represented as a colour-σ relation. The velocity dispersion of a galaxy is the characteristic broadening of absorption features due to the random motions of stars within, and is also a proxy for mass.

Red-Sequence Galaxies

Red-sequence galaxies (RSGs) dominate the stellar mass in clusters and comprise $\sim 70\%$ (Bell et al., 2003) of the stellar mass in the Universe. However, other than the fact that the *bulk* of their stellar population is older than ~ 1 Gyr, a detailed understanding of their star formation histories remains elusive. RSGs follow a tight colour-magnitude relation (Sandage & Visvanathan, 1978; Bower et al., 1992) and scaling relations such as the Fundamental Plane (described below) (Dressler et al., 1987; Djorgovski & Davis, 1987) with little scatter. At the same time, the dependence of the colours on magnitude suggests that there are indeed variations in their stellar properties as a function of luminosity or a mass-related parameter such as stellar mass or velocity dispersion. Variations in the stellar populations would also affect the "tilt" of the Fundamental Plane with respect to the virial scaling, although the degree to which the tilt is due to stellar populations compared with dark matter (DM) and non-homology remains hotly debated (Prugniel & Simien, 1996; Pahre et al., 1998; Gerhard et al., 2001; Trujillo et al., 2004; Cappellari et al., 2006; La Barbera et al., 2008).

The Fundamental Plane is a scaling relation of early-type galaxies between their effective surface brightnesses, effective radii and velocity dispersions. As I will discuss below, there is a strong correlation between morphology and colour, and thus RSGs also follow this scaling relation closely. The fundamental plane was first discovered by Dressler et al. (1987); Djorgovski & Davis (1987), and later studied by Bender et al. (1992) who define a three-dimensional κ-space as an orthogonal coordinate system for this plane, each a linear combination of the 3 parameters. The existence of this plane implies that early-types are well-virialized, their structures vary systematically along the plane, and their stellar populations are constrained by age and metallicity (Renzini, 2006).

Observationally, the selection of red-sequence members has a strong correlation between morphology, colour, and spectrum. They are (obviously) red in colour, are mostly early-type galaxies (E+S0), and mostly emission-free. However this overlap is not complete, and can impose selection effects in analysis. The review of Renzini (2006) outlines the properties of a sample of ~ 123000 galaxies from the Sloan Digital Sky Survey (SDSS) in the local universe with $z < 0.08$, selected by each of these three criteria and their overlap. This is

Table 1.1. Early-Type Galaxy Selection Comparison[a]

	Morphology	Colour	Spectra
Morphology	37151	70%	81%
Colour	58%	44618	87%
Spectra	55%	70%	55134

[a]Table 1, Renzini (2006). Percentages show number which satisfy both criteria. See text.

reproduced verbatim in Table 1.1 (Table 1 Renzini, 2006). The number of galaxies which meet each criterion lie on the diagonal. Off the diagonal, the percentages represent those galaxies which satisfy two criteria. For example: out of the 37151 morphologically selected early-type galaxies, 70% of those also satisfy the colour criterion; out of the 44618 selected by colour, only 58% of those also satisfy the morphological criterion. The clear fact that the range of selected galaxies spans from ~ 37000 to ~ 55000, is particularly worrisome, as this suggests these specific criteria, although similar, cannot be easily compared without bias. It is clear that these selection criteria are not identical, and it is important to recognize this selection effect in any evolutionary analysis. Furthermore, the correlations between these criteria may weaken with increasing redshift. These biases will be discussed further in Section 5.4 in terms of progenitor bias at high redshift.

1.3 Structure of Thesis

An outline of this thesis is as follows: Chapter 2 describes the spectroscopic and photometric data sets to which we will fit the stellar population models with assumed star formation histories, and compare the predictions. Section 3.1 describes said models of star formation history. The results of the fits to these models are presented in Section 3.2. Having fixed the parameters of the models with the spectroscopic data, we create synthetic clusters based on these models in Section 3.3 and compare these to dynamical mass-to-light ratios, colours, and the Faber-Jackson and Fundamental Plane relations in Chapter 4. The goal here is to distinguish which models provide a good fit to predictions, and which do not. We discuss the effect of systematics, the IMF and of dark matter on our results in Section 4.5.

We explore the evolution of the CMR and mass-to-light ratios in Chapter 5, by increasing the lookback time of our modeled synthetic clusters and comparing to high redshift observations. We discuss the impact of our results on derived stellar mass densities, the tilt of the FP, and red-sequence build-up in Chapter 6. We summarize the results in Chapter 7, and discuss possible future work.

Throughout this thesis, we assume the following cosmological parameters: $(\Omega_M, \Omega_\Lambda, h) = (0.3, 0.7, 0.7)$.

Chapter 2

Data

In this work, we will make use of two datasets for the RSG population in rich clusters. We assume that RSG populations in rich clusters are universal, in the sense of having the same distribution of star-formation histories at a given RSG mass. Absorption linestrength data from deep observations of the RSGs in three rich clusters in the Shapley supercluster are used to derive the ages and metallicities of the RSG population. The resulting predicted colours, magnitudes and Fundamental Plane parameters for the RSG population are compared to data in the Coma cluster.

2.1 Linestrength Data from Cluster Galaxies in Shapley Concentration

The Shapley cluster sample consists of ~ 180 R < 18 emission-free cluster galaxies (Smith et al., 2007) that cover a wide range in central velocity dispersion ($38\,\mathrm{km\,s^{-1}} < \sigma < 313\,\mathrm{km\,s^{-1}}$). There is no morphological selection in this dataset: the only selection is on Hα emission, and this is strongly correlated with colour: $\sim 99\%$ of the emission-free galaxies are red. Furthermore, red-selection and morphology are tightly correlated: for example, only $\sim 20\%$ of NFPS galaxies with $\sigma > 70$ km s^{-1} are types Sa or later (Hudson et al. 09, in preparation). Finally, we note that nearly all of the galaxies in the Shapley cluster sample lie within half the virial radius ($r_{200}/2$) of the centre of one of the three rich clusters (A3556, A3558, A3562) in the supercluster.

The Lick linestrength indices were measured from 8-hour, high signal-to-noise ratio (~ 60 Å^{-1}) spectra, obtained with the AAOmega instrument at the 3.9m Anglo-Australian

Telescope. The spectra were obtained through a 1" radius fibre, corresponding to a physical radius of 0.95 kpc. In this work, we use six Lick linestrength indices (three Balmer indices and three metallic indices) to measure age-related quantities and metallicities, as discussed in Section 3.2 below.

2.2 Coma Cluster Galaxy Data

We will compare predictions from our models to photometric data for 218 galaxies in the Coma Cluster from SDSS DR 6 (Adelman-McCarthy, 2008) and the Two Micron All Sky Survey (2MASS) (Skrutskie et al., 2006) with measured velocity dispersions from the literature. We compare with Coma rather than Shapley itself because no published photometry is available for Shapley, whereas a large range of wavebands is available in Coma (u through K). We note that the Coma cluster is of similar richness to the Shapley clusters, and López-Cruz et al. (2004) have shown that for Abell clusters, the cluster-to-cluster dispersion in CMR colour (at the characteristic luminosity L_*) is only 0.05 in $B-R$. Moreover, the CMR of Coma is typical, deviating by no more than 0.05 mag from the average relation. Figure 2.1 compares the linestrength indices from the homogeneous National Optical Astronomy Observatory Fundamental Plane Survey (NFPS) (Nelan et al., 2005). There is no significant difference between the index-σ relations of the two clusters.

Derived photometric parameters in Coma include half-light radii, surface brightnesses within the half-light radius, and total magnitude measured in the SDSS r-band. These parameters have been corrected for the effects of seeing by fitting a model using GALFIT (Peng et al., 2002) and deriving corrections to observed values from the difference between the seeing-convolved model and the unconvolved model. In order to compare colours with ages and metallicities predicted from the Shapley linestrengths, we measure the colours within a 2" radius aperture corresponding to a physical aperture of 0.97 kpc, which matches the 1" aperture of the AAOmega data in Shapley. (Shapley is approximately twice as distant as Coma.) These aperture magnitudes are corrected for seeing in the same way as described above. Data are k-corrected using formulae from Frei & Gunn (1994), and corrected for Galactic extinction using Schlegel et al. (1998). Finally, because there is evidence for gradients in the stellar populations as a function of cluster-centric radius (Smith et al., 2006, 2009b), we limit fits to Coma galaxies within $r_{200}/2$ (i.e. within 1.24 Mpc, 0.71') of the cluster centre.

In order to model stellar masses, as well as to calculate aperture corrections for the Shapley data, we will require the relationship between effective radius and velocity dispersion. This relationship in Coma is shown in Figure 2.2. We find that a broken power-law

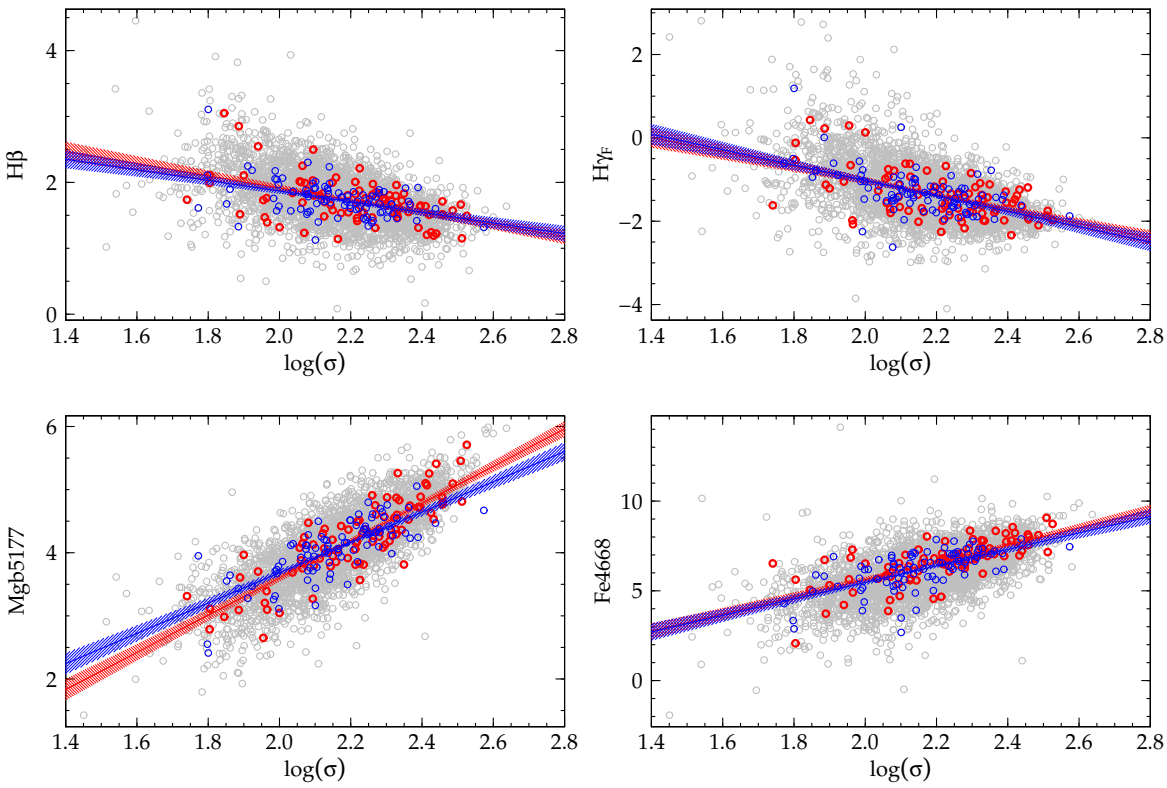

Figure 2.1 Linestrength-σ relations from the NFPS sample for Coma (blue) and the Shapley clusters (red). NFPS data for other clusters are shown in grey. In all cases, galaxies within 0.5 Mpc of the cluster centre are used. There is no significant difference between Coma and Shapley clusters.

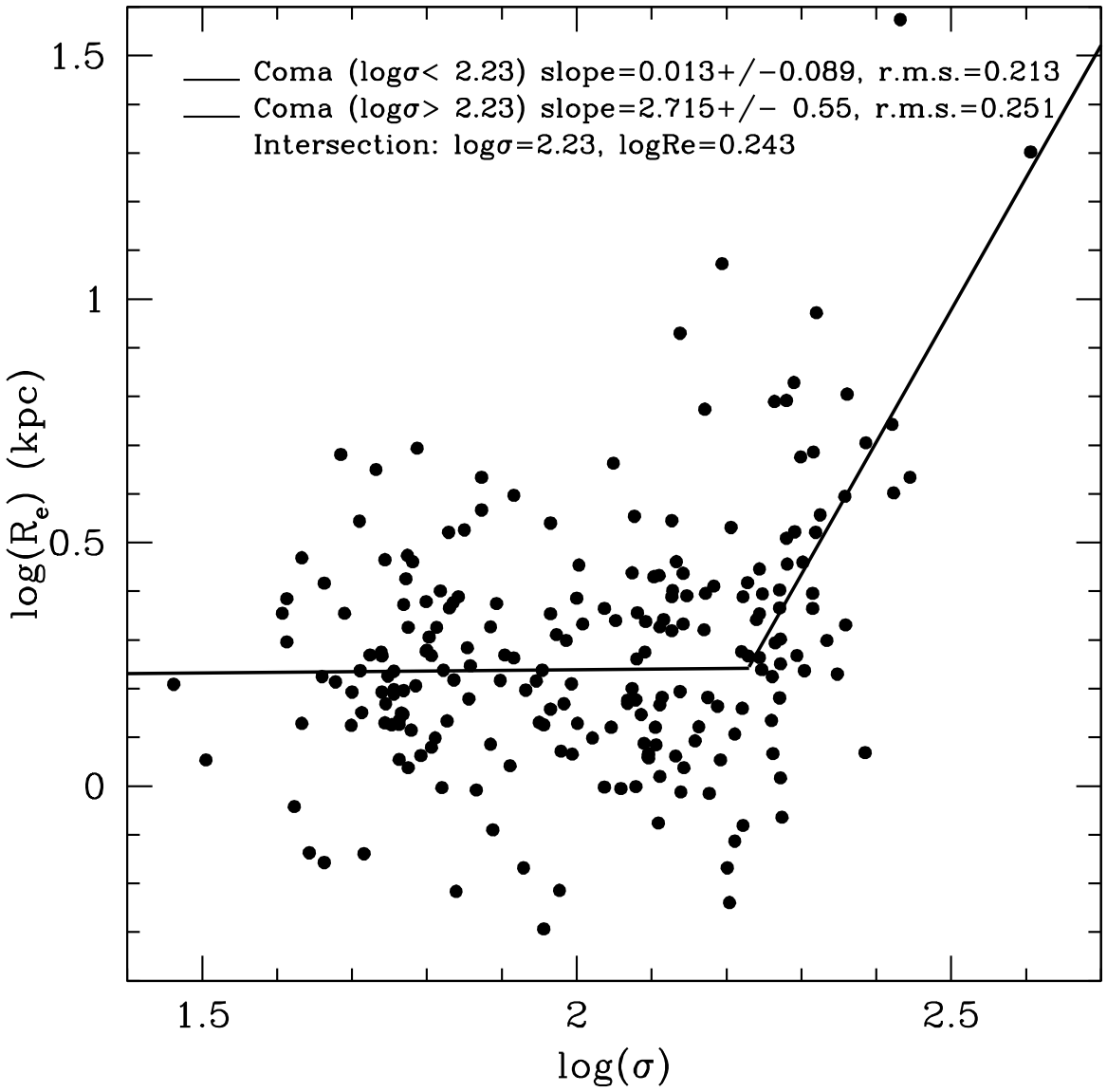

Figure 2.2 Coma $\log(R_e) - \log(\sigma)$ relation. A broken power law (Equation 2.2) was fit to Coma galaxies with cluster-centric radius less than $r_{200}/2$ (filled circles) to match the Shapley sample.

is required to fit the data:

$$\begin{aligned} \log R_e &= 0.013 \log \sigma + 0.21; \qquad \log(\sigma) < 2.23 \\ \log R_e &= 2.715 \log \sigma - 5.81; \qquad \log(\sigma) > 2.23 \end{aligned} \tag{2.1}$$

where R_e is in units of kpc and σ is in units of km/s. The break in R_e is closely related to the well-known break in the surface brightness behavior (Kormendy, 1985), and has been seen in the Faber-Jackson relation (Matković & Guzmán, 2005) and the $R_e - L$ relation Hyde & Bernardi (2009a). The dispersion in $\log(R_e)$, is 0.213 for $\log(\sigma) < 2.23$, and is 0.251 for larger values. The scatter at the low-σ/faint end is comparable to that found at fixed luminosity for the SDSS for faint early-type galaxies; for comparison (Shen et al., 2003) find a dispersion $\gtrsim 0.22$ in $\log(R_e)$ for $M_r > -19$.

Chapter 3

Theory and Models

3.1 Synthetic Linestrengths for Galaxies with Complex Star Formation Histories

Our goal is to extend the SSP analyses of previous work to more complex star formation histories (CSFHs). A CSFH model can be generated by convolving the SSP response with the star formation rate. Here we combine SSP SEDs (Maraston, 1998, 2005) with $\alpha-$enhanced Lick-index absorption linestrengths (Thomas et al., 2003, 2004, together hereafter the TMBK models) to construct linestrength indices for CSFHs. Specifically, the TMBK line indices are based on SSP models. To obtain predictions for complex star formation scenarios, we reconstruct the fluxes in the sidebands and in the central (absorption) band for each step of star formation. By integrating these fluxes over all time steps, appropriately weighted, we can produce a set of indices for any formation scenario. A similar method applies to mass-to-light ratios.

The range of possible star formation histories is clearly large and highly uncertain. Here we consider six simple star formation scenarios that are intended to bracket more complicated, realistic scenarios. All but one of the models we consider have a single age-related quantity, whose definition depends on the specific model detailed below. The exception is the Old SSP model, which has a single fixed age. Note that "ages" from Lick indices have poor age sensitivity at old ages, so it is impossible to discriminate, for example, an old instantaneous burst from an old burst of the same age, but with a short duration of 1 Gyr. The models,abbreviations, and methods for generating mock line indices are as follows:

- Old SSP (hereafter OSP): a single burst of star formation at a fixed age of 13 Gyr. The line indices are generated as in the SSP model, fixing the formation start time.
- Single Stellar Population (SSP): a single burst of star formation, with fitted age $t_{\rm SSP}$.
- Exponential star formation rate (EXP): star formation begins 13 Gyr ago, ends 0.1 Gyr ago, with a fitted exponential decay parameter τ.
- "Abruptly" Quenched (AQ) star formation: a model with constant star formation beginning 13 Gyr ago, and an abrupt truncation of star formation at a fitted lookback time, $t_{\rm AQ}$.
- A 2-component "frosting" model (FR) consisting of a dominant (98% by mass) 13 Gyr SSP and a secondary (2% by mass) burst with fitted age $t_{\rm FR}$.
- A "Strangulation" model (STR): a quenched (constant SFR) model beginning 13 Gyr ago up to fitted $t_{\rm STR}$, followed by an exponential SFR from $t_{\rm STR}$ to 0.1Gyr ago with fixed $\tau = 1$ Gyr. The mass fractions in each component are a function of $t_{\rm STR}$, such that the SFR at $t_{\rm STR}$ is continuous.

In each model, we assume a single metallicity and a single α-enhancement for all generations of stars, and fit these parameters to the data. Our models therefore do not attempt to include chemical enrichment in any physically motivated way and so the abundance parameters are intended to represent luminosity-weighted mean values. .

Note that in the OSP, AQ, EXP, FR and STR models, we have chosen to fix the age of the old population or the "starting time" for star formation at 13 Gyr. While, in principle, one would like to leave the starting time as a free parameter, in practice, the multiple age parameters become highly degenerate. We will discuss the implications of varying the age of the oldest stars in Sections 3.2.2 and 4.5.1.

These models can be subdivided into two classes. In one class of models (OSP, EXP, FR), the stars are predominantly old. In the case of the EXP and FR models, intermediate ($\sim$ 5 Gyr) luminosity-weighted ages can arise, but these are due to a small fraction (by mass) of very young ($\lesssim$ 1 Gyr) stars in addition to the dominant (by mass) old population. In the other class of models (SSP, AQ, STR), there is little star formation at late times and the luminosity-weighted intermediate ages are due to stars which indeed formed at intermediate times. We will show that these two classes have different properties, particularly in terms of their stellar mass-to-light ratios, even when constrained to match the same line index data.

3.1.1 Generating Mock Linestrength Indices

Here we outline the procedure for generating the mock line indices as a function of input model parameters. The SSP and OSP modeled indices are simply interpolated from the TMBK model grids. Interpolation in 'age' is done in log space.

$$EW_i\left(\left[\tfrac{Z}{H}\right],\left[\tfrac{\alpha}{Fe}\right],t\right) = EW_i\left(TMBK\right) \tag{3.1}$$

The complex star formation history models require a weighted sum over the formation time range as a function of star formation rate. The total continuum flux and total absorbed flux must be calculated for each feature over the entire formation time range. The ratio of absorbed to continuum photons is the fraction of the total width of the index.

$$EW_i\left(\left[\tfrac{Z}{H}\right],\left[\tfrac{\alpha}{Fe}\right],SFR(t)\right) = \left(\frac{N_{absorbed}}{N_{continuum}}\right)_i \Delta\lambda_i \tag{3.2}$$

$$\begin{aligned}\left(N_{absorbed}\right)_i \;=\; & \left[\sum_{t_{start}}^{t_{end}}\left(F_i\left(\left[\tfrac{Z}{H}\right],t\right)\cdot EW_i\left(\left[\tfrac{Z}{H}\right],\left[\tfrac{\alpha}{Fe}\right],t\right)\cdot SFR(t)\right)\right]\cdot\left[\sum_{t_{start}}^{t_{end}} SFR(t)\right]^{-1}\end{aligned} \tag{3.3}$$

$$\begin{aligned}\left(N_{continuum}\right)_i \;=\; & \left[\sum_{t_{start}}^{t_{end}}\left(F_i\left(\left[\tfrac{Z}{H}\right],t\right)\cdot\Delta\lambda_i\cdot SFR(t)\right)\right]\cdot\left[\sum_{t_{start}}^{t_{end}} SFR(t)\right]^{-1}\end{aligned} \tag{3.4}$$

$\Delta\lambda_i$ is the defined wavelength range of the index (Nelan et al., 2005). The continuum flux (F_i) of each feature is linearly interpolated in $\log_{10}$ space, at the median wavelength.

Now we define the star formation rate for each complex star formation history model:

Exponential SFR Model

The three defining parameters are metallicity, α-enhancement, and τ (governs rate of decay), keeping t_{start} and t_{end} fixed. The equivalent width in $N_{absorbed}$ is interpolated as in the SSP, for each time step in the sum.

$$SFR(t) = exp\left(\frac{-\left(t_{start} - t\right)}{\tau}\right) \tag{3.5}$$

Abruptly Quenched Model
The three defining parameters are metallicity, α-enhancement, and t_q. The equivalent widths for this CSP are calculated precisely as in the EXP, but setting τ to a very large number (10000 Gyr) to represent a constant formation.

Frosting Model
This model consists of two SSP's superimposed. The three defining parameters are metallicity, α-enhancement, and secondary burst time t_{burst2}. The mass fractions, (MF - representative of how much of the stellar mass is used in each burst, where $\sum \left(MF\right)_j = 1$), are fixed at 0.98_1 and 0.02_2.

$$SFR(t) = MF_i\left(t_{burst}\right) \tag{3.6}$$

Strangulation Model
To explore more complex star formation histories, we contructed a scenario with constant star formation rate from 13Gyr to t_{quench}, from which an exponentially declining star formation rate occurs from t_q to 0.1Gyr. Therefore the three defining parameters are metallicity, α-enhancement, and t_q. The separate mass fractions of each component now are dependent on t_q, where we normalize the exponential tail to have the same SFR as at t_q (Equation 3.7).

$$\begin{aligned} MF_1 &= \frac{13Gyr - t_Q}{13Gyr - t_Q + \tau\left(1 - e^{(t_Q - 0.1Gyr)/\tau}\right)} \\ MF_2 &= \frac{\tau\left(1 - e^{(t_Q - 0.1Gyr)/\tau}\right)}{13Gyr - t_Q + \tau\left(1 - e^{(t_Q - 0.1Gyr)/\tau}\right)} \end{aligned} \tag{3.7}$$

3.2 Fitting Star Formation History Models to Linestrength Indices

The goal of this work is to create synthetic clusters of simulated galaxies with distributions of age and metallicity that are consistent with the observed line indices. While the observational data are of high S/N, the fitted ages and metallicities of individual galaxies have substantial correlated errors, particularly for the faintest, low velocity dispersion galaxies. Thus, rather than *invert* the data, we instead *model* the mean and scatter in the stellar population parameters, P ("age", metallicity and α-enhancement) that are required to match the median linestrength and the scatter in the observed linestrengths.

By comparing the scatters in either linestrengths (Trager et al., 2000), colours (Bernardi et al., 2005) or total M/L (Cappellari et al., 2006) as a function of velocity dispersion, with the same scatters as a function of luminosity, one finds that the correlations with velocity dispersion are always tighter than those with luminosity. Indeed, we have confirmed this using our Coma cluster data described above. These results strongly suggest that the fundamental or "driving" parameter of stellar populations is the velocity dispersion (Smith et al., 2009a), an assumption we will make in this thesis. Thus we divide our sample into five bins by $\log(\sigma)$ and measure median Lick indices and scatters for each bin, both of which are then fit to each star formation history model.

We will use the six Lick indices given in Table 3.1 to break the degeneracies between "age" (traced primarily by the Balmer lines: HδF, HγF, Hβ), Fe (Fe4383, Fe5015) and α-element enhancement (Mgb5177). We assign the galaxies to five bins in velocity dispersion, and for each bin we calculate the observed median linestrength index. Our stellar population parameters include one age-related parameter ($t_{\rm SSP}$,$t_{\rm AQ}$,$t_{\rm STR}$,τ,$t_{\rm FR}$), $[Z/H]$ and α/Fe.

In general, however, we expect that the linestrength data may have small zero-point offsets. To compare with previous results, and following Smith et al. (2009a), we force the median line indices in the highest-velocity dispersion bin to equal the SSP-parameters recovered by Nelan et al. (2005) in their highest velocity dispersion bin: (age, [Z/H], [α/Fe]) = (10.8 Gyr, 0.24, 0.28). This corresponding offset given in Table 3.1 in each line is then applied to all bins.

Our goal is not only to fit the median line indices at each velocity dispersion, but also fit the spread in ages, metallicities and α-enhancement to the spread in each line index of each bin. We first calculate the total observed scatter $S_{\rm tot}$ in a given index I at a fixed σ by measuring the semi-interquartile-range (SIQR) and convert this to its Gaussian equivalent:

Table 3.1. Best-Fit Line Index Corrections

Line Index	Correction[a]($\AA$)
HδF	-0.063
HγF	+0.026
Fe4383	+0.257
Hβ	+0.061
Fe5015	+0.667
Mgb5177	+0.274

[a]Applied to all observed bins

$S_{\rm tot}$ = SIQR/0.67. This is more robust to outliers than the usual root-mean-square. We then estimate the *intrinsic* dispersion in line index properties as follows:

$$S^2_{\rm int} = S^2_{\rm tot} - S^2_{\rm meas} \tag{3.8}$$

where $S_{\rm meas}$ is taken to be the median measurement error in the bin for each specific absorption line.

3.2.1 Results

Fits to Median Linestrengths

We employ a simple χ^2 fitting scheme to the observed median linestrength indices. The lines are fit simultaneously with equal weighting to each set of model parameters. The results are shown in Figure 3.1 and are tabulated in Table 3.2, along with the Shapley binned values to which the models were fit. Corresponding model parameters appear in Table 3.3. Note that, for the Balmer lines HγF and Hβ, the scaling is roughly linear at high velocity dispersions, but the lowest-σ bin appears to deviate from this linear relationship. This will yield older ages for this bin. We will discuss this further in Section 3.3.4.

From Fig. 3.1, we see that all models, except the Old SSP Model which is clearly a poor fit, yield similar predicted linestrengths. However, closer inspection of Hβ shows the SSP, AQ and STR models are a better fit to this index. To quantify this, we calculate a

χ^2 for each model, for each line, as well as an aggregate χ^2 over all six lines for the four lowest mass bins (since we have fit a free offset to match the high velocity dispersion bin), and these values are tabulated in Table 3.2. Formally, the EXP, FR and OSP are poor fits, the latter being rejected at > 99.99 CL. However, this is somewhat driven by our choice to correct the linestrengths to obtain a given age in the highest velocity dispersion bin, particularly for Hβ. If instead, we attempt to fit Hβ in all velocity dispersion bins simultaneously, then EXP and FR remain poorer fits than SSP but are no longer formally rejected. The OSP model, however, is still rejected at a high confidence level.

Fits to Scatter

With at least three lines, we can iteratively calculate the best fit intrinsic scatter $S_{1,2,3}$ in the three model parameters $P_{1,2,3}$, where P_1 represents the age-related parameter ($\log(t_{\rm SSP})$ for the SSP case) and $P_{2,3}$ are metallicity and α-enhancement respectively:

$$S^2_{\rm pred} = \sum_{i=1}^{3} \left(\frac{\partial I}{\partial P_i} \right)^2 S_i^2 \tag{3.9}$$

where the derivatives $\frac{\partial I}{\partial P_i}$ are calculated numerically from the model grids.

The above formula assumes that, at a given σ, the intrinsic scatter in age, for example, is independent of that of metallicity. However, we know that these parameters are not in fact independent. Worthey (1994), and later Trager et al. (2000) showed that there is a correlation between age and metallicity at a fixed mass. Smith et al. (2008) found $\partial[Z/H]/\partial \log(t_{\rm SSP}) = -0.68$ and $\partial[\alpha/{\rm Fe}]/\partial \log({\rm t_{SSP}}) = 0.34$, using the same Shapley data as in this work.

To allow for correlated scatter, we modify equation (3.9) as follows. We allow for a scatter in the age parameter, and a correlated scatter in metallicity and α-enhancement. The sense of the correlation is that if a galaxy is older than the median by 0.1 dex, it is more metal-poor by –0.068 dex (SSP). We also allow for "extra" or residual uncorrelated scatter in the latter two parameters. We can now predict the scatter in each index as a function of the predicted scatter in each model parameter as

$$\begin{aligned} S^2_{\rm pred} &= \left(\frac{\partial I}{\partial t} + \sum_{i=2}^{3} \left(\frac{\partial I}{\partial P_i} \right) \left(\frac{\partial P_i}{\partial t} \right) \Big|_{log(\sigma)} \right) S_t^2 \\ &\quad + \sum_{i=2}^{3} \left(\frac{\partial I}{\partial P_i} \right)^2 S^2_{i,\rm res} \end{aligned} \tag{3.10}$$

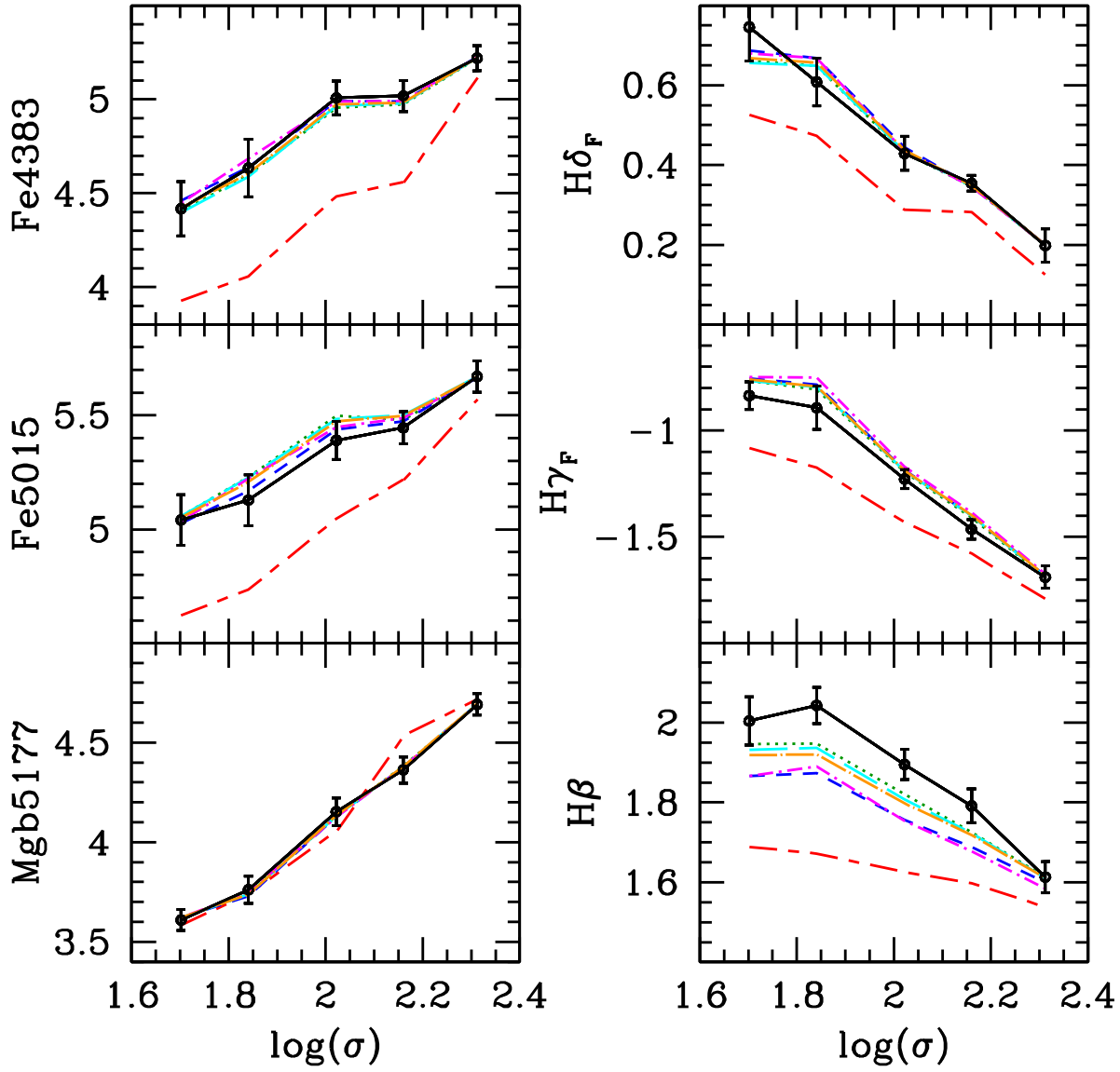

Figure 3.1 Linestrengths as a function of velocity dispersion. The Shapley binned linestrength data are shown by the black lines and circles, with error bars representing the uncertainty in the median. The predicted line index values for the best fit model parameters for each model are also shown: OSP (red short - long dashed); SSP (green dotted); EXP (blue short dashed line); AQ (cyan long dashed); FR (magenta dot - short dashed), STR orange dot - long dashed). Note that the OSP model is offset even in the highest velocity dispersion bin because we have adopted an age of 13 Gyr for this model rather than the default of 10.8 Gyr. It is clear that, with the exception of OSP, the models are nearly degenerate in most line indices.

Table 3.2 Best-Fit Model Linestrength Indices by Bin and Model

Bin	Line	Median ($\AA$)	$\frac{Error\ in}{Median}$	S	SSP	AQ	STR	EXP	FR	OSP
σ in km/s		Observed Data					Model Best Fits			
Range of σ	HδF	0.746	0.085	0.287	0.660	0.655	0.667	0.687	0.679	0.525
$= 35 \rightarrow 59$;	HγF	-0.836	0.065	0.205	-0.767	-0.766	-0.762	-0.756	-0.748	-1.084
$\langle \log(\sigma) \rangle$	Fe4383	4.417	0.144	0.510	4.402	4.397	4.419	4.460	4.447	3.925
$= 1.706$	Hβ	2.004	0.060	0.222	1.946	1.932	1.917	1.867	1.866	1.687
	Fe5015	5.041	0.110	0.405	5.058	5.058	5.050	5.026	5.034	4.621
$N_{gal} = 33$	Mgb5177	3.610	0.052	0.168	3.621	3.620	3.620	3.623	3.623	3.582
				χ^2:	3.14	3.84	4.31	7.44	7.88	75.6
Range of σ	HδF	0.608	0.060	0.207	0.648	0.648	0.656	0.668	0.668	0.472
$= 59 \rightarrow 84$	HγF	-0.893	0.102	0.466	-0.806	-0.794	-0.795	-0.785	-0.752	-1.177
$\langle \log(\sigma) \rangle$	Fe4383	4.634	0.153	0.674	4.596	4.588	4.603	4.637	4.683	4.055
$= 1.844$	Hβ	2.043	0.045	0.181	1.947	1.936	1.919	1.873	1.891	1.671
	Fe5015	5.128	0.111	0.489	5.228	5.228	5.205	5.168	5.223	4.733
$N_{gal} = 37$	Mgb5177	3.761	0.068	0.300	3.739	3.739	3.736	3.728	3.750	3.738
				χ^2:	6.64	7.91	9.67	16.5	15.1	107
Range of σ	HδF	0.429	0.042	0.153	0.431	0.434	0.436	0.444	0.435	0.287
$= 84 \rightarrow 124$;	HγF	-1.228	0.045	0.184	-1.195	-1.190	-1.190	-1.184	-1.169	-1.433
$\langle \log(\sigma) \rangle$	Fe4383	5.008	0.090	0.387	4.956	4.966	4.971	4.991	4.988	4.482
$= 2.022$	Hβ	1.895	0.038	0.164	1.821	1.808	1.797	1.756	1.754	1.625
	Fe5015	5.391	0.083	0.362	5.498	5.485	5.472	5.437	5.448	5.045
$N_{gal} = 37$	Mgb5177	4.153	0.070	0.329	4.132	4.132	4.132	4.128	4.127	4.054
				χ^2:	6.49	7.55	8.70	15.0	16.2	136
Range of σ	HδF	0.354	0.019	0.166	0.346	0.347	0.347	0.348	0.346	0.281
$= 124 \rightarrow 171$;	HγF	-1.464	0.046	0.200	-1.409	-1.401	-1.401	-1.399	-1.384	-1.580
$\langle \log(\sigma) \rangle$	Fe4383	5.018	0.082	0.344	4.972	4.978	4.980	4.990	4.992	4.557
$= 2.160$	Hβ	1.792	0.042	0.192	1.725	1.723	1.718	1.688	1.678	1.597
	Fe5015	5.446	0.071	0.307	5.480	5.501	5.496	5.473	5.488	5.216
$N_{gal} = 37$	Mgb5177	4.363	0.066	0.309	4.382	4.377	4.377	4.375	4.377	4.533
				χ^2:	4.64	5.51	5.80	8.28	10.9	89.9
Range of σ	HδF	0.198	0.042	0.181	0.198	0.199	0.200	0.201	0.200	0.124
$= 171 \rightarrow 314$;	HγF	-1.689	0.052	0.240	-1.689	-1.687	-1.686	-1.682	-1.673	-1.794
$\langle \log(\sigma) \rangle$	Fe4383	5.219	0.067	0.290	5.219	5.222	5.220	5.227	5.225	5.116
$= 2.312$	Hβ	1.613	0.039	0.179	1.613	1.611	1.609	1.601	1.584	1.537
	Fe5015	5.671	0.068	0.305	5.671	5.669	5.667	5.666	5.668	5.569
$N_{gal} = 36$	Mgb5177	4.692	0.054	0.250	4.692	4.693	4.693	4.692	4.690	4.714
				χ^2:	0.00	0.00	0.02	0.14	0.63	15.8
				Bins $1 \rightarrow 4$, Total χ^2:	20.91	24.8	28.5	47.2	50.1	409

Table 3.3 Best-Fit Model Parameters by Bin

Range of σ (km/s)	$\langle\log(\sigma)\rangle$	χ^2	$\langle Age\rangle$ (Gyr)	$\langle[Z/H]\rangle$	$\langle[\alpha/Fe]\rangle$	χ^2	$S(Age)$	$S([Z/H])_{\rm res}$	$S([\alpha/Fe])_{\rm res}$
Single Stellar Population Model (SSP); Age = time since single burst									
$35-59$	1.706	3.14	5.91	-0.002	0.189	25.6	0.186	0.001	0.105
$59-84$	1.844	6.64	5.53	0.089	0.186	7.32	0.212	0.119	0.001
$84-124$	2.022	6.49	7.08	0.185	0.214	19.7	0.142	0.079	0.046
$124-171$	2.160	4.64	9.10	0.190	0.260	21.6	0.151	0.075	0.048
$171-314$	2.312	0.00	10.8	0.240	0.280	33.4	0.141	0.070	0.041
Abruptly Quenched Model (AQ); Age = time since quenching									
$35-59$	1.706	3.84	3.17	-0.009	0.183	39.9	0.228	0.001	0.115
$59-84$	1.844	7.91	2.66	0.081	0.180	8.61	0.331	0.121	0.001
$84-124$	2.022	7.55	3.99	0.180	0.211	22.1	0.238	0.085	0.039
$124-171$	2.160	5.51	6.15	0.188	0.257	24.3	0.271	0.080	0.047
$171-314$	2.312	0.00	9.06	0.240	0.280	44.9	0.136	0.090	0.037
Strangulation Model (STR); Age = time since quenching									
$35-59$	1.706	4.31	5.44	-0.018	0.175	41.2	0.123	0.001	0.116
$59-84$	1.844	9.67	5.05	0.056	0.169	4.95	0.218	0.109	0.001
$84-124$	2.022	8.70	6.14	0.169	0.206	25.5	0.087	0.084	0.001
$124-171$	2.160	5.80	7.90	0.184	0.255	22.2	0.127	0.074	0.001
$171-314$	2.312	0.02	10.57	0.238	0.280	43.6	0.117	0.063	0.036
Exponential Star Formation Rate Model (EXP); Age = e-folding time									
$35-59$	1.706	7.44	2.28	-0.040	0.161	27.2	0.711	0.001	0.095
$59-84$	1.844	16.5	2.39	0.005	0.145	18.6	0.829	0.109	0.001
$84-124$	2.022	15.0	2.10	0.133	0.190	30.0	0.366	0.098	0.039
$124-171$	2.160	8.28	1.81	0.160	0.246	27.5	0.613	0.085	0.015
$171-314$	2.312	0.14	1.44	0.233	0.277	15.2	0.903	0.082	0.001
Frosting Model (FR); Age = time since secondary burst									
$35-59$	1.706	7.88	1.37	-0.055	0.160	32.8	0.146	0.001	0.105
$59-84$	1.844	15.1	1.23	0.000	0.132	13.9	0.159	0.122	0.001
$84-124$	2.022	16.2	1.48	0.119	0.184	27.1	0.085	0.099	0.001
$124-171$	2.160	10.9	1.78	0.153	0.241	26.0	0.097	0.099	0.001
$171-314$	2.312	0.63	2.49	0.224	0.274	19.9	0.199	0.087	0.001
Old Single Stellar Population Model (OSP); Age = time since single burst (13Gyr)									
$35-59$	1.706	75.6	13.00	-0.194	0.303	75.4	0.000	0.050	0.133
$59-84$	1.844	107	13.00	-0.151	0.303	47.0	0.000	0.137	0.067
$84-124$	2.022	136	13.00	-0.059	0.272	35.6	0.000	0.109	0.05
$124-171$	2.160	89.9	13.00	0.044	0.338	38.4	0.000	0.105	0.057
$171-314$	2.312	15.8	13.00	0.173	0.293	50.2	0.000	0.096	0.041

[a] Age Parameters: SSP: $t_{\rm SSP}$; EXP: τ; AQ: $t_{\rm AQ}$; FR: $t_{\rm FR}$; STR: $t_{\rm STR}$

[b] Age Parameters: SSP: $\log(t_{\rm SSP})$; EXP: τ; AQ: $\log(t_{\rm AQ})$; FR: $\log(t_{\rm FR})$; STR: $\log(t_{\rm STR})$

Table 3.4. Parameter Correlations

Model	$\frac{\partial[Z/H]}{\partial t}$[b]	$\frac{\partial[\alpha/Fe]}{\partial t}$[b]
SSP	-0.68[a]	0.34[a]
EXP	0.172	-0.086
AQ	-0.367	0.183
FR	-0.523	0.262
STR	-0.610	0.305

[a]Smith et al. (2008)

[b]t $\equiv$ model age parameter. See table 3.3 note b.

where t represents the age-related parameter (e.g. $t = \log(t_{\rm SSP})$ for the SSP case) and $P_{2,3}$ are metallicity and α-enhancement respectively.

By examining the response of the indices in the other star formation history models, in comparison with the SSP, it is possible to calculate the slope of the correlation between, for example, metallicity and the "age" parameter t (e.g. τ in the case of EXP models). These correlations for both metallicity and α-enhancement for all models are tabulated in Table 3.4.

Distribution of Stellar Population Parameters as a Function of Velocity Dispersion

Having outlined how the line index scatters are predicted given correlated scatter in the model parameters, we proceed to fit these scatters to the observed values. Table 3.3 presents the model parameters yielding the best fits to the line index data. Also tabulated are the fit scatters in each parameter for each bin and model. Figures 3.2 and 3.3 illustrate the parameter versus velocity dispersion relations, and their associated scatter. We also show the linear fits to the parameters, ignoring the lowest σ bin, i.e. using data with $\sigma > 70$ km s^{-1} ($\log(\sigma) > 1.844$); the quoted zero points are calculated at $\log(\sigma) = 2.00$.

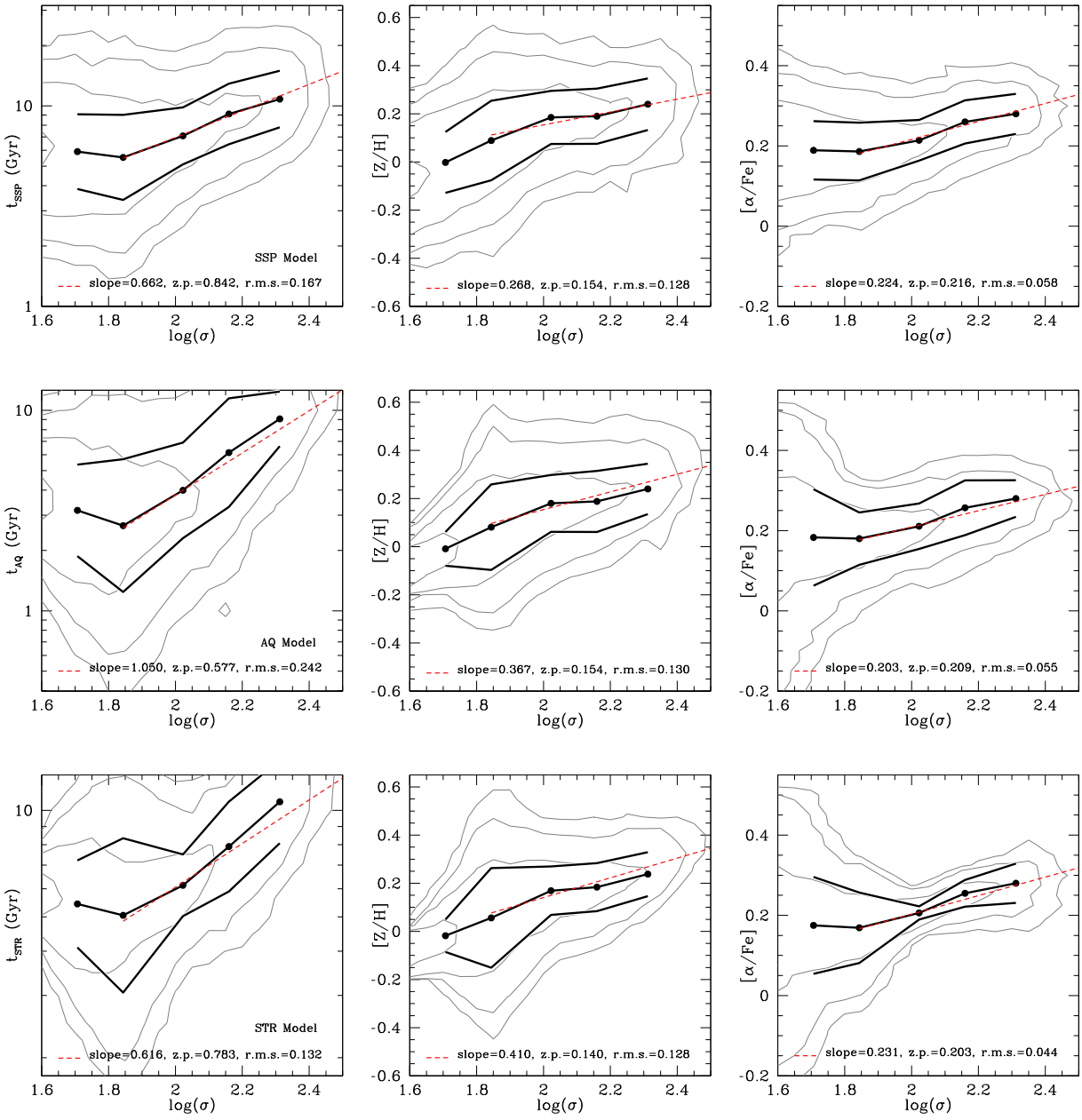

Figure 3.2 Best-fit model parameters as a function of $\log(\sigma)$. The filled points show the median values of the parameters and the solid black lines show the $\pm 1\sigma$ range. Fitted slopes (shown by red dotted lines) are to data with $\log(\sigma) > 1.844$ only. Rows from top to bottom correspond to SSP, AQ, and STR. Age parameters are as in Table 3.3. Note increasing metallicity, α-enhancement and age with increasing velocity dispersion. Synthetic cluster density contours are shown in grey, at 0.7dex increments (see Section 3.3).

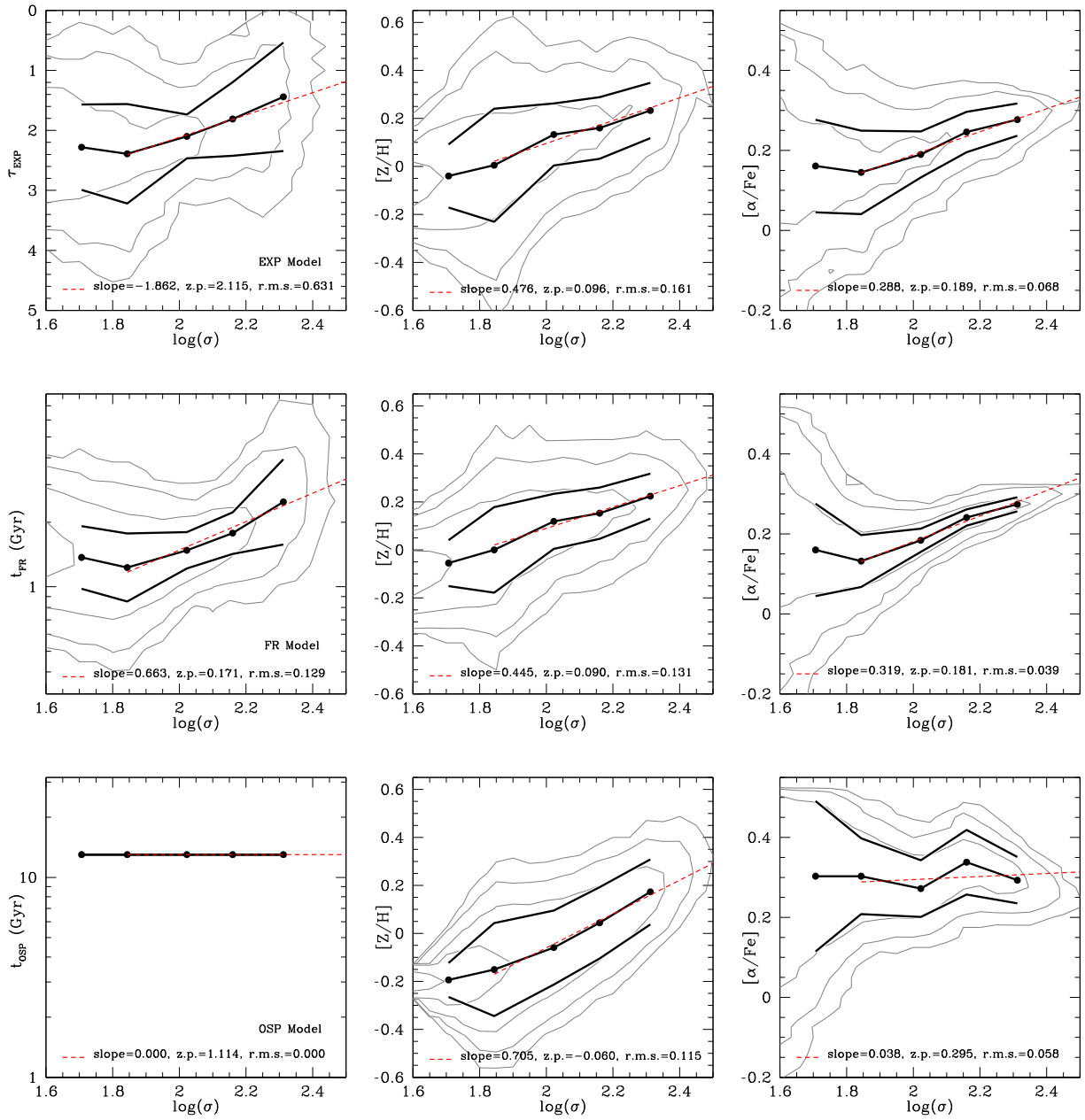

Figure 3.3 Best-fit model parameter trends with $\log(\sigma)$. Rows from top to bottom correspond to EXP, FR, and OSP. Lines, contours and symbols are as in Figure 3.2. Age parameters are as in Table 3.3. Note increasing metallicity, α-enhancement and age with increasing velocity dispersion.

3.2.2 Systematics

Aperture Effects

Our data are observed through a 1" diameter fibre, corresponding to 0.95 kpc radius at the distance of Shapley. Thus the stellar populations found above correspond to the stars within that aperture. Nevertheless, for some purposes, it is interesting to consider how this might be extrapolated to refer to all stars within the effective radius, R_e. As our data are all at a common distance we cannot solve for population gradients internally. Internal radial gradients in early-type galaxies have been studied by a number of authors, and are summarized in Table 4 of Rawle et al. (2008). They find that gradients in age and α-enhancement are small, but the gradient in Z is $\Delta Z/\Delta \log r_{\rm ap} = -0.18 \pm 0.02$. We can correct our data to R_e using this result, together with eq. 2.2. We find

$$[Z/H](R_e) - [Z/H](ap) = \begin{cases} -0.043 & \log(\sigma) < 2.23, \\ -0.50(\log\sigma/2.23) - 0.043 & \log(\sigma) > 2.23. \end{cases} \quad (3.11)$$

Thus the correction is small: -0.08 for the highest velocity dispersion bin, and ~ -0.04 for the other bins.

Line Indices: Choice of Index and Effect of Index Calibration Corrections

It is interesting to see whether the conclusions, particularly those for age, change significantly depending on which lines are used in the analysis. Here we focus on the Balmer lines, reproducing the fits with only one Balmer line rather than all three simultaneously. The results of these tests are shown in Fig. 3.4. We find that the median age in the second-lowest bin ($\log\sigma = 1.844$) changes by less than 1 Gyr (15%) depending on which Balmer line is used. In Hγ and Hβ we see a flattening or an upturn in age at the lowest velocity dispersion bin (as in Fig. 3.4), but if we only use Hδ, the lowest bin is younger.

One concern regarding the Balmer line indices is the possibility of weak infilling by AGN emission at high mass. Smith et al. (2007) Figure 7 shows the fraction of RSGs with AGN-like emission in the Shapley sample. At $M_R < -20.5$, and thus high mass and velocity dispersion, there is still significant AGN contribution on the red-sequence. While galaxies with clear emission have been removed from our sample, it is possible that weak AGN emission may cause infilling in $H\beta$, particularly for the highest velocity dispersion galaxies. If so, it is possible we have overcorrected $H\beta$ by the procedure adopted in Section

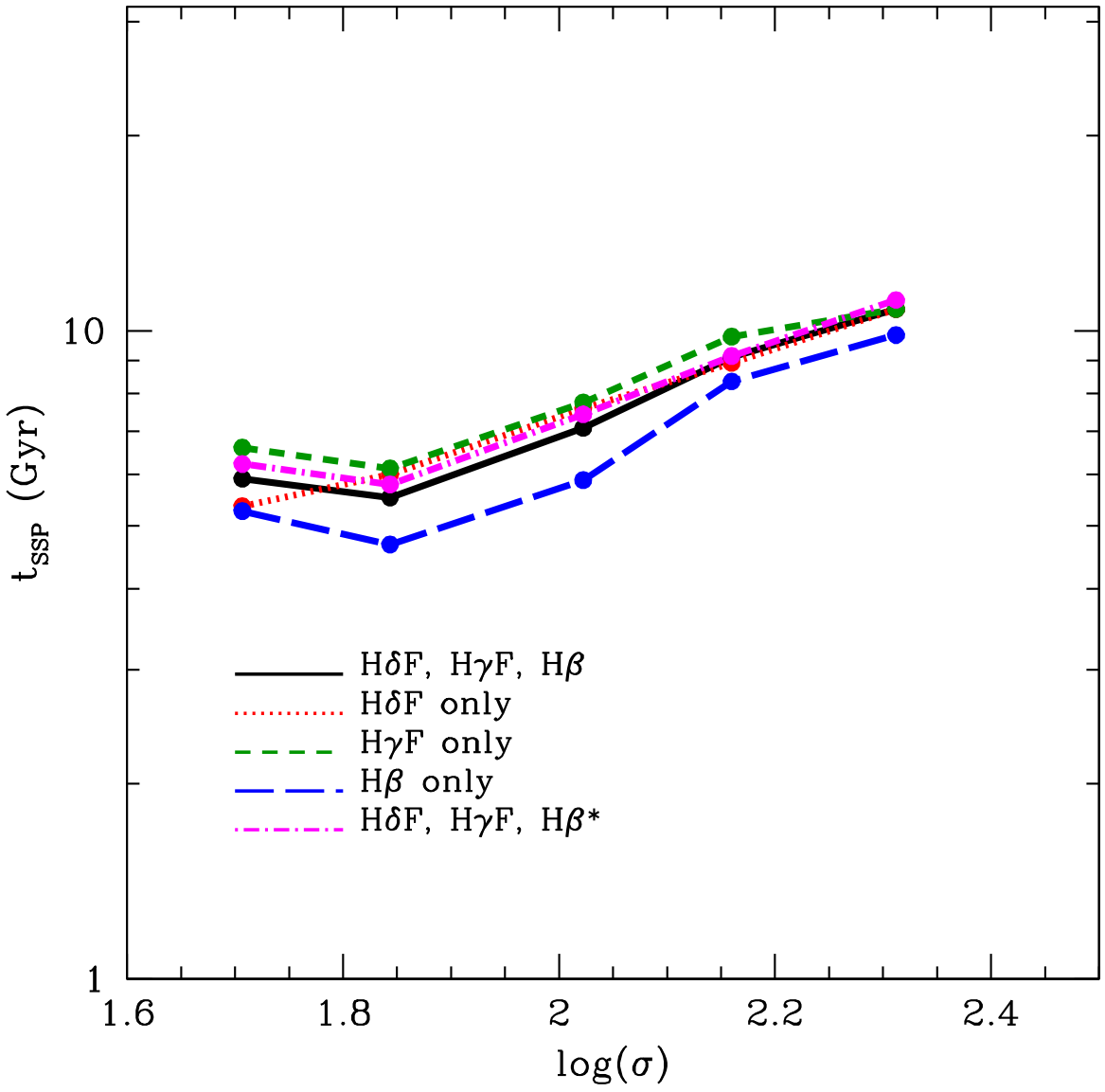

Figure 3.4 SSP age as a function of log(σ) for different choices of Balmer line used in the fits. (The Fe and Mg lines are used in all cases.) In the Hβ* case, we have fit Hβ using a calibration fit to all velocity dispersion bins (see Section 3.2.2 for details). In all cases, the choice of Balmer index makes little difference at the youngest ages.

3.2. An alternative calibration would have been to fit a zero-point iteratively to the average of all bins rather than to the highest velocity dispersion bin alone. In fact, if we fit the observed $H\beta$ indices to all velocity dispersion bins, then all models agree better with the predicted values of $H\beta$. The weak effect of this alternative correction on the derived ages is shown in Figure 3.4.

A related concern is the effect on our conclusions of the choice to calibrate all lines to Nelan et al. (2005), which itself was not calibrated to the Lick system. To test the effect of alternative calibration schemes, we have also compared our Shapley linestrength-σ relations to those from 12 Coma early-type galaxies observed by Trager et al. (2008), which we expect to be well-calibrated to the Lick system. We then fit additional offsets to our Nelan-calibrated Shapley linestrength-σ relations to match the Trager et al. (2008) linestrengths as a function of σ. In particular, the Balmer line offsets were estimated as HδF,HγF,H$\beta \sim$ 0.12,0.2,0.1 (in addition to the correction to Nelan et al. (2005) tabulated in Table 3.1). We then refit our models with this alternative calibration scheme, and find that it yields ages that are only slightly younger (by < 0.5 Gyr or 10% for the youngest galaxies). This change in stellar population parameters is smaller than other systematics. In particular, the effect of this recalibration is weaker than, but in the same sense as, the effect of fitting using only Hβ, which was discussed in the previous paragraph.

Systematics Associated with Model Parameters

In Section 3.1, in certain models, star formation was assumed to start 13 Gyr ago, which corresponds to a rather high redshift. As an alternative, we will consider a different starting time and investigate its effect on the fits. For this purpose, we choose a redshift of 2, corresponding to approximately 10.3 Gyr, as a more realistic choice, as this is close to the peak star formation in the universe (Hopkins & Beacom, 2006) . When we refit our star formation history models, we find that the CSFH age parameters shift towards older ages to compensate for the absence of very old stars. For example, for the EXP model, for the $\langle\sigma\rangle = 70$ km s^{-1} bin, τ is reduced, from its default value of 2.4 Gyr, to only 1.7 Gyr. In the AQ model, the lookback time to quenching increased from 2.7 Gyr to 3.3 Gyr. Other velocity dispersion bins are affected similarly. We also find that metallicity increases by approximately 7% in the "mostly old" models, whereas the intermediate age models show no significant change in metallicity. Finally α-enhancements remain virtually unchanged from the 13 Gyr case. We will discuss the effects of these changes on stellar mass-to-light ratios in Section 4.5.1.

Table 3.5. SSP Scaling Relations

Reference	σ range	Age	Z/H	α/Fe
Nelan et al. (2005)	$50\mathrm{km\,s^{-1}} < \sigma < 400\mathrm{km\,s^{-1}}$	0.59 ± 0.13	0.53 ± 0.08	0.31 ± 0.06
Smith et al. (2007)	$30\mathrm{km\,s^{-1}} < \sigma < 300\mathrm{km\,s^{-1}}$	0.52 ± 0.06	0.34 ± 0.04	0.23 ± 0.04
Smith et al. (2007)	$100\mathrm{km\,s^{-1}} < \sigma < 300\mathrm{km\,s^{-1}}$	0.64 ± 0.12	0.38 ± 0.09	0.36 ± 0.07
This work	$70\mathrm{km\,s^{-1}} < \sigma < 300\mathrm{km\,s^{-1}}$	0.66	0.27	0.22

Effect of Other Population Synthesis Models

Smith et al. (2009b) found a generally good agreement between our TMBK-based SSP models and the EZ-Ages model of Schiavon (2007) for age, metallicity and α-enhancement. However, they noted that there was a small [Fe/H]-dependent bias in the derived ages in the sense that the EZ-Ages ages were younger by ~ 0.25 dex per dex of [Fe/H]. Given the small range in $\langle$[Fe/H]$\rangle$ covered by our sample (only 0.05 dex for $\sigma > 70\mathrm{km\,s^{-1}}$), the effect of the choice of models on the Age-σ relation and hence on colours and mass-to-light ratios is negligible.

3.2.3 Comparison with previous work

For all models, the general stellar population trends observed here for $\sigma > 70$ km s^{-1}, are that age, metallicity and α-enhancement all increase with velocity dispersion, are in agreement with a number of previous results (Caldwell et al., 2003; Heavens et al., 2004; Nelan et al., 2005; Thomas et al., 2005; Gallazzi et al., 2006; Smith et al., 2007).

The scaling relations we find for $\sigma > 70$ km s^{-1}are tabulated in Table 3.5. Note that these are based on the fits to synthetic clusters (discussed below in Section 3.3) and are weighted to low velocity dispersions. We also show results from Smith et al. (2007), using the same Shapley data (and indices) for all galaxies and for $\sigma > 100$ km s^{-1}. In general our scaling relations are between the "all σ" and "$\sigma > 100$ km s^{-1}" relations found by Smith et al. (2007), although our scaling relation for $[Z/H]$ is somewhat flatter. In comparison with Nelan et al. (2005), the scaling of age with velocity dispersion is similar, however this analysis yields shallower relationships with $[Z/H]$ and [α/Fe]. Note that our determination of α-enhancement is based on Mgb and so primarily reflects the [Mg/Fe] abundance ratio, whereas the α-enhancement of Nelan et al. (2005) was also based on CN. A full table of comparisons is given in Smith et al. (2007).

The lowest-velocity dispersion bin ($\sigma < 70\mathrm{km\,s^{-1}}$) shows a either a flattening or an increase in the mean age of galaxies, in comparison to $\sigma > 70\mathrm{km\,s^{-1}}$. This is as a result of the downturn or flattening of the Balmer-line indices seen in Fig 3.1. We note that this change in the ages of low velocity dispersion galaxies can be seen in the fits of Smith et al. (2007), in the sense that their scaling relations are flatter when all galaxies are included and become steeper when only high velocity dispersion galaxies ($\sigma > 100$) $\mathrm{km\,s^{-1}}$ are used in the fit. Furthermore, this trend is also seen in central Coma cluster galaxies at low velocity dispersions (Smith et al., 2009b). Consequently, we argue that this effect is real, and signals the end of "downsizing" on the cluster red-sequence. We discuss selection effects that may affect the derived stellar population parameters in Section 3.3.4, but conclude there that correction for such effects would strengthen our conclusion that this "upsizing" effect is real.

In Section 3.3.4, we also show that the "pinching" of the scatter S in the lowest velocity dispersion bin is a selection effect. In reality, the scatter in age increases at decreasing velocity dispersion. This increased scatter may also help to reconcile previously contradictory results in the literature. For example, Sánchez-Blázquez et al. (2006) find no "downsizing" effect in the Coma cluster but do find downsizing in Virgo. In both clusters they have a number of objects with high-σ plus a small number (4-5) with $\log(\sigma) < 1.844$. Given the large intrinsic scatter in age that we find at low-σ (>0.2 dex or $\sim$ 3 Gyr), we argue that a sample of 4-5 galaxies is too small to secure a robust detection of the mean age of the low-σ population. Similarly, with regard to Trager et al. (2008), who also find no downsizing with a 12 galaxy sample, we argue that a sample of this size is too small to detect the downsizing effect, given the large intrinsic scatter in the age-σ relation.

3.3 Synthetic Galaxy Clusters

In section 3.2, we have shown how we derive the medians and dispersion of age, metallicity and α-enhancement as a function of velocity dispersion. For a given choice of stellar population parameters, P, we can generate stellar mass-to-light ratios, and hence colours and mass-to-light ratios, as outlined below in Section 3.3.2. To populate a synthetic cluster, the additional ingredients required are the velocity dispersion distribution, effective radii and stellar masses.

3.3.1 The Velocity Dispersion Distribution

The next step is to generate a synthetic cluster populated by galaxies with appropriate statistical distributions of velocity dispersion, effective radius, stellar mass, age and metallicity, as well as derived parameters (luminosity). Because velocity dispersion is the driving parameter, a prerequisite input is the velocity dispersion distribution (VDD). We adopt a lower limit of $\sigma = 20\mathrm{km\,s^{-1}}$ for the velocity dispersion distribution for our synthetic clusters. While we will not create velocity-dispersion-limited samples with velocity dispersions this low, because of the large scatter in the Faber-Jackson relation, it is necessary to include low velocity-dispersion galaxies in order to ensure completeness at a given magnitude.

To model the VDD, we begin with the fits of Sheth et al. (2003) to a sample of de Vaucouleurs-profile early-type galaxies in the SDSS

$$\phi(\sigma)d\sigma = \phi_* \left(\frac{\sigma}{\sigma_*}\right)^{\alpha} \frac{\exp\left[-\left(\sigma/\sigma_*\right)^{\beta}\right]}{\Gamma\left(\alpha/\beta\right)}\ \beta\ \frac{d\sigma}{\sigma} \tag{3.12}$$

where the best fit parameters are $\phi_* = 0.0020 \pm 0.0001$, $\alpha = 6.5 \pm 1.0$, $\beta = 1.93 \pm 0.22$ and $\sigma_* = 88.8 \pm 17.7\mathrm{km\,s^{-1}}$.

According to Sheth et al. (2003, Figure 6), one expects that late-type galaxies dominate the VDD, at least for velocity dispersions lower than 200 km/s. However, the exact level of the contribution of these galaxies to the VDD is very uncertain. Nevertheless, to the velocity dispersion limit to which we would like to synthesize galaxies ($\sim 20\mathrm{km\,s^{-1}}$), we expect non-early-types to make a non-negligible contribution to the RSG cluster population. Thus we model the "faint" end of the VDD as a power law in σ:

$$\phi(\sigma) \propto \sigma^{\xi} \qquad (\sigma < 200\mathrm{km\,s^{-1}})\,. \tag{3.13}$$

We choose to fit the "faint-end" slope, ξ, by adjusting it to fit the observed $z \sim 0$ red-sequence dwarf-to-giant galaxy ratio (DGR) (Gilbank & Balogh, 2008). We find this slope to be $\xi = -1.275$, yielding a DGR of 3-4 at $z = 0$. The final adopted distribution of σ is shown in Figure 3.5. For each of our CSFH models, we create 50000 galaxies from this distribution, with $\sigma > 20$ km s^{-1}.

Thus the procedure is as follows: generate a velocity dispersion from the VDD described above. For a given velocity dispersion, the mean and scatter in the stellar population parameters are known (the binned values are interpolated or extrapolated where necessary). For each of the stellar population parameters, we can thus generate a realization consistent with the statistical distributions, allowing for correlation between offset in "age" and the offset in metallicity, and likewise between "age" and α-enhancement. The distribution of the simulated populations are shown by the contours in Figures 3.2 and 3.3.

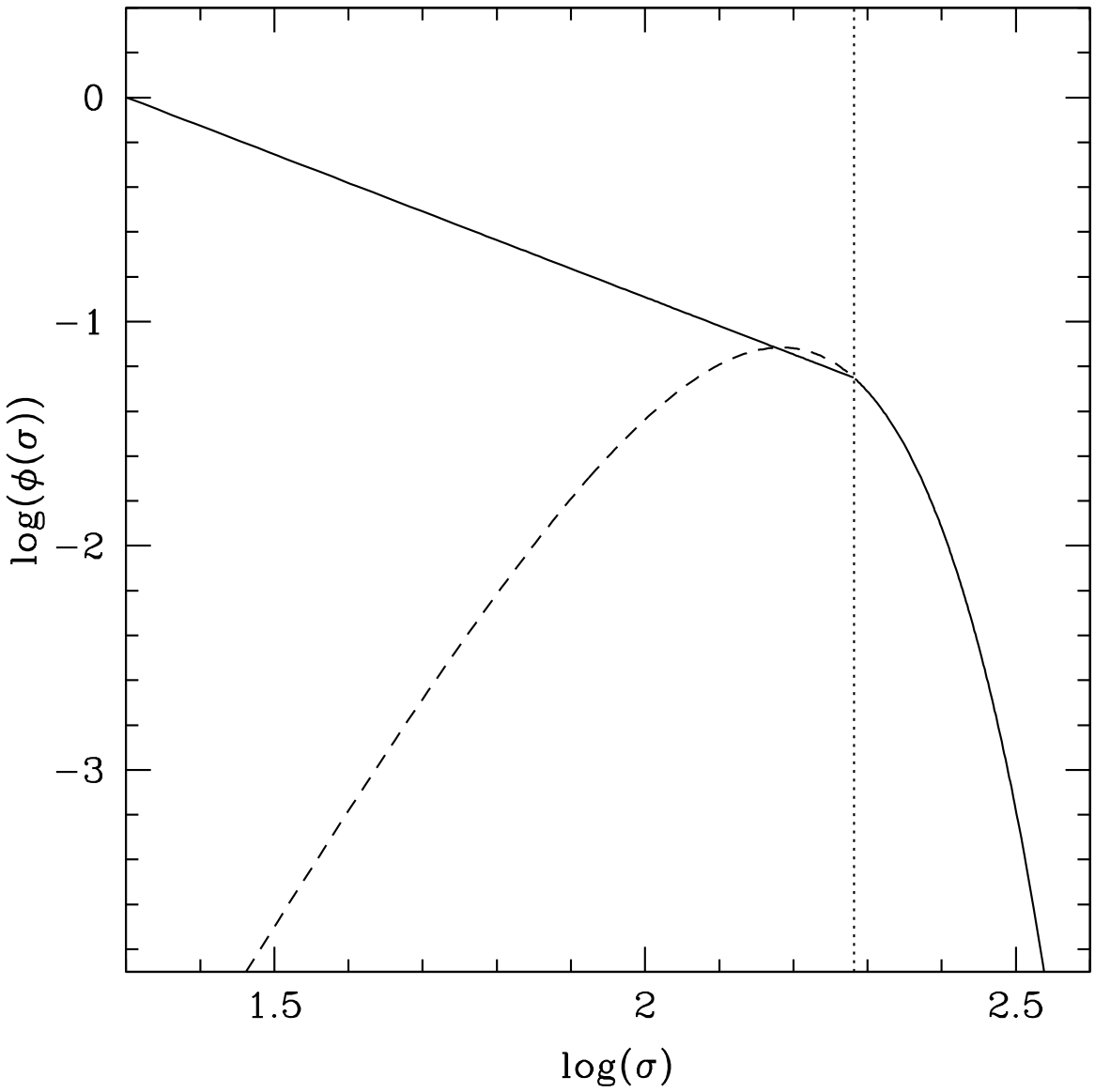

Figure 3.5 The normalized velocity dispersion distribution (VDD) of early-types from Sheth et al. (2003), with extrapolation to low velocity dispersions shown by the dashed line. Late-type galaxies dominate at $\sigma < 200\mathrm{km\,s^{-1}}$. We approximate this with a power law (solid line) and fit the slope such that the resulting dwarf-to-giant ratio of all models reasonably matches the $z \sim 0$ observed dwarf-to-giant ratio of Gilbank & Balogh (2008) (see Section 5.3).

3.3.2 Mass-To-Light Ratios and Colours

Having generated the stellar population parameters for our synthetic, clusters, we now turn to predicting observables, such as colour. The models of Maraston (Maraston, 1998, 2005) provide grids of stellar mass-to-light ratios in both the Johnson-Cousins and SDSS filter sets, which can be used to compute colours as a function of age and metallicity. Here we adopt the Kroupa (2001) IMF with red/intermediate horizontal branch. Using the Salpeter IMF would increase the M_*/L ratios by a factor of ~ 1.6 (Thomas et al., 2005); we discuss the effects of the choice of IMF in Section 4.5.2.

We then fit scaling relations of mass-to-light ratio and colour as a function of velocity dispersion. For the fits, only galaxies with velocity dispersion $\log(\sigma) > 1.844$ are used, as these are not affected by the "upturn" in age at low velocity dispersion (Figures 3.2, 3.3). Tables 3.6 and 3.7 summarize the slopes and intercepts as a function of velocity dispersion for Johnson-Cousins, infrared and SDSS passbands for each star formation history model. Zero points are measured at $\log(\sigma) = 2.00$.

3.3.3 Effective Radii, Stellar Masses and Luminosities

In order to predict luminosities and the Fundamental Plane, we need to assign a stellar mass and an effective radius to each synthetic galaxy.

We assign an R_e based on the σ, following the broken-power-law model of our Coma data in Section 2.2, allowing for scatter in this relation by generating a random Gaussian deviate with the same root-mean-square scatter as given in Figure 2.2. Total mass is then assigned according to the virial relation

$$M = c_2 \frac{\sigma_e^2 R_e}{G} \tag{3.14}$$

where here we assume $\sigma_e \sim \sigma$ (see Section 4.4). The factor c_2 depends on the luminosity distribution, velocity dispersion anisotropy and rotation. Perhaps surprisingly, Cappellari et al. (2006) found that a constant $c_2 = 5$ was an excellent approximation to detailed dynamical mass reconstructions. This indicates that there is little evidence for non-homology, i.e. a dependence of c_2 on mass or velocity dispersion. The same result, that early-types are homologous, has also been found using gravitational lensing as a mass estimator (Bolton et al., 2008). Note that Cappellari et al. (2006) measured R_e in the I-band, which is close to the r band used here for measuring R_e, so their value of c_2 may be transferred to this analysis. Denoting the fraction of the total mass in stars as f_*, we then have $M_* = f_* M$.

Table 3.6 Mass-To-Light Ratio, Magnitude, Colour - Velocity Dispersion Relations By Model (Johnson-Cousins [Vega])

Band (X)	$m = \frac{d\log(M/L_X)}{d\log(\sigma)}$ [a]	z.p.[b]	r.m.s.	$\frac{dM_X}{d\log(\sigma)}$ [a]	z.p.[b]	r.m.s.	colour	$\frac{d(X-X')}{d\log(\sigma)}$ [a]	z.p.[b]	r.m.s.
Single Stellar Population Model (SSP)										
U	0.956	0.757	0.135	-3.666	-18.283	0.661	U-B	0.457	0.571	0.041
B	0.773	0.581	0.125	-4.123	-18.855	0.649	B-V	0.199	0.980	0.019
V	0.693	0.449	0.120	-4.322	-19.835	0.643	V-R	0.099	0.475	0.009
R	0.654	0.423	0.118	-4.421	-20.310	0.640	R-I	0.093	0.613	0.010
I	0.617	0.313	0.116	-4.513	-20.923	0.638	I-J	0.231	1.107	0.046
J	0.524	0.047	0.128	-4.744	-22.030	0.653	J-H	0.054	0.674	0.008
H	0.503	-0.095	0.128	-4.798	-22.704	0.653	H-K	0.052	0.224	0.017
K	0.482	-0.168	0.133	-4.851	-22.928	0.660	-	-	-	-
Abruptly Quenched Model (AQ)										
U	0.726	0.799	0.082	-4.231	-18.191	0.606	U-B	0.422	0.574	0.052
B	0.557	0.621	0.069	-4.653	-18.764	0.597	B-V	0.186	0.981	0.022
V	0.483	0.489	0.064	-4.839	-19.745	0.594	V-R	0.087	0.477	0.012
R	0.448	0.462	0.062	-4.926	-20.222	0.593	R-I	0.076	0.615	0.012
I	0.418	0.352	0.061	-5.002	-20.837	0.592	I-J	0.227	1.114	0.060
J	0.327	0.082	0.072	-5.230	-21.952	0.601	J-H	0.041	0.677	0.011
H	0.311	-0.061	0.074	-5.270	-22.628	0.602	H-K	0.048	0.227	0.021
K	0.292	-0.135	0.080	-5.318	-22.856	0.607	-	-	-	-
Strangulation Model (STR)										
U	0.664	0.819	0.062	-4.353	-18.132	0.596	U-B	0.421	0.573	0.048
B	0.496	0.642	0.049	-4.775	-18.705	0.590	B-V	0.191	0.979	0.020
V	0.419	0.510	0.044	-4.966	-19.684	0.587	V-R	0.086	0.477	0.010
R	0.385	0.483	0.042	-5.052	-20.161	0.587	R-I	0.073	0.616	0.011
I	0.356	0.373	0.042	-5.125	-20.777	0.587	I-J	0.235	1.111	0.057
J	0.262	0.105	0.052	-5.360	-21.888	0.594	J-H	0.039	0.677	0.009
H	0.246	-0.038	0.054	-5.399	-22.564	0.595	H-K	0.051	0.226	0.018
K	0.226	-0.112	0.060	-5.450	-22.790	0.599	-	-	-	-
Exponential Star Formation Rate Model (EXP)										
U	0.478	0.896	0.063	-4.694	-17.931	0.597	U-B	0.380	0.583	0.063
B	0.326	0.715	0.040	-5.073	-18.513	0.582	B-V	0.168	0.982	0.024
V	0.259	0.582	0.031	-5.241	-19.496	0.578	V-R	0.072	0.481	0.013
R	0.230	0.554	0.027	-5.313	-19.977	0.577	R-I	0.063	0.621	0.013
I	0.205	0.442	0.025	-5.376	-20.597	0.575	I-J	0.230	1.107	0.071
J	0.113	0.175	0.032	-5.607	-21.705	0.577	J-H	0.040	0.679	0.013
H	0.096	0.031	0.036	-5.647	-22.384	0.578	H-K	0.048	0.225	0.020
K	0.077	-0.043	0.042	-5.694	-22.609	0.581	-	-	-	-
Frosting Model (FR)										
U	0.395	0.972	0.069	-5.123	-17.743	0.596	U-B	0.341	0.613	0.062
B	0.259	0.779	0.044	-5.464	-18.357	0.581	B-V	0.159	0.996	0.025
V	0.195	0.640	0.034	-5.623	-19.353	0.577	V-R	0.062	0.489	0.012
R	0.171	0.609	0.030	-5.684	-19.842	0.576	R-I	0.048	0.630	0.014
I	0.151	0.493	0.025	-5.733	-20.472	0.574	I-J	0.201	1.123	0.063
J	0.071	0.220	0.011	-5.934	-21.594	0.572	J-H	0.014	0.689	0.010
H	0.066	0.072	0.013	-5.947	-22.283	0.573	H-K	0.026	0.233	0.017
K	0.055	-0.005	0.019	-5.973	-22.517	0.574	-	-	-	-
Old Single Stellar Population Model (OSP)										
U	0.451	0.960	0.073	-4.903	-17.774	0.603	U-B	0.423	0.584	0.069
B	0.282	0.779	0.046	-5.326	-18.358	0.586	B-V	0.159	0.993	0.026
V	0.218	0.641	0.035	-5.486	-19.352	0.582	V-R	0.068	0.484	0.011
R	0.191	0.612	0.031	-5.553	-19.835	0.580	R-I	0.069	0.620	0.011
I	0.164	0.500	0.027	-5.622	-20.456	0.579	I-J	0.303	1.057	0.048
J	0.043	0.253	0.008	-5.926	-21.512	0.577	J-H	0.059	0.672	0.011
H	0.019	0.112	0.004	-5.985	-22.185	0.576	H-K	0.062	0.210	0.010
K	-0.006	0.044	0.004	-6.047	-22.394	0.577	-	-	-	-

[a] Measured with galaxies with $\log(\sigma) > 1.844$

[b] Measured at $\log(\sigma) = 2.00$

Table 3.7 Mass-To-Light Ratio, Magnitude, Colour - Velocity Dispersion Relations By Model (SDSS [AB])

Band (X)	$m = \frac{d\log(M/L_X)}{d\log(\sigma)}$ [a]	z.p.[b]	r.m.s.	$\frac{dM_X}{d\log(\sigma)}$ [a]	z.p.[b]	r.m.s.	colour	$\frac{d(X-X')}{d\log(\sigma)}$ [a]	z.p.[b]	r.m.s.
Single Stellar Population Model (SSP)										
u	0.958	0.735	0.136	-3.529	-17.553	0.667	u-g	0.545	1.807	0.050
g	0.740	0.528	0.123	-4.075	-19.360	0.651	g-r	0.196	0.838	0.018
r	0.662	0.373	0.119	-4.270	-20.198	0.646	r-i	0.084	0.320	0.009
i	0.628	0.289	0.117	-4.354	-20.518	0.643	i-z	0.109	0.296	0.015
z	0.585	0.191	0.118	-4.463	-20.814	0.645	z-J	0.151	1.220	0.034
Abruptly Quenched Model (AQ)										
u	0.727	0.777	0.082	-4.151	-17.456	0.608	u-g	0.502	1.811	0.061
g	0.527	0.568	0.067	-4.653	-19.266	0.597	g-r	0.179	0.840	0.022
r	0.455	0.412	0.062	-4.833	-20.106	0.594	r-i	0.068	0.322	0.010
i	0.428	0.328	0.061	-4.900	-20.428	0.594	i-z	0.100	0.298	0.021
z	0.388	0.228	0.063	-5.000	-20.726	0.595	z-J	0.153	1.226	0.044
Strangulation Model (STR)										
u	0.664	0.797	0.061	-4.253	-17.403	0.586	u-g	0.500	1.809	0.057
g	0.464	0.589	0.047	-4.753	-19.212	0.579	g-r	0.181	0.839	0.020
r	0.391	0.434	0.043	-4.934	-20.051	0.577	r-i	0.065	0.323	0.009
i	0.366	0.349	0.042	-4.999	-20.374	0.577	i-z	0.102	0.298	0.020
z	0.325	0.250	0.043	-5.101	-20.671	0.578	z-J	0.158	1.223	0.041
Exponential Star Formation Rate Model (EXP)										
u	0.477	0.876	0.064	-4.830	-17.201	0.589	u-g	0.450	1.822	0.075
g	0.297	0.663	0.036	-5.280	-19.023	0.573	g-r	0.155	0.844	0.024
r	0.235	0.505	0.028	-5.435	-19.868	0.570	r-i	0.053	0.328	0.010
i	0.214	0.418	0.025	-5.488	-20.196	0.570	i-z	0.100	0.298	0.026
z	0.174	0.319	0.023	-5.588	-20.494	0.569	z-J	0.154	1.220	0.050
Frosting Model (FR)										
u	0.393	0.952	0.069	-5.090	-17.003	0.593	u-g	0.404	1.860	0.073
g	0.231	0.724	0.040	-5.494	-18.863	0.578	g-r	0.143	0.859	0.024
r	0.174	0.561	0.031	-5.637	-19.721	0.574	r-i	0.038	0.337	0.011
i	0.159	0.470	0.027	-5.675	-20.058	0.573	i-z	0.086	0.307	0.025
z	0.124	0.367	0.018	-5.761	-20.365	0.572	z-J	0.134	1.229	0.044
Old Single Stellar Population Model (OSP)										
u	0.454	0.939	0.074	-4.873	-17.033	0.599	u-g	0.498	1.826	0.082
g	0.255	0.724	0.041	-5.370	-18.859	0.581	g-r	0.149	0.851	0.024
r	0.196	0.563	0.032	-5.519	-19.710	0.578	r-i	0.050	0.330	0.008
i	0.176	0.475	0.029	-5.569	-20.041	0.577	i-z	0.129	0.284	0.021
z	0.124	0.382	0.020	-5.699	-20.324	0.576	z-J	0.204	1.182	0.032

[a] Measured with galaxies with $\log(\sigma) > 1.844$

[b] Measured at $\log(\sigma) = 2.00$

Clearly for our analysis, c_2 and f_* are degenerate. We adopt $c_2 = 5$ and $f_* = 1$ (no dark matter), and return to discuss these assumptions in Section 4.5.3.

Finally, the magnitudes are then given by, for example in the R-band,

$$M_R = M_{R_\odot} - 2.5 \log \left(\frac{M_*}{M_*/L_R} \right) \tag{3.15}$$

where the stellar M_*/L_R is given by the Maraston models for the known stellar population parameters, constructed as described in Section 3.1.

3.3.4 Selection Effects at Faint Magnitudes

As noted above, the model fits show an increase in all age-related parameters at low velocity dispersion. Kelson et al. (2006) pointed out that a magnitude-limited sample will lead to biases in stellar population parameters at fixed mass because, for example, older galaxies will be fainter and hence will be excluded by the magnitude limit. This bias was also studied by Graves et al. (2007), who calibrated the bias empirically, and found a larger correction to metallicity than to age.

Here, we use our synthetic cluster populations to determine the effect of this bias on our modeled stellar population parameters. Our Shapley sample was limited to $m_R < 18$, or $M_R < -18.65$, but our synthetic clusters are limited by velocity dispersion, not by magnitude. By removing the synthetic galaxies fainter than -18.65, we can quantify the biases that may result from this selection by refitting the model parameters to the magnitude-limited sample. Figure 3.6 illustrates the effect, in the case of the SSP model. We find that, when faint galaxies are excluded, the remaining low-σ galaxies are younger, more metal-rich and less-α enhanced. One might naively expect the bias in metallicity to go in the opposite sense: i.e. metal-poor galaxies are brighter and hence they should be preferentially included in a magnitude-limited sample. However, in our SSP model, the scatter in age and metallicity at fixed σ is assumed to be anti-correlated (Section 3.2.1). Since the effect of age on mass-to-light is greater than that of metallicity, the bias towards younger brighter galaxies implies that we are also selecting relatively metal-rich galaxies. The correlated scatter between age and α-enhancement goes in the opposite sense, and hence so does the correction to α-enhancement. The effects of this selection bias are small, however, and affect only the lowest velocity dispersion bin. Now because the original Shapley data were indeed magnitude-limited, then to account properly for this selection effect, a correction should be applied (in the opposite sense to that found when faint galaxies are removed from the synthetic cluster sample). The corrected stellar population

parameters are shown by the dashed line in Figure 3.6. Thus the correction, if applied, would make the low velocity dispersion galaxies older, less metal-rich and more α-enhanced. The same bias also affects the scatter in stellar population parameters: because galaxies are removed from the magnitude-limited sample, the scatter in, for example, age is reduced. Thus a correction for selection would increase the scatter at low velocity dispersion. We do not correct for these effects in this work, because Figure 3.6 shows that the effects are small. Nevertheless, the sense of the correction strengthens our conclusion that the "upsizing" at low velocity dispersion is real. Note, however, that the selection does not affect the robust "downsizing" trend seen at higher velocity dispersion ($\sigma > 70\mathrm{km\,s^{-1}}$).

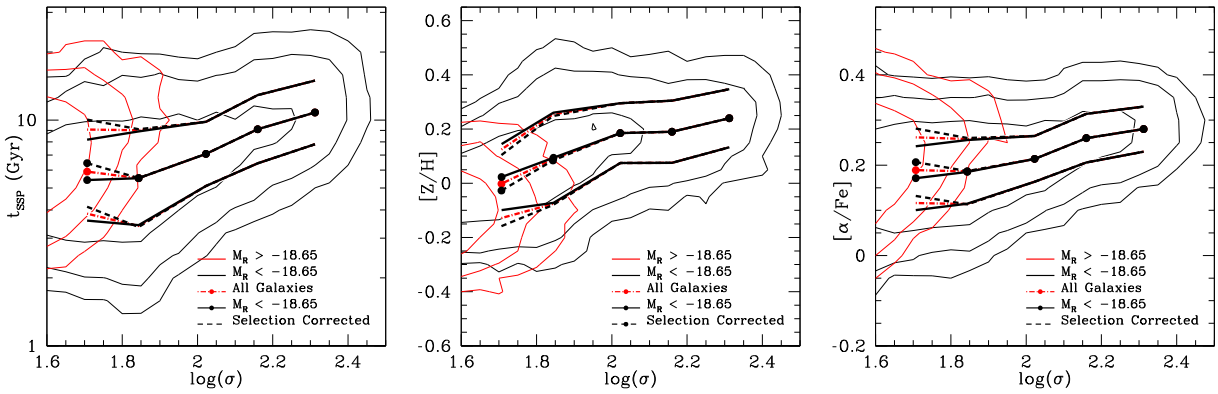

Figure 3.6 Effect of a magnitude limit on the modeled SSP stellar population parameters. The Shapley data, on which the stellar populations of our synthetic clusters are based, were limited to $M_R < -18.65$. Thus the derived stellar populations, and hence the mock clusters, may be affected by biases due to this magnitude limit. However, having fixed the stellar populations, there is no explicit magnitude limit in the synthetic clusters, i.e. some galaxies have magnitudes fainter than -18.65. This allows us to use the synthetic clusters to test the biases due to the magnitude limit. Black contours represent galaxies with $M_R < -18.65$, whereas red contours represent galaxies with $M_R > -18.65$ which would have been excluded had our synthetic clusters been magnitude limited. The dot - dashed red lines are fits to the stellar populations of the synthetic clusters with the faint galaxies included in the entire population, whereas the solid black lines are the fits when the faint galaxies are removed. When faint galaxies are removed from the sample, we find that, at the low velocity dispersions, the population is generally younger, more metal and less α-enhanced. The scatter in each stellar population parameter also decreases. Therefore, in order to correct for this selection effect in the real data, we would have to *reverse* the offset from this test, resulting in an underlying population that is older, more metal-poor and more α-enhanced with greater scatter in all parameters at dispersions $\log(\sigma) < 1.85$. The dashed black lines show our best estimate of the underlying population parameters after correction for this effect.

Chapter 4

Comparison of Models With Low Redshift Observations

For each model, we now have stellar population parameters and derived parameters, such as magnitudes and colours, for a synthetic cluster galaxy population. We can now compare these to independent observations in order to constrain the model. Later in this section, we will compare the predictions to scaling relations such as the FP. We begin however with a comparison sensitive only to the stellar populations: the colour-σ relation.

4.1 Comparison of Colour$-\sigma$ Relations

Figure 4.1 compares predicted $u-g$, $g-i$ and $i-K$ colours in our models to the Coma cluster data measured in an aperture of the same physical size (~ 0.95 kpc, 2") as the Shapley line index data. The quantitative comparisons are restricted to galaxies with cluster-centric radii $r_{200}/2$ to match our models derived from the central regions of Shapley clusters.

Although variable α-enhancement is used to fit the line indices using the models of Thomas et al. (2003, 2004), the stellar M_*/L predictions of Maraston (2005) do not allow for the effect of α-enhancement. We can estimate the effects of α-enhancement using the models of Coelho et al. (2007), who compute tracks and colours for an α-enhanced model as well as models with solar abundance ratios. Their colours are tabulated as a function of [Fe/H] and [α/Fe]. Fitting the colours as a function of age, α-enhancement, and metallicity (where [Z/H] = [Fe/H] + 0.75[α/Fe] for the enhancement pattern adopted by Coelho et al.

(2007)), we can find the differential effect of [α/Fe] (at fixed [Z/H]) on the colours. Since α-enhancement is a weak function of velocity dispersion, in principle both the slopes and the zero-points of the colour-σ relations could change. Using their self-consistent SSP model in a differential sense, ie. to derive an α-enhancement-dependent colour correction, we find that the optical colours shift blueward with increasing α-enhancement, at fixed Z/H. We illustrate this for the SSP case for $u-g$ and $g-i$ in Figure 4.1, where the lower SSP model is with α-enhancement.

Note that while our models do not allow for dust, in reality, of course dust may be present, particularly for low-σ galaxies, that may be of later morphological type. Correcting the data for this possible effect would shift the low-σ data blueward, and would make the slope steeper.

In $u-g$, without allowing for α-enhancement, all models are too red. The best fit slope is the FR model and all the other models overpredict the observed slope, by factors as large as 33% (SSP). However, if we allow for α-enhancement, the SSP prediction for $u-g$ shifts blueward by -0.090 at $\log\sigma = 1.84$ and -0.136 at $\log\sigma = 2.31$. This makes the SSP model very slightly bluer (by a few hundredths of a magnitude) than the Coma data, and flattens the slope to 0.45, in good agreement with the observed slope (0.43 ± 0.04). We have not calculated the effect of α-enhancement on the other models, but one might expect the sense of this correction to be the same as for the SSP case, i.e. to flatten the model slope and shift the model to bluer colours on average. Note that $u-g$ is, however, sensitive to dust, and so the small reddening of the data may be due to dust extinction.

In the $g-i$ colour, all of the models are again too red and, with the exception of the SSP model, are also too shallow compared to the data. The effect of α-enhancement is weaker in $g-i$ than in $u-g$: the models shift blueward by -0.026 at $\log\sigma = 1.84$ and -0.039 at $\log\sigma = 2.31$ for the SSP case. Thus allowing for α-enhancement, all models remain slightly too red (by ~ 0.04 mag in the SSP case), and of course, a disagreement in this direction cannot arise from dust. The SSP $(g-i)-\log\sigma$ slope flattens slightly to 0.25, but is still a reasonable fit to the slope of the data (0.31 ± 0.03). Maraston et al. (2009) have noted that, by using empirical libraries from Pickles (1998), the colours of solar-metallicity models change, particularly in g and r. However, the sense of the change would be to make the models even redder in g-i. In contrast to the good agreement with the α-enhancement-corrected SSP case, the "mostly-old" models (EXP, FR, OSP) have slopes only two-thirds of that observed before considering α-enhancement, which one expects would flatten them further. Furthermore, correcting for dust, if preferentially present in low-σ galaxies, would steepen the observed slope, exacerbating the conflict with the "mostly-old" models.

In $i-K$, again the model slopes are all too shallow. The OSP model has the strongest

metallicity trend, and since $i-K$ is more metallicity sensitive than age sensitive, it yields the steepest $i-K$ slope. However, the SSP model is the next steepest model after the OSP case. While the models of Coelho et al. (2007) do not predict the effect of α-enhancement on $i-K$, those of Percival et al. (2009) do predict its effect on $I-K$: ~ 0.04 for the α-enhancement relevant at $\sigma \gtrsim 70$ km s^{-1}. Thus qualitatively we would expect α-enhancement to shift colours to the blue and very slightly flatten the predicted colour-σ relation, as with the optical colours.

We conclude that, overall, the SSP model and, to a lesser extent, the AQ model are good fits to the optical colour-σ slopes, once the effects of α-enhancement are accounted for. The FR and EXP models do not fit the observed trends well in $g-i$. None of the models fit the observed $i-K$ slope well, even the OSP model which has a strong dependence of metallicity on σ. The comparison of colour-σ zero-points is less certain, particularly because of the effects of α-enhancement and of dust. No model fits the zero-point of, for example, $g-i$, although the SSP model zero-point is closest to the Coma data. We conclude that colours are not a strong discriminant of the CSFH models.

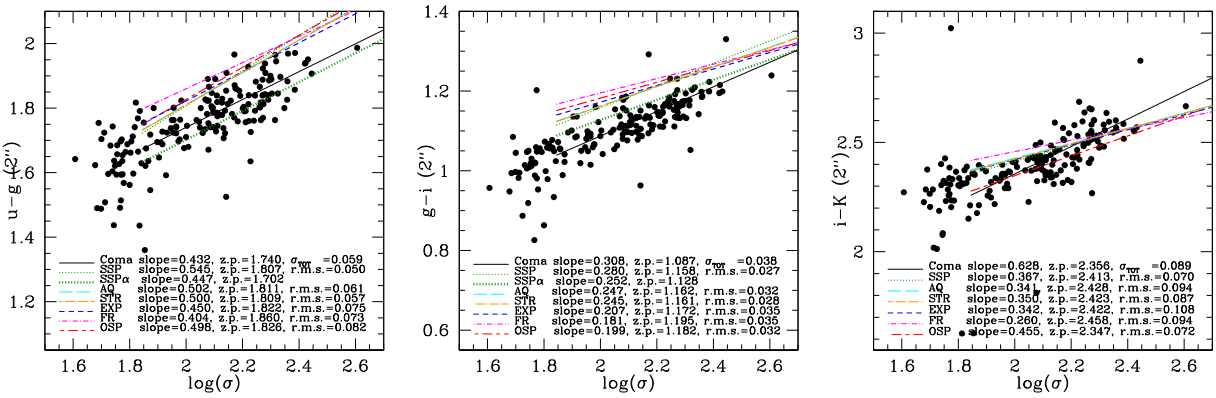

Figure 4.1 Colour - σ relations compared to model predictions. Colours are measured in a 2" aperture on Coma to match the 1" aperture of the Shapley data, at twice the distance. Fits to the Coma data are shown by the solid line, and robust fits to the medians, hence insensitive to outliers. Only galaxies within $r_{200}/2$ (filled circles) and $\sigma > 70$km s^{-1} are used in the fit. Line styles and colours as in Fig. 3.1, except for the heavy green dotted line is the SSP model with a correction for α-enhancement. The α-enhancement-correction reduces the colour offsets in $u-g$ and $g-i$, as discussed in the text.

4.2 The Faber-Jackson Relation

As described in Section 3.3.3, stellar masses are generated based on the observed $R_e - \sigma$ relation, and from these and the mass-to-light ratios one can calculate magnitudes and surface brightnesses.

Figure 4.2 illustrates the resulting Faber-Jackson (FJ) relations both for the Coma data and the models. Note that over the range of velocity dispersions covered here, the observed slope of the FJ is close to -5, i.e. $L \propto \sigma^2$. This is in agreement with previous work (Matković & Guzmán, 2005). Only at large velocity dispersions ($\log(\sigma) > 2.23$) does FJ approach the "classical" relation $L \propto \sigma^4$. This change in slope is a direct result of the change in slope of the $\log(R_e) - \log(\sigma)$ relation discussed above (Section 3.3.3). The FJ relation is not a strong model discriminator because its slope and scatter are driven by the $\log(R_e) - \log(\sigma)$ relation, and not by stellar populations and their associated mass-to-light ratios.

4.3 The Fundamental Plane

The FP is considerably tighter than the FJ relation, and hence offers a more powerful test of dynamical mass-to-light ratios. Figure 4.3 shows the r-band FP data for Coma where we have chosen to regress the combination $[\log(R_e) - 0.32\langle\mu_e\rangle]$ on $\log\sigma$.

If the tilt of the FP with respect to the virial relation were due only to variation in average stellar populations as a function of σ, then we would expect the slope of the model FP to agree with that of the Coma data. Thus the observed slope can be used to determine the additional tilt that is due to DM and/or non-homology. We find that the SSP and AQ models require the least additional tilt from DM & non-homology. We discuss this in more detail in Section 4.5.3 below. Furthermore, the "mostly-old" (EXP, FR, OSP) models predict a surface brightness too faint compared to the data, at low velocity dispersions and at a fixed effective radius. The addition of dark matter would exacerbate this situation as it would increase the predicted velocity dispersion and so would move the models further to the right.

An alternative way to address this issue is by constructing the *dynamical* mass-to-light ratio directly from the observed FP parameters (Dressler et al., 1987; Bender et al., 1992; Jorgensen et al., 1996). These can then be compared to *stellar* mass-to-light ratio predictions, as shown in Fig. 4.4. Because our modeled M_r and $\langle\mu_e\rangle$ are dependent on the Coma $R_e - \sigma$ relation (Equation 2.2 and Section 3.3.3), comparison of observed

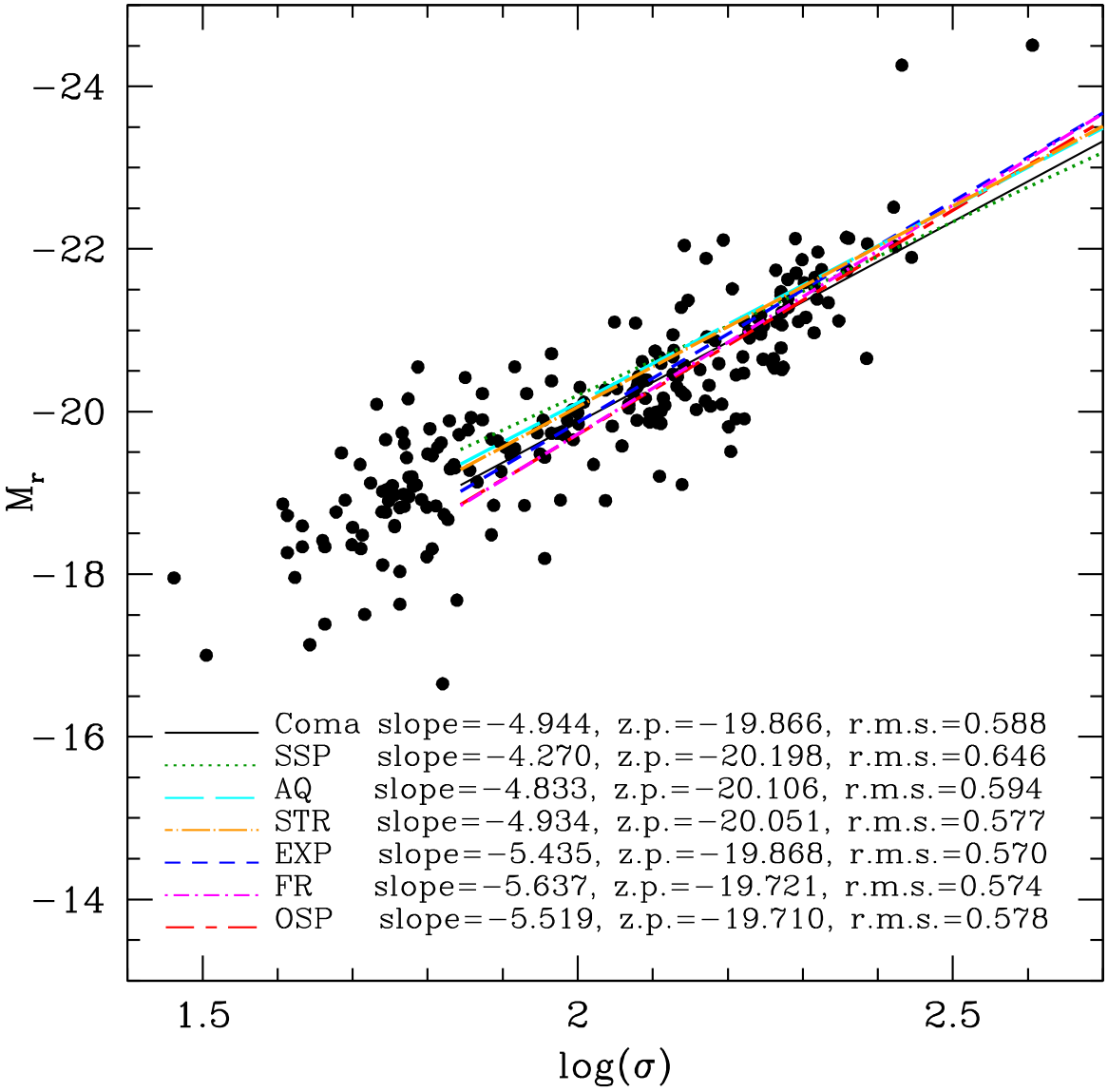

Figure 4.2 Coma Faber-Jackson relation compared to model predictions. Line styles and colours are as in Fig. 3.1. The fit to Coma data uses galaxies within a cluster-centric $r_{200}/2$ only and with $\sigma > 70$ km s^{-1}. Note the transition in the data from $L \propto \sigma^2$ to $L \propto \sigma^4$ at $\log \sigma \sim 2.2$, resulting from break in the $R_e - \sigma$ relation (Figure 2.2). The same transition is seen in FJ of the synthetic clusters, but here we simply plot the best linear fit to their FJ relation.

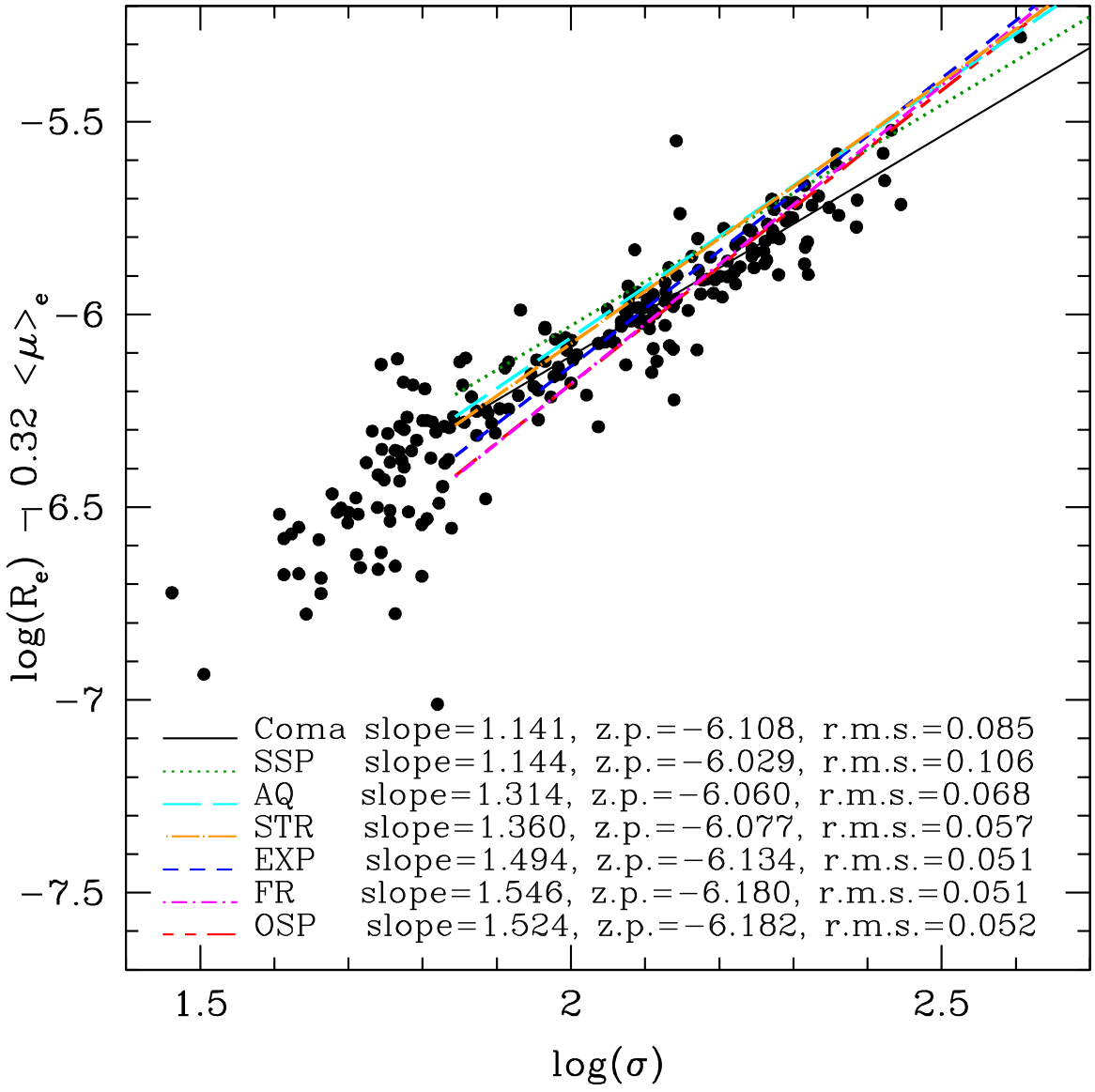

Figure 4.3 The Fundamental Plane. The r-band data from Coma are reproduced in each panel by the filled circles. The scatter in $[\log(R_e) - 0.32\langle\mu_e\rangle]$ for Coma is 0.085. Line styles and colours are as in Fig. 3.1. In order of increasing extra "tilt" relative to the data, these are SSP, AQ, STR, EXP, FR and OSP. We note however that the SSP slightly overproduces the scatter in the FP. However all models, with the exception of SSP and AQ predict, at fixed R_e, too faint a surface brightness at low σ.

$(M_{\rm dyn}/L)_{FP}$ to our modeled M_*/L provides the most direct comparison as our models are now independent of the data. The most striking aspect of this is how closely the Coma dynamical M/L, as a function of σ, follows the distribution of stellar *ages* as a function of σ (see Fig. 3.2). Specifically we see the same steep slope at high σ and the same upturn or flattening, and increased scatter at low σ. This strongly suggests that the FP tilt and scatter are driven primarily by stellar age effects.

As with Fig. 4.3, the additional tilt of the SSP model (i.e. the tilt that is attributable to dark matter and/or non-homology, in addition to the stellar populations), is small. However, as also noted above, at $\log\sigma = 1.844$, the OSP, FR and EXP models overpredict the FP-based mass-to-light ratios at the low-σ end by factors 1.45 - 1.7. The numerical values are given in Table 4.1. In contrast, the SSP leaves some room ($\sim 20\%$) for dark matter.

4.4 Comparison to Dynamical Mass-to-Light Ratios

A more direct comparison is with dynamical mass-to-light ratios in the I and K-band from the Schwarzchild model of the SAURON (Spectroscopic Areal Unit for Research on Optical Nebulae) group (Cappellari et al., 2006). The SAURON results are based on full orbit reconstruction using the observed luminosity profile and the observed line-of-sight velocity distribution. Their method thus accounts for spatial and kinematic non-homology and so a comparison between a given model and the data allow us to determine the fraction of dark matter as a function of velocity dispersion. Fig. 4.5 compares the stellar mass-to-light ratios of our synthetic galaxies with the data from Cappellari et al. (2006), as a function of velocity dispersion[1]. We find that the slopes of the OSP, EXP, and FR models are much flatter than the SAURON mass-to-light ratios. The AQ and STR models are less flat and the SSP slope is a close match. As noted above the masses determined by Cappellari et al. (2006) include both dark and stellar matter, whereas our TMBK models predict only the stellar mass-to-light ratio. Note that aperture effects are small: correcting to R_e (where the Cappellari et al. (2006) mass-to-light ratios are measured) yields changes in $\log(M_*/L) < 0.01$. Thus a serious problem with the OSP, FR and EXP models is that they predict *stellar M_*/L_I in excess of the total $M_{\rm dyn}/L_I$*, by significant factors (1.93, 1.91 and 1.67, respectively) at $\log\sigma = 1.844$. On this basis, these models are ruled out.

[1]Note that the Cappellari et al. (2006) data tabulate σ_e, the velocity dispersion at the effective radius, whereas our velocity dispersions are measured at a fixed metric aperture of 0.95 kpc radius. For most of the velocity dispersion range, R_e is constant (Fig. 2.2). Since the velocity dispersion aperture correction is $\sigma/\sigma_e = (R_{\rm ap}/R_e)^{-0.06}$, this yields $\log\sigma_e = \log\sigma - 0.015$, which is a negligible correction.

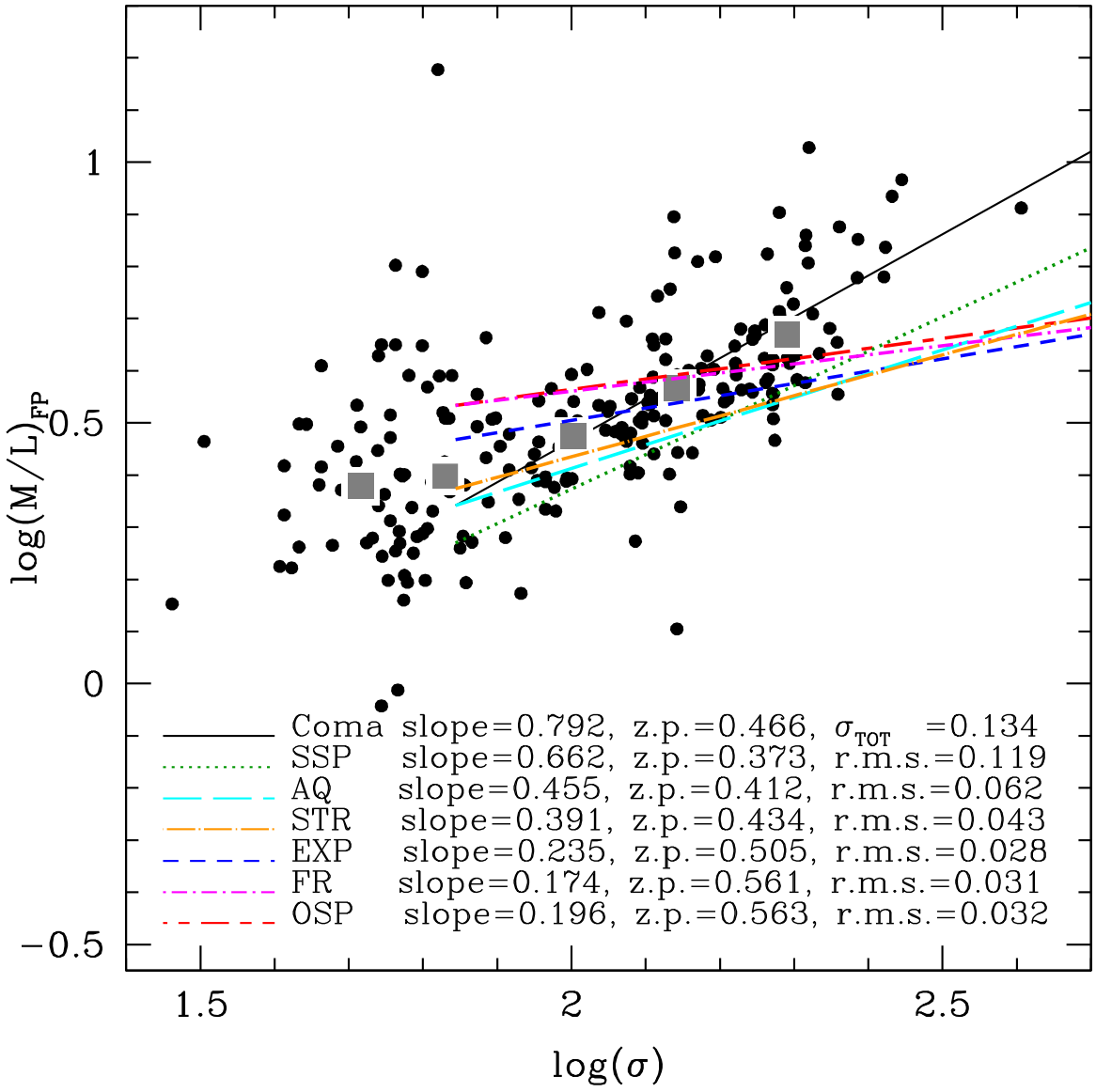

Figure 4.4 The r-band mass-to-light ratio data from Coma. Observed data from the Coma Cluster are shown as black points, and the fit to these is indicated by the solid black line. Binned medians are plotted as grey squares. These bins represent the same $\log(\sigma)$ ranges used when fitting to Shapley (see Table 3.2). Model fits to the *stellar* M_*/L are shown by the coloured broken lines (line styles and colours as in Fig. 3.1). Again, we only fit these lines to $\log(\sigma) > 1.844$, see Section 3.3.4. We find the models consisting of intermediate mass stars (SSP, AQ, and STR) fit best, whereas the models consisting of old stars (OSP, FR, EXP) fit the poorest. Note here that the SSP and AQ models underpredict $M_{\rm FP}/L$ at all σ's which implies dark matter is required.

However, note that even the AQ model has a stellar M_*/L_I 26% larger than the data. Table 4.1 outlines the offsets between data and model at $\log(\sigma) = 1.844$.

Consistent dynamical mass-to-light scaling relations are found in other dynamical studies. For example, van der Marel & van Dokkum (2007), using a compilation of data sources including Cappellari et al. (2006), find a steep relation in the B-band, with $M_{\rm dyn}/L_B \propto \sigma^{0.992\pm0.054}$. This is significantly steeper than all models except for SSP, for which the slope is 0.773 in the B-band. Their intercept at $\sigma = 100$ km/s is $\log(M/L) = 0.597$, and is consistent with the SSP model, but, as was the case with the I-band, is larger than that of all other models at low velocity dispersion.

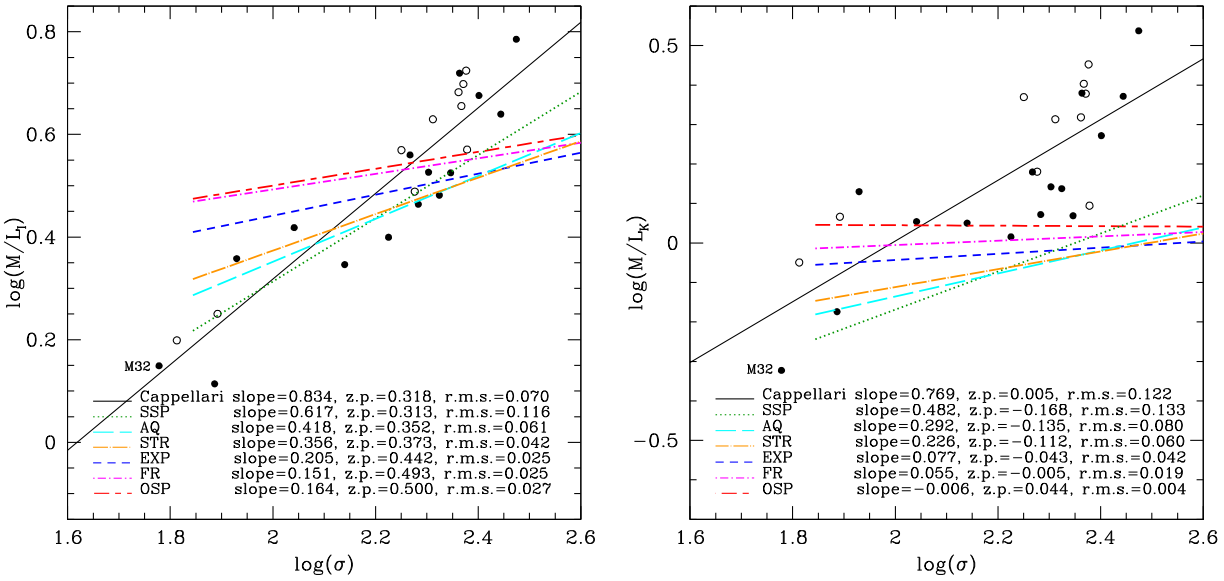

Figure 4.5 Mass-to-light ratios as a function of velocity dispersion. The left hand panel shows results in the I-band; K-band results are shown on the right. The *dynamical* mass-to-light ratios from SAURON (Cappellari et al., 2006) are shown by the black points (open circles are field galaxies, filled circles are cluster galaxies), and the fit to these is indicated by the solid black line. Model fits to the *stellar* M_*/L are shown by the coloured broken lines (line styles and colours as in Fig. 3.1). Again, we only fit these lines to $\log(\sigma) > 1.844$, see Section 3.3.4. Note that all models except for SSP overpredict the M/L at low σ. The models consisting mostly of old stars (OSP, FR, EXP) are the poorest fits at low σ.

From Figure 4.5, we see that for the SSP case, stellar populations account for 74% of the total observed $M_{\rm dyn}/L_I$ "tilt". Even in the K-band, 63% of the tilt is due to stellar

Table 4.1 M/L Offsets at Low Velocity Dispersion

Model	$\Delta \log(M/L_I)^{\rm a}$	$\Delta \log(M/L_K)^{\rm a}$	$\Delta \log(M/L_r)^{\rm b}$
SSP	+0.029	-0.128	-0.092
AQ	+0.099	-0.066	+0.00
STR	+0.129	-0.032	+0.027
EXP	+0.222	+0.060	+0.157
FR	+0.281	+0.101	+0.239
OSP	+0.286	+0.160	+0.235

[a]Offset between data and model at $\log(\sigma) = 1.844$, see Fig. 4.5

[b]Offset between data and model at $\log(\sigma) = 1.844$, see Fig. 4.3

population effects. These reduce to 50% and 38% for the AQ model. For consistency between our models and the SAURON data, we require the baryonic-mass to total-mass ratio to scale as $f_* \propto \sigma^{-0.22}$ for SSP, and $\propto \sigma^{-0.42}$ for the AQ case.

The SAURON data are a mixture of cluster and field early-type galaxies, and it may be argued that it is not well-matched to our predictions, which were derived from cluster galaxies alone. It is clear from Fig. 4.5, however, that there is no significant difference between cluster and field galaxies in $M_{\rm dyn}/L$. At low velocity dispersions ($\sigma < 100\,{\rm km\,s^{-1}}$) there are 5 galaxies: Cappellari et al. (2006) assign three of these to clusters (although one of these is M32) and the other two to the field. Their Hβ values range from 2-3 according to their Fig. 16, the upper end of which is larger than our median value of 2.05 at the same velocity dispersions. Interestingly, one of the high Hβ, low M/L galaxies is a cluster member. We have investigated how the slopes of the SAURON M/L relations are affected by dropping between 2 and 4 of the SAURON galaxies with the highest $H\beta$ (and hence lowest $M_{\rm dyn}/L$). We find that this does not significantly affect our conclusions: the "mostly-old" class of model, when tuned to reproduce the observed spectral indices, yields stellar M/L ratios that are too large compared to the dynamical values.

4.5 Extending the Models

Our models as described above are necessarily simplistic. In this section we explore the effects on our results of (i) systematics, (ii) altering the IMF, and (iii) adding dark matter.

4.5.1 Systematic Effects on Mass-to-Light Ratios and Colours

As mentioned in Section 3.2.2, the arbitrary choice of restricting the star formation of CSFH models to begin at a look-back time of $t_{\rm start} = 13$ Gyr requires investigation. Again, we choose a look-back time of 10.3 Gyr for comparison, which corresponds to $z \sim 2$. First, we note the effect on the colours and mass-to-light ratios of the choice of $t_{\rm start}$ is small. In all models, we find that, if the star formation starts at 10.3 Gyr then, *at the fixed observed values of the line indices*, the predicted stellar M_*/L values are slightly higher than in the case with $t_{\rm start} = 13$ Gyr, with the effect being largest for the bluest bands. This arises because, for example in the case of the EXP model, when $t_{\rm start}$ is decreased, then in order to fit the observed line indices, τ is also reduced compared to the $t_{\rm start} = 13$ Gyr case, with the consequence that M_*/L increases. Other models are affected in a similar way. In the r and I bands in the mid-σ range, we find a 12% increase in M_*/L for the EXP model and 7% increase for the AQ model. For all models, the slope of the M_*/L -σ relations are negligibly affected by the choice of $t_{\rm start}$. Colours are also largely unaffected by this choice, with the largest offset being for the bluest bands. This offset in colour towards the blue is $\lesssim 0.05$ in magnitude for all colours given in Tables 3.6 and 3.7, for all velocity dispersion bins, in all models, compared to the 13 Gyr case. This effect can be explained as follows: although $t_{\rm start}$ is now more recent, the constraint on fitting the line indices forces the fitted 'age' towards older populations, as discussed in detail in Section 3.2.2. Because the mass-to-light ratios are even higher when star formation starts later, this test strengthens the conclusion that the 'mostly-old' models (EXP, FR, OSP) are a poor fit.

Next we consider the effect of Balmer line choice, as discussed in Section 3.2.2. In that Section, we found that, for example, fitting only the Hβ Balmer line had the largest effect on the ages[2]. As with the choice of $t_{\rm start}$, the effect of using only Hβ on the predicted colours is negligible. The effect on stellar mass-to-light ratios is somewhat greater: for the SSP model, this choice leads to a decrease in mass-to-light ratios on the order of 10% at $\log \sigma \sim 1.85$ in the r, I and K bands. For the EXP and FR model, however, only a 3% and 1% decreases in M_*/L are found. Thus, this effect is too small to avoid our rejection of the FR and EXP models as discussed in Section 4.4, as these models would still overpredict the stellar mass-to-light ratios at low velocity dispersion, albeit by a slightly lesser amount.

[2]We note that the other scenarios, such as calibrating the Hβ line using all velocity dispersion bins, had a much smaller effect on the ages (see Figure 3.4), and hence presumably on the mass-to-light ratios, and so we do not discuss those here.

4.5.2 Choice of IMF

In calculating stellar mass-to-light ratios, we have adopted the Kroupa (2001) IMF. Other choices often considered in the literature are the Salpeter (1955) and Chabrier (2003) IMFs. These models have similar slopes at high masses, but differ in the low mass ($M < 1M_{\odot}$) regime: while the Salpeter IMF is a pure power-law, the Kroupa and Chabrier IMFs have knees at masses of $0.5M_{\odot}$ and $1M_{\odot}$ respectively. We expect the choice of IMF to have little effect on the derived stellar ages and metallicities, since most of the light is from main-sequence turn-off and red-giant branch stars. For the ages considered here (2 Gyr to 13 Gyr), the turn-off masses are well above the IMF "knee".

The choice of IMF, however, has greater impact on the stellar mass-to-light ratios. Using the Salpeter IMF would increase the M_*/L ratios by a factor of ~ 1.6 (Thomas et al., 2005) and so would *increase* the conflict for all models at low σ between the stellar and dynamic mass-to-light ratios from the SAURON and FP comparisons. The Chabrier IMF produces marginally lower stellar mass-to-light ratios compared to a Kroupa IMF, but this would be insufficient to reconcile the OSP, EXP and FR models with the dynamical mass-to-light ratios.

More radical IMF modifications have been suggested by van Dokkum (2008), who proposes an IMF in which the critical mass at the knee varies as a function of age, with older populations having higher critical masses. It is difficult to compare the results of this model in detail, as full population synthesis models have yet to be constructed. Referring to van Dokkum (2008) Figure 15, the effects on M_*/L may be modest, amounting to at most a 20% reduction compared to the Chabrier IMF for a 3 Gyr population. It seems very difficult to reduce the high stellar M/L values of the FR and OSP models, as most of their population is old, and for older populations with a larger critical mass ($M_c \gtrsim 0.3M_{\odot}$), M_*/L actually increases due to remnants.

We conclude that the choice of IMF cannot lower the stellar mass-to-light ratios sufficiently to ease the conflict with the OSP, FR and EXP models.

4.5.3 Effects of Dark Matter and Non-homology

For simplicity, our models have been assumed to be 100% stellar, i.e. $f_* = 1$. Various studies have suggested that, like spiral galaxies, early-type galaxies also have non-negligible mass fractions of dark matter (DM) in their central regions. For example, from lensing studies, Bolton et al. (2008) find $f_* = 0.62 \pm 0.07$ within the effective radius, for galaxies

with $175\mathrm{km\,s^{-1}} < \sigma < 400\mathrm{km\,s^{-1}}$. It is clear that adding DM will increase the total mass-to-light ratios by a factor $1/f_*$. As noted above, the OSP, EXP and FR models already over-predict the dynamical M/L for low σ galaxies, so including DM would only increase the conflict.

The combined influence of DM and non-homology can also be deduced from the tilt of the FP. This 'tilt' is the intrinsic scaling of $M_{\rm dyn}/L$ with mass or luminosity away from a constant value, due to variations in stellar populations and dark matter/non-homology. Following Boylan-Kolchin et al. (2006), let us assume a scaling $M_{\rm dyn} \propto M_*^{1+\mu} R_e^{\nu}$. We define the scaling of the stellar mass-to-light as a function of σ as $(M_*/L) \propto \sigma^m$, where the value of m is given as a function of model and passband in Table 3.7. The theoretical FP

$$R_e = (M_{\rm dyn}/L)^{-1} \frac{c_2}{2\pi} \sigma^2 \langle I_e \rangle^{-1} \tag{4.1}$$

becomes

$$\begin{aligned} \log(R_e) \quad \propto \quad & \left(\frac{2 - m(1+\mu)}{1 + \nu + 2\mu} \right) \log(\sigma) \\ & - \left(\frac{1+\mu}{1+\nu+2\mu} \right) \log\langle I_e \rangle \end{aligned} \tag{4.2}$$

after allowing for stellar populations and dark matter/non-homology. If we assume that the dynamical mass-to-light ratio scales with luminosity L as $M_{\rm dyn}/L \propto L^Y$ in Equation 4.1, knowing $L \propto I_e R_e^2$, and equate the coefficient of $\log \sigma$ (when measuring the proportionality to $\log(R_e)$) with that of Equation 4.2, then

$$Y = \frac{1}{\alpha} - \frac{1}{2} \tag{4.3}$$

where α is the coefficient of $\log \sigma$ in Equation 4.2. If we assume that the dynamical mass-to-light ratio scales with mass M as $M_{\rm dyn}/L \propto M^T$, then the "tilt" T of the FP (or scaling of $M_{\rm dyn}/L$ with mass due to the combined effect of stellar populations and dark matter/non-homology) can be expressed as

$$T = \frac{Y}{1+Y} = \frac{2-\alpha}{2+\alpha} \tag{4.4}$$

We can also derive tilts for the cases with only stellar populations and no DM ($\mu = 0$, $\nu = 0$):

$$T_* = \frac{2-\alpha_*}{2+\alpha_*} = \frac{m}{4-m} \tag{4.5}$$

as well as with DM (either μ or ν non-zero).

Table 4.2 restates the value of m for each model from Table 3.7 in the r-band. We find that all of the models with the exception of the SSP are too steep (too high α, close to the virial relation) in comparison to the observed FP. We can then adjust the DM/non-homology scaling (the value of μ or ν) so as to match the observed FP slope in Figure 4.3. This yields the values in the second and third columns of Table 4.2. For the SSP model, the DM/non-homology scaling is essentially zero. For the other models, stronger scaling is required: for AQ $\mu = 0.06$, or $\nu = 0.150$. As a result, we find that in the SSP case, essentially all of the r-band FP tilt is due to stellar populations. For the AQ model, 2/3 of the tilt is due to stellar populations and 1/3 is due to DM and/or non-homology. Note that because of the age-dependence of the K-band stellar M/L, for the SSP case we find that most of the predicted K-band tilt is due to stellar population effects. In the case of the AQ model, we expect that half of the K-band tilt is due to stellar population effects.

If we repeat this exercise using the dynamical M_{FP}/L values calculated from the FP and shown in Fig. 4.4, we can determine the tilt assuming that dark matter and non-homology depend directly on σ. For the SSP case, we find that $f_* \propto \sigma^{-0.13}$ and for the AQ case the exponent is -0.34. To extend these scaling relations to the case of non-homology, replace f_* with the combination $f_*(c_2/5)$. These scalings are slightly flatter than the corresponding values derived from the SAURON comparison: $f_* \propto \sigma^{-0.22}$ and $\propto \sigma^{-0.42}$, respectively. Since the SAURON results are free of the effects of non-homology, the comparison between the FP and SAURON scalings then yields $c_2 \propto \sigma^{0.09}$ for both SSP and AQ cases. This non-homology is weak, and is not a major driver of the tilt of the FP.

Table 4.2 Effect of Dark Matter on r-band FP Tilt

Model	m^{a}	μ^{b}	ν^{c}	${T_*}^{\mathrm{d}}$	T^{e}	T_*/T^{f}
SSP	0.662	0.001	0.003	0.198	0.200	0.993
AQ	0.455	0.065	0.150	0.128	0.197	0.652
STR	0.391	0.085	0.190	0.108	0.194	0.558
EXP	0.235	0.140	0.310	0.062	0.194	0.322
FR	0.174	0.165	0.355	0.045	0.194	0.234
OSP	0.196	0.155	0.340	0.052	0.194	0.270

[a] $(M_*/L)_r \propto \sigma^m$. From table 3.7

[b] μ required in eq. 4.2 (with $\nu = 0$) to reproduce the $\log(\sigma)$ coefficient in the observed Coma FP.

[c] same as (b), but with $\mu = 0$

[d] $M_*/L \propto M^{T_*}$: tilt due to stellar populations

[e] $M/L \propto M^T$: tilt of the FP

[f] T_*/T is the fraction of the tilt due to stellar populations

Chapter 5

Comparison of Models With High Redshift Observations

5.1 Introduction

One of the major limitations in the study of galaxy evolution is the inability to observe a single galaxy evolve. Instead, statistical analyses must be done on similarly selected populations at different redshifts, and conclusions are drawn as to their apparent evolution. Our study provides a unique opportunity to predict the evolution of simulated galaxies onto the red-sequence, at all lookback times. We will show that for each model the red-sequence is built in a unique manner, providing a possible way to distinguish between them, and more importantly, gain insight into how the red-sequence is built-up. In Chapter 4 at low redshift we found that models of intermediate age reproduced the red-sequence properties the best. Here we wish to test if these models will continue to be favoured when compared to high redshift data.

Early studies of ellipticals in clusters in the local universe have shown that their colour-magnitude relations are identical, and thus universal (Bower et al., 1992). However, debate as to the origin of the CMR at high redshift still continues today. Early studies of high redshift cluster elliptical CMRs strongly suggested a purely passive red-sequence evolution out to $z \sim 1$ (for example: Dressler & Gunn (1990), Aragon-Salamanca et al. (1993), Rakos & Schombert (1995)). The study of Kodama & Arimoto (1997) attempted to disentangle the age-metallicity degeneracy of high redshift ellipticals by constructing two extreme models: a pure metallicity sequence (quite similar to our OSP model) without α-enhancement and a formation start time of 15Gyr, and a pure age sequence, varying age and fixing a solar

metallicity. They conclude that age cannot be the dominant effect as it cannot produce the observed faint red-sequence members at high redshift, and thus the red-sequence is dominantly a metallicity sequence. Later studies (Trager et al., 2000; Thomas et al., 2003; Nelan et al., 2005) showed the requirement for both age and metallicity variation along the red-sequence at low redshift (see also Section 3.2).

In this chapter, we wish to follow the red-sequence as it evolves with redshift. At any given redshift or lookback time, we can reproduce observables and compare to observations.

In order to generate synthetic high redshift clusters, we must make a few assumptions to simplify the analysis:

- The velocity dispersion of each synthetic galaxy is assumed to be constant with redshift.
- The chemical abundances remain constant, i.e., the fit z $\sim$ 0 metallicities and α-enhancements remain unchanged with redshift. This implies no feedback processes and more generally, no chemical evolution.

The implications of these assumptions are quantitatively unclear. We do know that galaxies evolve, be it morphologically or chemically (e.g. through mergers or feedback processes). It is our assumption that any un-introduced scatter in predicted trends is on par with observed selection biases, or perhaps the uncertainty in our correlated scatter. Thus, we assume they should have a qualitatively negligible effect on our results.

In addition to these assumptions, we have altered the generation of the synthetic clusters as follows:

- As addressed in Section 3.3.4, the scatter in model parameters at low velocity dispersion is uncertain, and likely pinching due to selection effects. In order for our synthetic clusters to be complete, we must extrapolate these fits to low velocity dispersion. In order to allow this extrapolation to occur without odd extremes in scatter, we have forced the residual scatters of metallicity and α-enhancement to be constant (excluding the OSP model), at a nominal average from the fits found in Section 3.2 ($S([Z/H])_{res} = 0.09$, $S([\alpha/Fe])_{res} = 0.04$). The overall scatter is then refit for all velocity dispersion bins. Finally, the 'age' scatter in the lowest two velocity dispersion bins are forced to be equal, at the average of the two fit values.
- We have rescaled the faint end slope of the VDD of Section 3.3.1 derived from Sheth et al. (2003), to match the z $\sim$ 0 dwarf-to-giant ratio (DGR) of Lu et al. (2009). To

do so, we employ the fact that all our synthetic galaxies at redshift of zero lie on the red-sequence. We then apply defintion of luminous (giant) and faint (dwarf) bins of De Lucia et al. (2007) and iteratively rescale the distribution to produce a DGR of just over ~ 2. This value was decided upon as a compromise between Lu et al. (2009) and recent data collected. See Section 5.2.1 for further detail into the red-sequence selection technique.

5.1.1 Selection Effects and Biases

A big challenge with comparing our work to high redshift studies, is the identification and emulation of selection effects. In reality, no sample will ever be truly representative of the universal truth. Repeated tests with smaller samples help narrow down the statistical uncertainty in measurement of this universal truth. Yet, if these repeated samples all are biased in some way, repeated sampling will not help. Here we outline some selection effects we take note of during our analysis.

An issue that affects all observations is the magnitude limit. As new telescopes are being built with larger collecting areas, these limits are being hammered down. However, there will always be a limit to how faint an object can be to be observed, and astronomers will always be pushing this limit. In general, it is good practice to regress data against the value that is limited, i.e., magnitude in this case. This is not always feasible though, and as such, a selection effect is born. We will show in Section 5.4 that in some cases, magnitude limits may appear as a diagonal selection when linearly regressing against observables other than magnitude, such as the M/L vs. mass relation. Because x and y are correlated in the M/L-M relation, a constant luminosity will appear as a diagonal line. This effect will skew the line of best fit away from the true value. Although inevitable, these effects must be noted and accounted for whenever possible.

One of the implicit assumptions made in our study of high redshift early-type galaxies is that their distribution remains unchanged, without any morphological evolution. However, this assumption may not be true. The progenitors of today's red-sequence were not necessarily always early-types, as they perhaps formed from spirals or mergers at high redshift. There is evidence for a significant decrease in S0 population at high redshift which might be indicative of morphological transformation and migration to the red-sequence (Dressler et al., 1999; Poggianti et al., 2006). These galaxies would not be included in the high redshift sample in comparing properties to their low redshift counterparts. This progenitor bias (van Dokkum & Franx, 2001) preferentially selects the oldest progenitors of today's red-sequence, and does not fully (if at all) represent the progenitors of early-types that

have very recently become red. Despite the assumptions we've made about our models, we have the unique opportunity to model all progenitors of today's red-sequence, by winding our models back in time.

5.2 Colour-Magnitude Relation

The colour-magnitude relation has been extensively studied in the local universe (for example: Bower et al. (1992); van Dokkum et al. (1998); Hogg et al. (2004); López-Cruz et al. (2004); Baldry et al. (2004); Bell et al. (2004); Bernardi et al. (2005); McIntosh et al. (2005); Gallazzi et al. (2006); De Lucia et al. (2007); Mei et al. (2009)) and at higher redshift (for example: Ellis et al. (1997); van Dokkum & Franx (2001); De Lucia et al. (2007); Mei et al. (2009)) as a tracer for galaxy formation. The bimodality of the distribution between the red-sequence and looser blue cloud, as well as the known correlation of early-types residing on the red-sequence, indicates a strong fundamental by-product of galaxy formation and evolution.

Figures 5.1, 5.2, 5.3, 5.4, illustrate the modeled evolution and formation of today's red-sequence for the OSP, EXP, FR, SSP, AQ, and STR star formation history models in $U-V$ vs. V. As we will discuss in the next section (5.2.1), defining the red-sequence in $U-V$ versus V is a natural choice if we intend to further define magnitude limits in the V band, as this eliminates any selection effects. At $z \sim 0$, all models appear relatively identical. However, as lookback time increases, we can see 6 very different stories being told. Qualitatively, we can compare these to high redshift CMRs to immediately remove those models which do not appear to follow the consensus picture of blue cloud - green valley - red-sequence progression as outlined in Section 1.2.2.

We can that see the SSP, AQ and STR models populate their red-sequences with galaxies beginning in the blue cloud and migrating up to the red. In general, at early times, the red-sequence appears in the process of being populated at all magnitudes, masses, and velocity dispersions. This migration ceases first at the bright end of the sequence, as the star formation in the most massive red-sequence progenitors shuts off earliest. As redshift decreases, this transition magnitude appears to shift to fainter magnitudes, with the population of the faint end of today's red-sequence being completed very recently. These three models, more so than the others, show slight curvature in their red-sequences. This is significant, as this curvature plays a direct role in the measurement of the dwarf-to-giant ratio detailed in Section 5.3 below. The SSP galaxies form their stars in a single burst, and migrate immediately and rapidly after they've formed. The AQ galaxies form a tight blue sequence before they migrate because as lookback time increases beyond t_{quench},

they appear blue due to current star formation. The lower limit of this blue sequence, or 'blue edge', is due to a few factors. Firstly, all galaxies experience the same t_{start}, and once the lookback time is greater than the quenching time, all galaxies appear relatively the same with respect to age. Thus, the small scatter seen in the blue sequence is due to the scatter in metallicity and α-enhancement. The 'blue edge' exists because the reddening effect due to sub-solar metallicity overcomes the effect of younger age, where the lookback time is greater than t_{quench}. In reality, we do not expect a tight sequence in the blue nor a 'blue edge', and thus these are artefacts of the over-simplification of the model. Had we also allowed a variable formation start time or allowed for dust reddening, the scatter in this sequence would increase. This predicted abundance of blue cluster members at intermediate/high redshift relative to low redshift is the trend known as the Butcher-Oemler effect (Butcher & Oemler, 1978, 1984), and the build-up of the red-sequence is a direct result of that.

The EXP model is not bimodal, in that it does not produce a distinct blue cloud and red-sequence. By definition stars form at all times, their abundance depending on the fit e-folding time. Therefore, there is no clear separation between blue and red in this model. At all redshifts, there are galaxies with stars that have just recently formed. This effect results in a sequence that simply rolls from blue to red in a relatively tight relationship. This is not the consensus picture of the CMR, and further disfavours the EXP model as an accurate star formation history. This model has been used extensively by authors as an assumed star formation history (Bell et al., 2003; Kauffmann et al., 2003) yet does not appear to be correct.

The STR model is a hybrid of the AQ and EXP models, and its red-sequence build-up reflects this. There is a slow progression from blue to red, although in this case, there is a clearer distinction between the two. Again, as the lookback time surpasses the quenching time, a tight blue sequence is formed. As seen in the SSP and AQ models, red-sequence build-up seems to complete from bright to faint magnitudes with decreasing redshift, with all magnitudes contributing at the earliest times.

The OSP and FR models evolve nearly identically, with a tight red-sequence at all times. The bulk of secondary bursts in the FR model occur between lookback times of 1 to 2 Gyr, which causes a stir of galaxies to shift from red to blue to red as the burst of new stars forms and dies. This is a non-standard picture of red-sequence build-up. At sufficiently high redshifts, the FR and OSP model appear nearly identical. The OSP model is the strawman 'old' population widely used as a formation history for early-type galaxies (Kodama & Arimoto, 1997). This apparent lack of red-sequence evolution, in stark contrast with studies of De Lucia et al. (2007); van den Bosch et al. (2008); Lu et al. (2009) which require a build-up of the red-sequence, all but removes the model as a possible candidate.

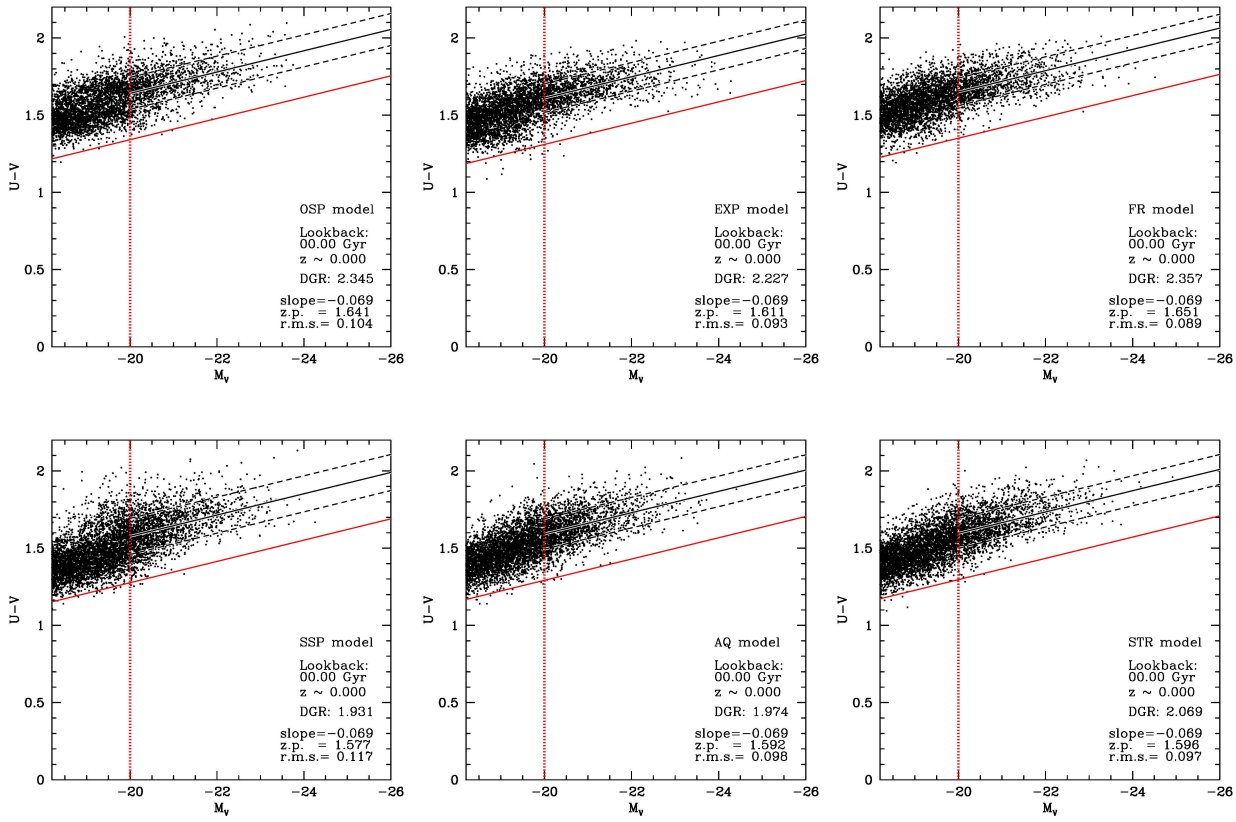

Figure 5.1 Present-day ($z \sim 0$) red-sequence CMR for the six models. The upper row consists of 'old age' models and bottom row of 'intermediate age' models. All slopes are identical and derived from the OSP fit, but each model has a freely fit zero point. The solid black line represents the line of best fit zero point of the OSP slope, with dashed black lines representing 1σ rms scatter. The red solid line represents the imposed 0.3 mag limit in selecting red-sequence members. The dashed red line represents the V band 'giant' limit of De Lucia et al. (2007). The left edge of the frame also indicates the corresponding 'dwarf' limit. Figures 5.2, 5.3, and 5.4, follow the models with increasing lookback time.

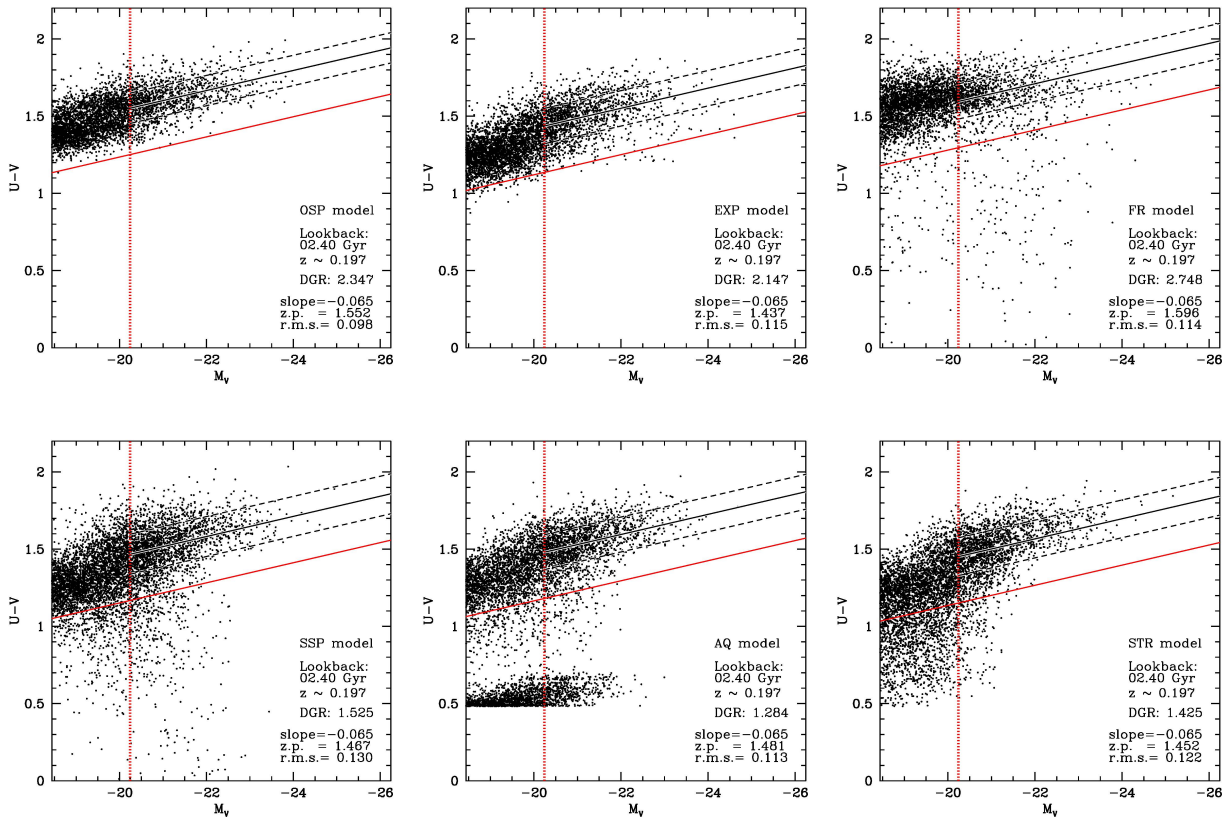

Figure 5.2 Modeled CMRs at $z \sim 0.2$. See caption of Figure 5.1. Note that the frame is passively evolved, such that the left edge of the frame remains at the 'dwarf' magnitude limit. It is evident that each model shows a different build-up of the red-sequence.

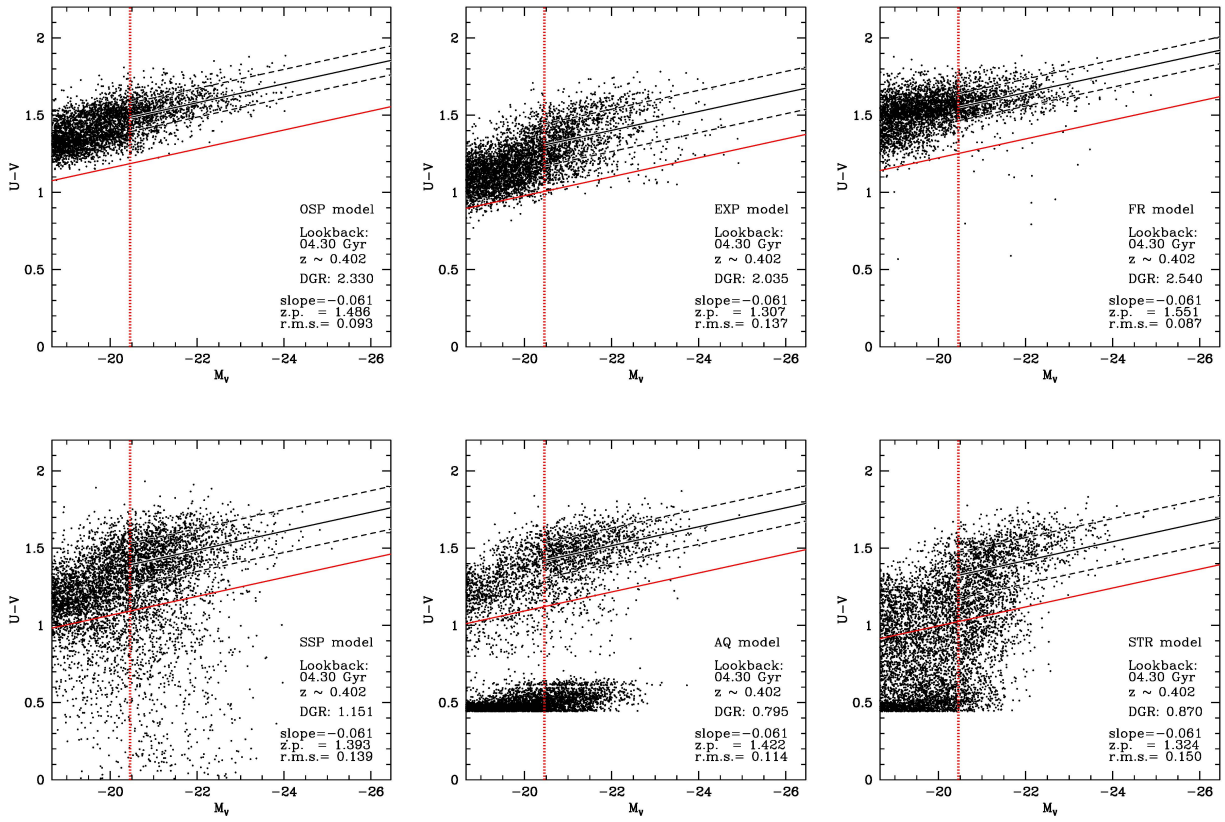

Figure 5.3 Modeled CMRs at $z \sim 0.4$. See captions of Figures 5.1 and 5.2.

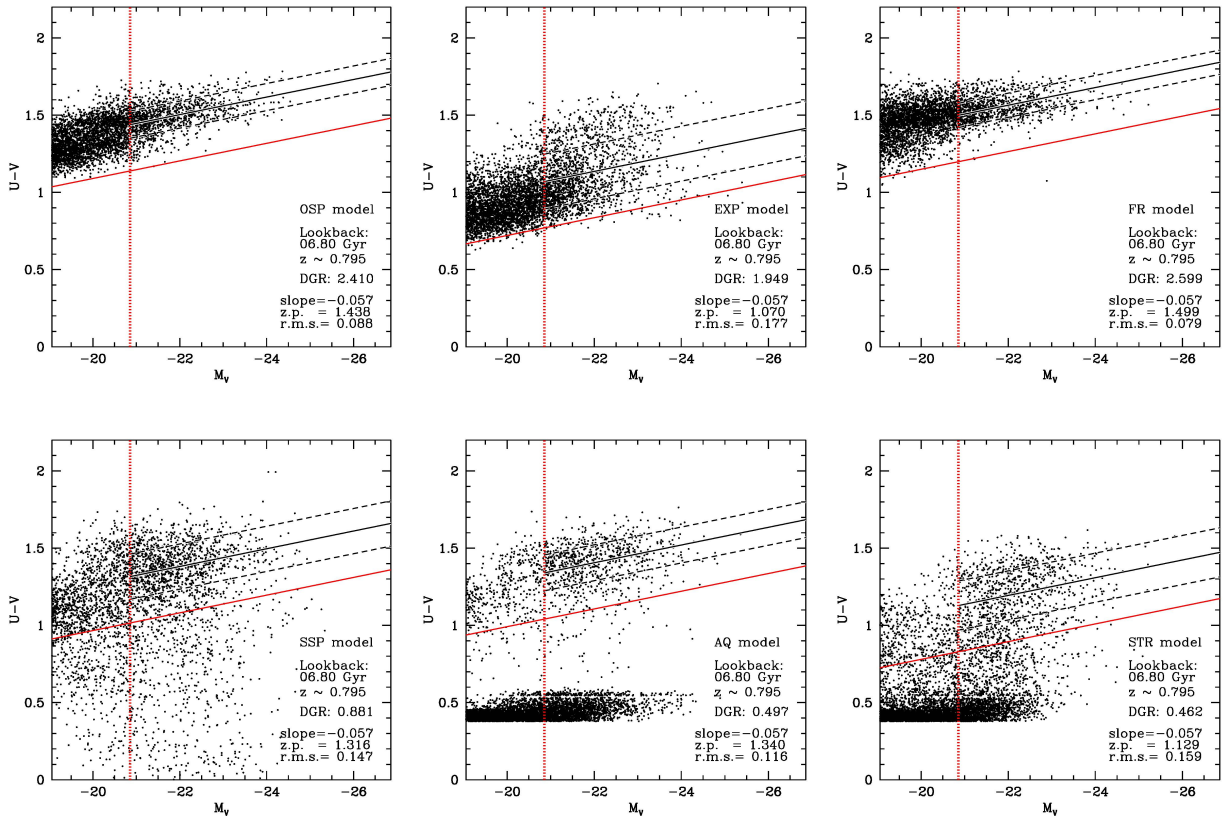

Figure 5.4 Modeled CMRs at $z \sim 0.8$. See captions of Figures 5.1 and 5.2.

5.2.1 Red-Sequence Selection Techniques

When making quantitative comparisons of high redshift red-sequence properties, as we wish to do here, it is important to understand the method used to isolate the red-sequence galaxies from other cluster members. Observationally this can be difficult and ambiguous, as surveys are based on different selection criteria. These could be morphology, colour, magnitude, or a combination, as mentioned in Section 1.2.2. These criteria are similar but not identical, and this needs to be considered when conclusions are drawn. I remind the reader that our selection criteria were based on each galaxy being emission-free. This is also not without flaw: a galaxy with small amounts of emission may still reside on the red-sequence, and would not be counted in our survey. Spectroscopically, emission would contaminate many markers we've used to which we've fit our models. Thus, our selection method serves our purpose well.

The first issue in red-sequence selection is deciding what parameters to isolate. High z observations usually entail colour-magnitude relations as photometric observations are easiest. Bower et al. (1992), Ellis et al. (1997), van Dokkum et al. (1998), De Lucia et al. (2007), to name a few have extensively studied the CMR at high redshift using various selection techniques. Lu et al. (2009) have performed an extensive study on RS selection and resulting RS luminosity function using the CFHTLS.

The colour chosen to isolate the red-sequence is technically arbitrary. The characteristic bimodality of the CMR is seen in any comparison between 'blue' and 'red' filters. As we will see however, observables such as the dwarf-to-giant ratio become sensitive to the limits placed on the selection.

De Lucia et al. (2007) select their $z \sim 0.4$ red-sequence members in observed $V - I$ vs. I, which is nearest to rest frame $U - V$ vs. V. They have assumed a fixed slope which is based on the Bruzual & Charlot (2003) passively evolved population with formation redshift ~ 3 using a Chabrier IMF. Hereafter this model will be considered and referred to as *the standard method* for passively evolving magnitudes, unless stated otherwise. However, because we have not used the models of Bruzual & Charlot (2003) to generate our populations, we have instead decided to freely fit a slope to our OSP modeled cluster, which is a better representation of an 'old' population in terms of the Maraston (2005) models fit to our data. For the other models when isolating the RS, the OSP slope is used and a free zero point is then fit to the red-sequence members brighter than the passively evolved 'giant' limit (see Section 5.3). The RS is defined as all galaxies redder than this line, as well as those which are bluer than it by no more than 0.3 mag in $U - V$. Iteratively, with increasing lookback time, galaxies will appear to 'fall off' the red-sequence and are then rejected. At each iteration a new red-sequence is isolated. Hereafter, this method of RS

isolation will be referred to as *the standard method*.

Figures 5.1, 5.2, 5.3, and 5.4 illustrate the standard method of red-sequence isolation and passively evolving magnitudes. The vertical line represents the 'giant' limit, and the leftmost edge of each frame also represents the 'dwarf' limit, defined by De Lucia et al. (2007) and discussed in Section 5.3.

5.2.2 Comparison to observations

Quantitatively, we wish to compare these different red-sequence evolutionary models to observed data. The study of Mei et al. (2009) isolates the red-sequence out to $z \sim 1$, in $U - B$ vs. B. They limit their fits to within R_{200} of the cluster centre, which is ideal for comparison with our $z \sim 0$ limitation of $R_{200}/2$ as we expect cluster infall with decreasing redshift. We can easily compare to this CMR, with minor corrections to allow for selection effects. Using the standard RS isolation method, we then follow the passively evolved $B-V$ using the standard method. Transforming the 'giant' limit in V to B band, we then fit a slope to this new red-sequence in $U - B$ vs. B. The resulting slope, zero point and rms scatter out to $z \sim 1$ are illustrated in Figure 5.5. Note that the data below $z \sim 0.7$ are taken from the literature for comparison, and are for elliptical galaxies only. Those above $z \sim 0.7$ are from the Mei et al. (2009) analysis of early-types (E+S0). As a result, the fit constant values (horizontal fits with 1σ scatter) are drawn from these high redshift data. Also note that the two most distant clusters are not considered in the zero-point fit due to the high uncertainty in their magnitude calibrations at the wavelengths where most of their galaxy light reside.

Somewhat surprisingly, Mei et al. (2009) find little to no evolution of the CMR between $0.7 < z < 1.3$. While we note that the CMR scatter in all models remains steady over the redshift range of their clusters (bottom panel of Figure 5.5), we do see a slight flattening of the CMR slope with increasing redshift across all models (middle panel of Figure 5.5). This flattening is strongest in the AQ (albeit 1σ shallower than observed), and OSP models over the observed redshift range. Had they decided also to ignore the problematic two most distant clusters from their analysis, the average observed slope $\pm 1\sigma$ would bracket all of our models. We also note a strongly evolving zero-point for all models (top panel of Figure 5.5), with the SSP model shallowing the most over the observed redshift range. The zero-point however, is strongly correlated and degenerate with slope in that, depending on where the zero point is measured, a small evolution of slope could mean a large evolution in zero point.

Mei et al. (2009) note that they are likely suffering from progenitor bias, due to their

selection technique. However, due to our selection of the red-sequence at these redshifts, the comparison of model and data should not be strongly dissimilar.

In general, the intermediate-age models appear more consistent with the observed CMR evolution of Mei et al. (2009), with the EXP and STR models showing the strongest deviation from the observed constant evolution. However, it is difficult to further distinguish the models as their predicted evolutions differ very little.

5.3 Dwarf-to-Giant Ratios

The dwarf-to-giant ratio (DGR) is a robust method with which to compare red-sequence luminosity functions (LFs), as it is essentially an LF split into 2 bins: dwarfs (faint) and giants (luminous). The concept of the dwarf-to-giant ratio was popularized by the study of De Lucia et al. (2004). Their analysis of red-sequence luminosity functions of $z \sim 0.8$ clusters showed a dip at faint magnitudes i.e., a deficit of faint galaxies. This deficit was later shown to evolve (De Lucia et al., 2007), with an increasing luminous-to-faint ratio with increasing redshift. Many studies of colour-magnitude relations and luminosity functions in clusters at various redshifts have also measured this value (Barkhouse et al., 2007; Gilbank et al., 2007; Hansen et al., 2009; Stott et al., 2007). A composite set was compared in Gilbank & Balogh (2008), and found a consistent picture of a decreasing DGR with increasing redshift. Later, Lu et al. (2009) studied cluster red-sequence luminosity functions in the CFHTLS, using robust red-sequence selection methods, and found a much more recent faint-end build-up of the RS with little DGR evolution beyond $z > 0.2$.

Following De Lucia et al. (2007), we define the 'dwarf' or faint bin as those red-sequence galaxies with $-20 < M_V \leq -18.2$, and the 'giant' or luminous bin as those red-sequence galaxies with $M_V \leq -20$ (rest frame magnitudes). As mentioned in Section 5.2.1, the difficult task is to emulate a red-sequence selection technique that matches the observational data.

Figure 5.6 shows two DGR comparisons: the compilation of Gilbank & Balogh (2008), and the recent red-sequence study of Lu et al. (2009). For comparison with Gilbank & Balogh (2008), following their procedure, we passively evolve the magnitude limits according to a Bruzual & Charlot (2003) $z_f \sim 3$, solar metallicity model with a Chabrier IMF. The red-sequence is selected using the standard method, where the fit is extrapolated to lower magnitudes for DGR calculations. For comparison with Lu et al. (2009) however, a slightly different approach is needed to emulate their procedure. Their measurements are based on observed $g - r$ vs. r, using data from the CFHTLS and the SDSS. They consider

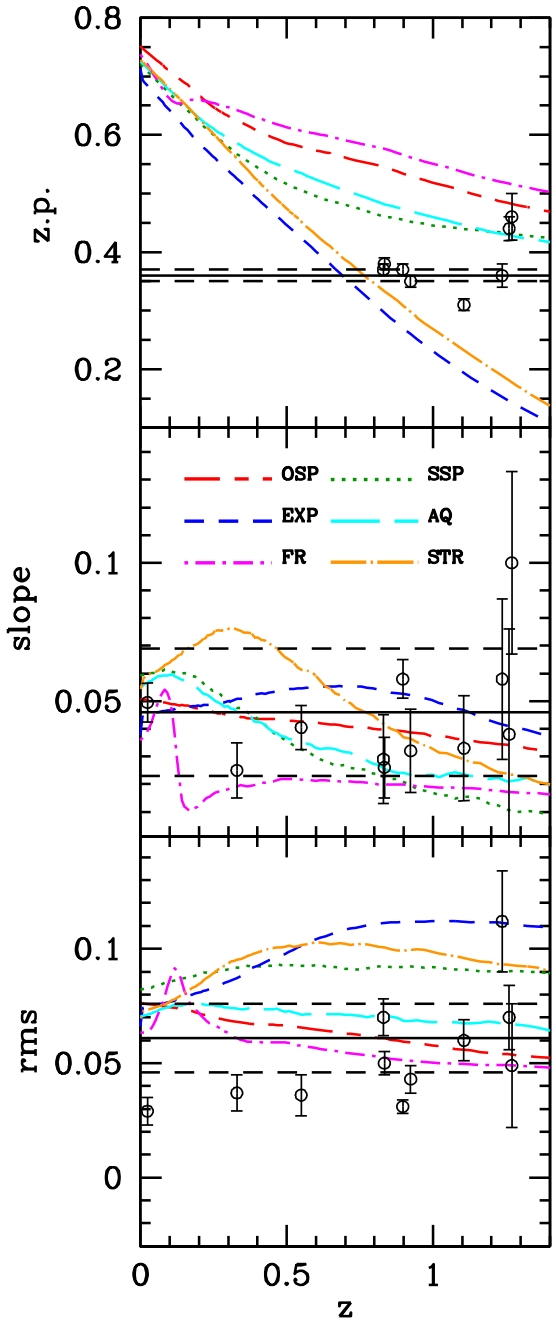

Figure 5.5 CMR evolution comparison with Mei et al. (2009). Predicted and observed zero points, slopes and rms as a function of redshift. The data points represent their data based on E+S0 galaxies, not including the 3 lowest redshift points which are for ellipticals only from the literature. We would expect the rms of these 3 points to increase if S0s were included.

galaxies brighter than $M_* + 2$ for their red-sequence fitting, which is a Schecter function fit to the luminosity function of galaxies in the SDSS from Blanton (2001). Using Fukugita et al. (1995) to transform this value to V band, we find a rest frame limit of -19.24. This, along with the dwarf and giant limits, is allowed to passively evolve according to a Bruzual & Charlot (2003) $z_f \sim 2$ model with Salpeter IMF. Again, the fit OSP slope is used for each timestep, with a free zero-point fit to the red-sequence for each model. Furthermore, only those galaxies redward of the fit slope are considered in the DGR calculation. Observationally this is done to reduce contamination from background galaxies, as well as from blue galaxies which are just joining the red-sequence from the green valley. As a result of the different RS selection, for the same data set, the DGRs from Lu et al. (2009) will differ from those of previous works.

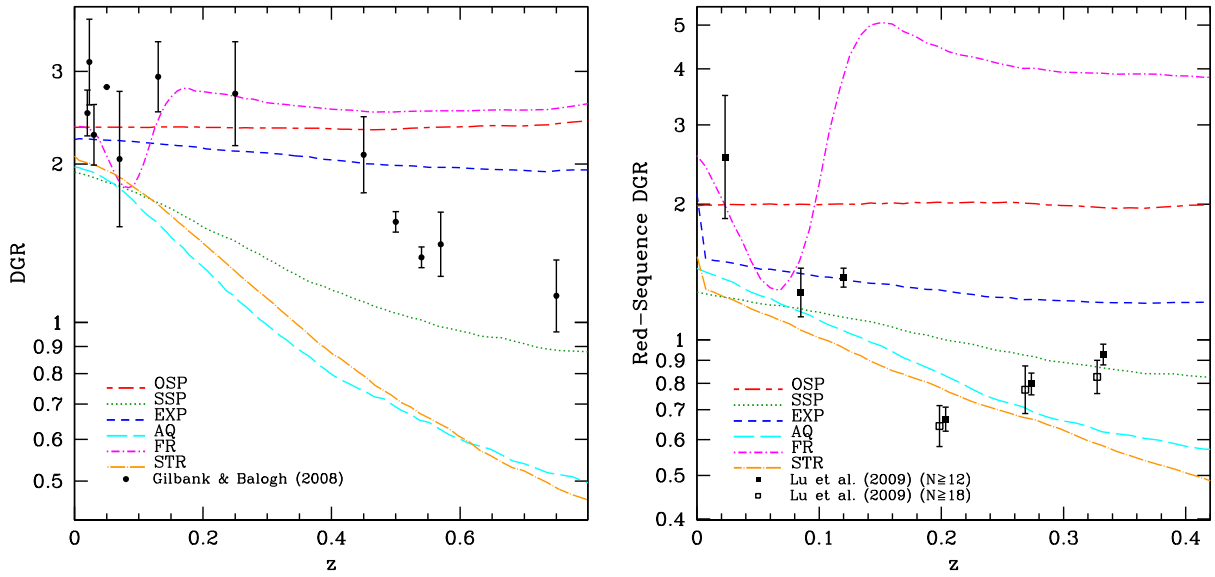

Figure 5.6 Dwarf-to-Giant Ratio evolution comparison to Gilbank & Balogh (2008) (left) and Lu et al. (2009) (right). We attempt to emulate the red-sequence selection of each study precisely, and present them separately here. In the left panel we see a strong difference between the families of models, with the intermediate age models qualitatively agreeing with a DGR evolution. In the right hand panel, the observations show a steep evolution between $0 < z < 0.2$, a much shallower observed evolution between $0.2 < z < 0.4$ (if at all) as well as an overall shallower model DGR evolution. Only the intermediate age models can reproduce the Lu et al. (2009) observations. See Section 5.3 for details.

In comparison with Gilbank & Balogh (2008) in the lefthand frame of Figure 5.6, we see a strong distinction between the 2 families of models. Only those models with intermediate ages show any evolution of the DGR, in qualitative agreement with observation. In comparison with Lu et al. (2009), we see quite different evolution. Not only does the data show weak, if any, evolution of the DGR between $0.2 < z < 0.4$, but the models also show much weaker evolution over this redshift range. This RS selection technique is much less sensitive to those galaxies which have recently joined the red-sequence, which is rapidly occurring at these redshifts. However, a similar result is found in this comparison: only those models of intermediate ages agree with the data here. The data suggest a steep decline in DGR between $0 < z < 0.2$ using their selection technique. No model can simultaneously reproduce this and the shallow evolution at higher redshift. Compare this to the compilation of Gilbank & Balogh (2008) and it is evident that RS selection plays an important role here. In either case, because we have arbitrarily set the DGR ~ 2 at $z \sim 0$ (based on the fact that all synthetic galaxies lie on the RS by design), the zero-point of the modeled evolution is not precise for either comparison. It is worth noting here that the $z \sim 0$ DGRs for all models have significantly decreased in the Lu et al. (2009) RS selection. This effect is due purely to the method used to calculate the DGR, in this case the redward half of the fit RS. The slight curvature seen at the faint end of the modeled RS plays a key role in this effect. However, this effect coupled with the drastically different observed DGR evolution, strongly suggest the DGR is very sensitive to selection technique, and may not be a robust estimator of red-sequence evolution.

As discussed in Sections 3.3.1 and 5, we scaled our VDD such that the resulting synthetic population of galaxies had a DGR ~ 2. An alternative approach could be to normalize our distribution with the $z \sim 0$ red-sequence luminosity functions of Lu et al. (2009). This would eliminate the zero-point inconsistencies and may provide a more accurate DGR evolution.

It is important to note that the DGR evolution, however selected, disfavours the 'old-age' models. Although the EXP model appears to predict a similar DGR evolution to the SSP, the reader is reminded that the EXP model predicts no bimodality of the CMR and so the predicted DGR evolution is not representative of the observed samples.

5.4 Mass-to-Light Ratio Evolution

The redshift evolution of mass-to-light ratios provides insight into the star formation epoch of red-sequence galaxies as well as their assembly histories. It also represents the evolution in the Fundamental Plane in a different projection, and is usually derived from FP fits.

Ultimately, it provides insight into how rapidly the red-sequence is built-up as a function of mass and can be used to discriminate models. We will compare to three data sets: First, the composite set M/L evolution of massive cluster early-types at redshifts $0 < z < 1.3$ of van Dokkum & van der Marel (2007); Second, the FP evolution study of cluster early-types at $z \sim 0.9$ of Jørgensen et al. (2006); Lastly, we will compare to the FP evolution study of field early-types at redshifts $0.2 < z < 1.2$ of Treu et al. (2005).

5.4.1 M/L Evolution of Massive Cluster Early-Types

Figure 5.7 reproduces the data of the van Dokkum & van der Marel (2007) study of massive early-type cluster galaxies. They compile a set of cluster mass-to-light ratios derived from Fundamental Plane analyses. They restrict their analysis to early-type galaxies with masses greater than 10^{11} solar masses, defined identically to the virial relation of Equation 3.14. Here we reproduce this analysis by isolating the red-sequence using the standard method, and finding the average M/L_B at each redshift for each model for all galaxies with $\log(M) > 11$. This is shown in the left panel of Figure 5.7. We can see that out to $z \sim 0.5$, the models appear to generally be indistinguishable. At higher redshifts it appears the SSP and AQ models tend to deviate from a linear dependence on z. van Dokkum & van der Marel (2007) note that their highest redshift value has the strongest effect on their fit, and could suggest non-linearity at high redshift.

However, progenitor bias may be affecting the observed evolution. Some star-forming spirals at high redshift may be the progenitors of the massive ellipticals at low redshifts, and would be ignored in the high redshift samples. Accounting for this bias would show a redshift dependent increase in $|\Delta \log(M/L)|$, having a stronger effect at higher redshifts. van Dokkum & van der Marel (2007) conservatively estimate the bias to be $\Delta_{pbias} \log(M/L_B) \sim 0.05z$, and this offset has been applied to the data in the right panel of Figure 5.7. To remove the effects of progenitor bias in our model fits, we've recalculated them to include all galaxies, not just isolating the RS. By construction, our catalogs contain the progenitors of *today's* RS, thus this procedure should be less susceptible to progenitor bias. We note that the degree of progenitor bias appears to depend on the model, with the largest effect appearing in the SSP and AQ models, and to a lesser extent the STR model. The OSP, FR, and EXP models appear to be unaffected by progenitor bias. The OSP galaxies by construction have been passively evolving since 13Gyr ago, and thus should not experience progenitor bias. The bulk of the secondary bursts in the FR galaxies began more recently than 2-3 Gyr ago, or $z < 0.3$ (the 'wobble' seen in the evolution). At higher redshifts, this model should evolve similarly to the OSP model. The EXP model again does not predict a CMR bimodality, and thus there is little difference

between the entire synthetic cluster and only selecting RS members. The uncertainty in the progenitor bias coupled with the near degeneracy of the intermediate-age models does not allow us to make any further model discrimination.

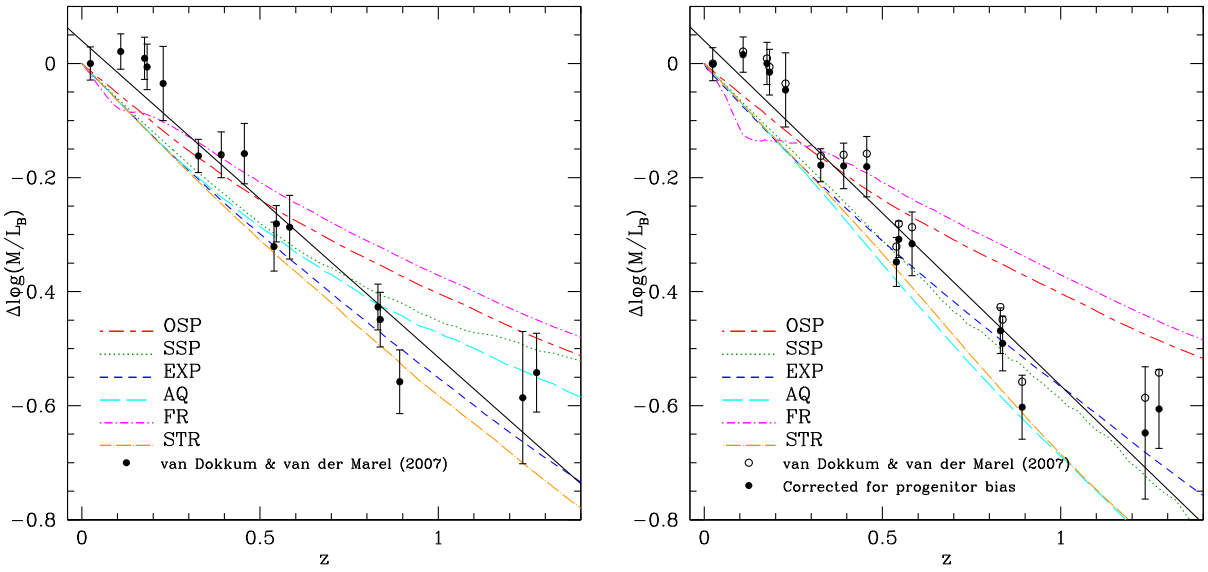

Figure 5.7 $\Delta \log(M/L_B)$ evolution comparison to van Dokkum & van der Marel (2007). (left panel) We emulate their study of massive early-types by isolating red-sequence members with masses greater than 10^{11} solar masses at increasing redshifts, and finding their average deviation of mass-to-light ratio from the $z \sim 0$ value. (Right panel) We have applied their correction to the progenitor bias to their data, and recalculated our modeled evolution by including all progenitors of today's red-sequence with masses greater than 10^{11} solar masses. We note that only the SSP and AQ models show a strong change in their M/L evolution between the two cases (and to a lesser extent the STR model), in qualitative agreement with the approximate progenitor bias correction applied by van Dokkum & van der Marel (2007).

5.4.2 Mass Dependence on M/L evolution of Cluster Early-Types

Recent studies of the evolution of the FP have suggested a systematic increase of the slope of the FP as a function of redshift. We wish to test these results by comparing our

models with Jørgensen et al. (2006), who studied cluster early-type galaxies at $z \sim 0.86$. Although these clusters are included in the ensemble of van Dokkum & van der Marel (2007), it is interesting to compare mass-to-light ratio dependence on mass at a given redshift. Our comparison is illustrated in Figure 5.8. Again, we attempt to model their selection limits, both in magnitude and in mass. They also restrict their analysis to emission free galaxies, which limits their sample to the high redshift red-sequence. We first select our red-sequence members using the standard method. We then set the magnitude limit to match that of Jørgensen et al. (2006) ($M_B < -18.6$ at $z \sim 0.024$ and $M_B < -20.5$ at $z \sim 0.86$). Furthermore, we apply their limit of galaxies with mass greater than $10^{10.3}$ solar masses, defined identically to the virial relation of Equation 3.14. A linear fit is applied to the modeled $\log(M/L_B)$ as a function of $\log(M)$, for both redshifts and all models, and plotted in the top right panel of Figure 5.8. At low redshift, we find good agreement with our comparison in Section 4.3 to the Coma cluster. At high redshift, only the SSP model appears to mimic the data, because it is the only model to demonstrate a steep mass dependence of the mass-to-light ratio evolution with redshift. Note that the SSP model predicts a significant scatter in the M/L vs. M relation. The large scatter, coupled with the diagonal magnitude limit (discussed in Section 5.1.1), is likely biasing the fit towards a steeper relation. It is thus our hypothesis that the strength of the observed evolution of the mass to light ratio dependence on mass is at least partly due to a selection effect, and we will next attempt to quantify this bias.

To estimate the effect of the magnitude limit on the fit, we have performed the same analysis in the bottom right panel of Figure 5.8 by removing the magnitude limit. Here we note that the SSP model no longer reproduces the high redshift observations. The left (SSP) and middle (AQ) panels of the top (magnitude limited) and bottom (no magnitude limit) rows show the selected populations and how they are biased. It is immediately evident that the diagonal magnitude limit strongly biases the fit, with the SSP and AQ slopes increasing by a factor of 2 with the selection effect applied. It is clear that the observed trends can be reproduced by our SSP model, but only if the selection effects are carefully modeled.

Another test is to select galaxies by mass, at a mass well above the magnitude limit. If one were to isolate only the massive galaxies ($\log(M) > 11$) in the high redshift cluster sample, qualitatively we can conclude a shallower slope would result in the observed M/L vs M relation, closer if not equal to the $z \sim 0$ slope. If true, this would support our hypothesis that the observed evolution of the mass to light ratio dependence on mass is at least partly a selection effect.

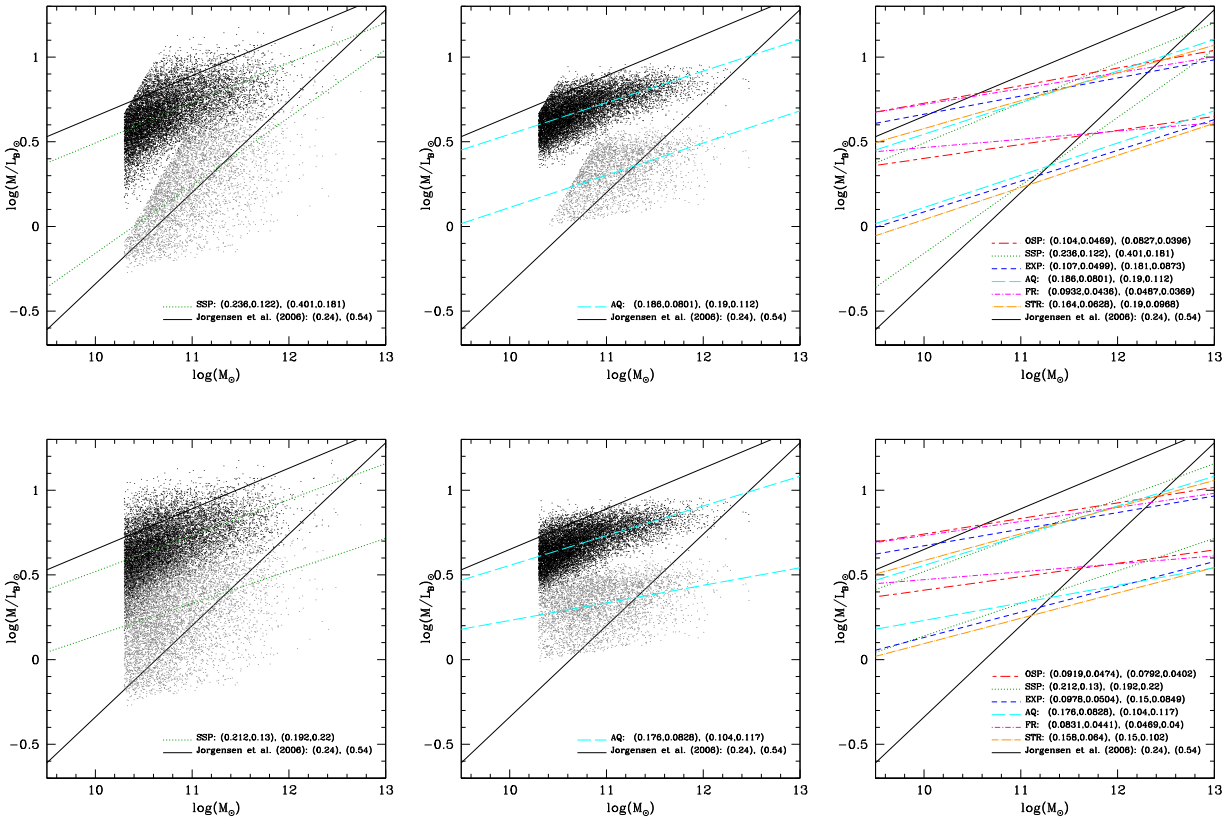

Figure 5.8 $\log(M/L_B)$ vs. Mass evolution comparison with Jørgensen et al. (2006). Here we overplot two sets of fits in each panel, the uppermost set is at $z \sim 0.024$, the lowermost set is at $z \sim 0.86$. These are fit to red-sequence members selected using the standard method. The legend indicates the slope and rms for the two sets, for each model. The top row emulates both the B band magnitude cut as well as their $M > 10^{10.3}$ exclusion criteria. The bottom row applies only the mass limit, without the magnitude cut. The left and middle panels show the SSP and AQ selected populations with and without the magnitude limits. The right panels show the fits for all models. We note that the only model to reproduce the observed evolution of M/L is the SSP model. However, due to the large scatter and diagonal magnitude limit, this is a selection effect (see Section 5.4.2). This can be seen when compared to the unbiased fit. In either case, no other model shows any change in slope between these redshifts.

5.4.3 Mass Dependence on M/L evolution of Field Spheroidals

Similar studies of the assembly history of spheroidals also find a strong mass dependence in the evolution of mass-to-light ratio with redshift, with less massive galaxies experiencing a much more rapid evolution than their high mass counterparts (Treu et al., 2005). Their study focuses on field spheroidals, so a comparison here can also test for environmental dependence or difference.

Figure 5.9 illustrates the mass dependence of the rate of change of mass-to-light ratio with redshift. The solid black line is the best fit from the study of Treu et al. (2005), and we have overlaid our model predictions. We have chosen not to use only red-sequence members here but to include all catalog members, as their sample is morphologically selected, not colour selected, with some members having blue colours and very low mass-to-light ratios. We have also focused our measurements between the redshifts of $0.4 < z < 0.9$, where the majority of their sample resides. To emulate Treu et al. (2005), we have reproduced their magnitude selection limits and applied them to our models. Figure 5.9 shows $d\log(M/L_B)/dz$ as a function of mass, with (left) and without (right) magnitude selection limits. With the magnitude limit, only the SSP, and to a lesser extent the STR model, predicts a strong mass dependence. Without the magnitude limit, there is far less mass dependence at lower masses. To illustrate the origin of this effect, the SSP modeled $\log(M/L_B)$ vs. $\log(M)$ relation is presented for three redshifts, spanning the observed range in Figure 5.10. The top row reproduces the magnitude limits, binning the galaxies by mass ignoring the grey (faint) galaxies. As a comparison, we have performed the same procedure but eliminating the magnitude limits to attempt to quantify the effect they have on the results. This is shown in the bottom row of Figure 5.10. With the magnitude limit, the low mass bins evolve much more rapidly than the high mass bins. Without the magnitude limit, all bins appear to evolve similarly. The large scatter of the SSP model may be contributing to this effect as well, by drawing the low mass bins towards lower M/Ls. However, Treu et al. (2005) claim to model the magnitude limit, yet their results can only be reproduced with our models when introducing their selection bias. So what is going on here? Perhaps early-types in the field evolve later than those in clusters. Note that all models tend to converge to a constant value at high mass, which could suggest that prior to the redshift range of their sample, the most massive galaxies had already migrated to the red-sequence and are evolving passively. This may suggest that massive cluster early-types have already migrated to the RS by $z \sim 0.9$, earlier than their field counterparts. This is supported by Thomas et al. (2005), who find that early-types in low density environments form $\sim$ 2Gyr later than those in high density environments at a given mass. di Serego Alighieri et al. (2006); van Dokkum & van der Marel (2007) both find massive field early-

types to be only slightly younger than their cluster counterparts (5% and 4%, respectively). Thus, it is possible that M/Ls of cluster early-types evolve differently than those in the field. Another possibility is that spheroidals may not be a complete representation of the progenitors of today's red-sequence, i.e. this morphologically selected sample could contain a progentior bias (see Section 5.1.1). It is unclear whether this bias is mass-dependent, however had Treu et al. (2005) included bluer late-types (predominantly at low masses) then the observed evolution would be even stronger. Since they already (without correcting for progenitor bias) find a stronger effect than we predict, this seems unlikely to be the explanation. A final possible explanation is that our models do not accurately reproduce the evolution of M/Ls at high redshift, or that some of the intrinsic assumptions we've made in Section 5 were incorrect or more significant than assumed. It is unclear what the true explanation of the discrepancy is. In the broadest of terms however, it is clear that our 'old age' models of OSP, FR and EXP clearly do not predict the observed trends.

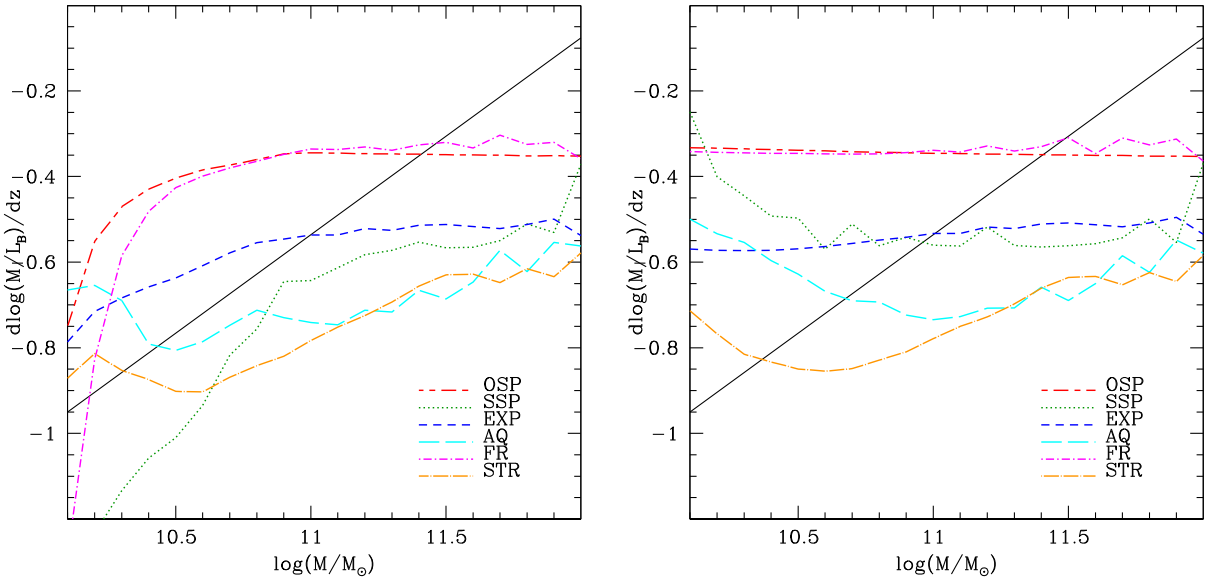

Figure 5.9 $\log(M/L_B)$ evolution comparison with Treu et al. (2005). The solid black line shows the observed best fit trend. Left panel shows the rate of change of mass-to-light ratio over the redshift range of the Treu et al. (2005) sample, as a function of mass, with the emulated magnitude limit. The right panel shows the same procedure, without the magnitude limit. Note how drastically different the SSP model is due to the selection effect.

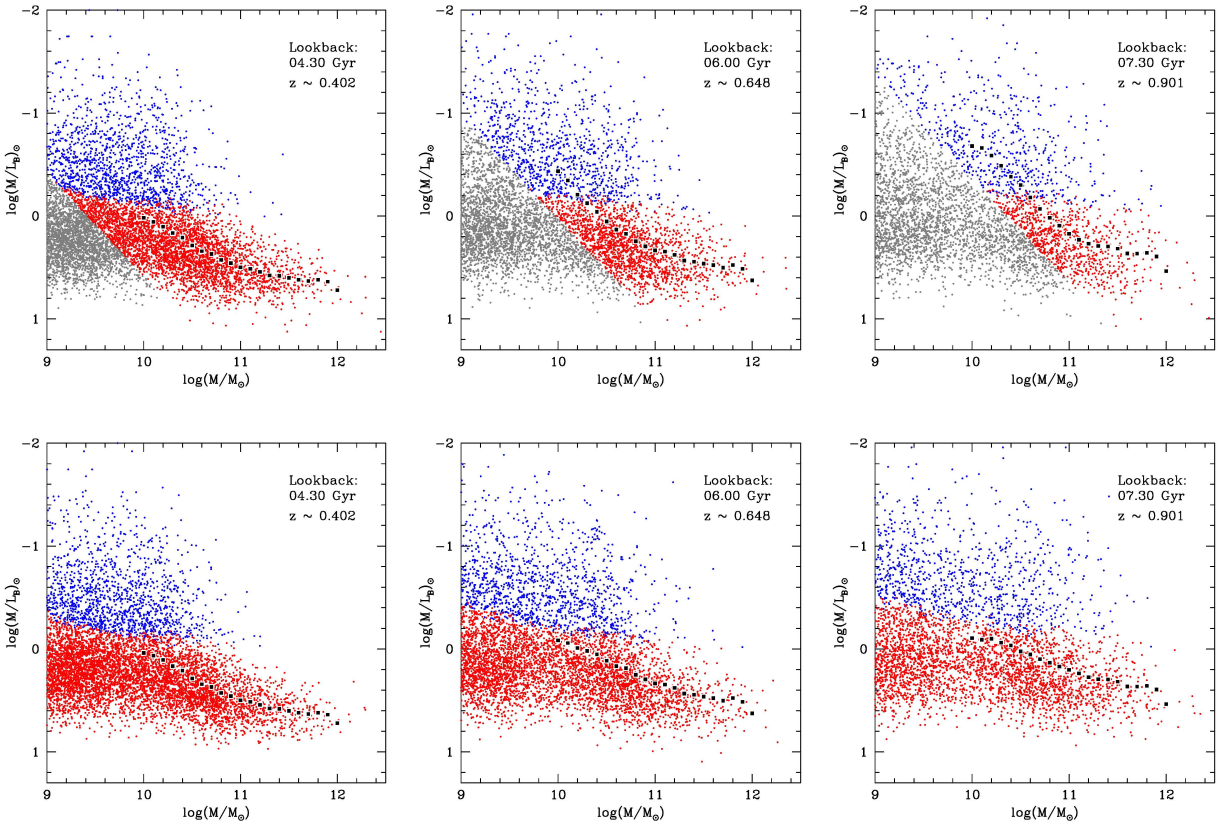

Figure 5.10 SSP $\log(M/L_B)$ evolution comparison with Treu et al. (2005), with and without observed magnitude limit. Top row shows the SSP modeled evolution of $\log(M/L_B)$ as a function of mass, spanning the observed redshift range, applying similar magnitude cuts to our models as experienced in their work. The second row shows the same evolution but without a magnitude limit. Note mass bins here represent all galaxies at a given mass not just red-sequence members. The observed trend can only be reproduced by implementing the selection effect.

With regard to the discussion of Section 4.5.2 on the choice of IMF, we consider the effect on the modeled mass-to-light ratios at high redshift with respect to the observed selection effects. We remind the reader of our choice to use a Kroupa IMF. A Salpeter IMF would raise the stellar M/Ls by a factor of ~ 1.6. This would exacerbate the effect of selection on our comparisons with Treu et al. (2005); Jørgensen et al. (2006), because higher predicted M/Ls gives fainter predicted magnitudes by Equation 3.15, further limiting the selection of synthetic galaxies. A Chabrier IMF would lower the stellar M/Ls slightly, yet likely not significantly enough to offset the magnitude limit effects on the results.

5.5 Summary

We have taken our synthetic clusters fit to the $z \sim 0$ RS, and compared their predicted CMR, DGR, and M/L evolution as lookback time is increased. Selection effects present in the observed data are reproduced and used in the comparisons. It is clear that the OSP, EXP and FR models do not predict the consensus picture of the build-up of the red-sequence, in that there is no apparent colour bimodality as observed by, for example: Bell et al. (2004); De Lucia et al. (2007); Lu et al. (2009). They do not reproduce observed DGR, CMR, or M/L evolution with redshift. The SSP, AQ and STR models are difficult to distinguish. They can reproduce the observed DGR evolution, and show a distinct blue to red transition in the CMR. The SSP model seems favoured in the M/L comparisons when selection effects are emulated. However, this reproduction is largely due to the large scatter in age allowing for lower *average* M/Ls. As a result, an applied diagonal magnitude limit allows a stronger evolution of slope in the M/L vs. M relation than if the selection effect were not present.

Chapter 6

Discussion

6.1 Summary of Model Fits

Here we consider each model separately, and summarize the comparison with observables. The OSP case is already ruled out by the Balmer linestrengths, but we note that it is also a poor fit to the colours, to the FP dynamical M/L, DGR evolution, M/L evolution and does not predict CMR bimodality at high redshift.

FR: The 2% frosting model consists mostly of old stars. It overpredicts the FP-based r-band mass-to-light ratios, and those from SAURON by significant factors (1.7 - 1.9). It does not reproduce observed DGR, evolution, M/L evolution or red-sequence build-up. We reject this model.

EXP: This model also consists mostly of old stars, with the young ages arising from the exponential tail of young stars. It does not reproduce observed DGR, M/L evolution or red-sequence build-up. Like the FR model, the stellar M/L also overpredicts the FP-based dynamical r-band mass-to-light ratios, and those from SAURON by factors 1.45 & 1.65, respectively. Given that we expect there to be some dark matter present in RSGs, we rank this model as "disfavoured".

AQ: The AQ model consists of old through intermediate age stars. In terms of mass-to-light ratio, it marginally overpredicts the FP and dynamical mass-to-light ratios, by factors 1.09 and 1.25. It reproduces the observed DGR evolution and M/L evolution, as well as red-sequence build-up. Given the uncertainties, we rank this model as

"acceptable", although we note that the implication of this model is that there is little DM at low velocity dispersions.

STR At low redshift, the behaviour of this model is similar to the AQ model in most respects. The build-up of the red-sequence happens much more gradually in this model, perhaps as a compromise between the AQ and EXP evolution. It does not reproduce observed CMR evolution, but reasonably reproduces the observed DGR and M/L evolution. We rank this model as "fair".

SSP: This model is the best fit to the linestrengths. Its predicted stellar mass-to-light ratios are always comfortably below the FP-based by factors ~ 0.8 and appear to be similar to the dynamical mass-to-light ratios measured by the SAURON team. It reproduces the observed DGR evolution and M/L evolution, as well as red-sequence build-up. We rank this model as "good".

In summary, the models that fit best to the faint end of the FP, the SAURON mass-to-light ratios, the CMR, DGR, and M/L evolutions are the SSP and AQ models. The models which are "mostly-old" (EXP, FR, OSP) fail to fit the faint end of the FP or the low-σ end of the SAURON M/L ratios by factors of $\sim 1.45 - 1.7$, and do not predict a bimodality in the CMR.

6.2 Comparison of the Predicted and Observed Scatter

For all of the models, with the exception of SSP, the predicted scatter from stellar population effects is well within the scatters observed in the colour-σ, M/L-σ, and FP relations. The SSP model, however, overpredicts the scatter in the M/L and, to a lesser extent, in the FP. This is a direct result of assuming that age is strongly anti-correlated with metallicity at a given velocity dispersion (Section 3.2.1). Recall that the scatter in stellar population parameters is constrained by the scatter in linestrengths. When age and metallicity are anti-correlated as we have assumed, their effects on the predicted linestrength tend to partially cancel. Consequently, the observed scatter in a given linestrength index can be fit with a larger scatter in age and a larger anti-correlated scatter in metallicity than would be the case if these two parameters were assumed uncorrelated. The same "conspiracy" keeps the scatter in colours low. Mass-to-light ratios are more sensitive to age, however, and so as a result, the scatter in M_*/L is larger than it would be if we had assumed that age

and metallicity were uncorrelated when fitting the linestrength scatters. As a result, this does not invalidate the SSP model itself, since it may be possible to fit the line strengths adequately with a weaker age–metallicity anti-correlation[1]. For the other CSFH models, the stellar M/L ratios are largely dominated by older stars and so have considerably less scatter.

6.3 Timescales of Star Formation Histories of Red-Sequence Galaxies

The results here argue that star formation histories of RSGs were either a short SSP-like burst or of somewhat more extended duration as in the AQ model. It is difficult to distinguish between these two cases based on this low-redshift data alone.

One method, although it is somewhat uncertain, is via α-enhancement ratios. Thomas et al. (2005) have argued that, in order to obtain high α-enhancement ratios, the duration of star formation must be less than ~ 1 Gyr. Specifically, they propose a relation $[\alpha/\mathrm{Fe}] = 1/5 - 1/6 \log(\Delta \mathrm{t})$, where Δt is the full-width-at-half-maximum of a Gaussian star formation history. For RSGs of all masses, $[\alpha/\mathrm{Fe}] > 0.2$ (Fig. 3.2 and 3.3) so this implies $\Delta t < 1$ Gyr. Thus based on α-enhancement ratios and the Thomas et al. (2005) models, the SSP would be preferred over the AQ model, for which the duration of star formation can extend over a range of up to ~ 10 Gyr at $\sigma \sim 70$ km s^{-1}. However, it must be emphasized that the translation between $[\alpha/\mathrm{Fe}]$ and star-formation timescale depends on many assumptions about the chemical enrichment histories of early-type galaxies, that remain uncertain at present.

Of course, more complex star formation histories than the ones described here are possible. For example, a plausible model is one in which the bulge component formed in a short SSP-like burst, whereas the disk component was quenched. Clearly the results from this model would lie somewhere between the SSP and AQ cases.

6.4 Implications for the Tilt of the FP

We have shown that the best-fitting model is the SSP, and that, as a result of the scaling of SSP age with velocity dispersion, there is a strong trend of stellar mass-to-light ratio

[1]See Smith et al. (2009a) for an alternative approach to constraining the anti-correlation between age and metallicity.

with velocity dispersion. Consequently, we find that 75%-100% of the r/I-band FP tilt is due to stellar population variations as a function of σ.

A strong SSP-age-driven scaling has generally not been assumed in previous analyses of the FP, leading to the conclusion that the "extra" tilt, e.g. due to DM variations, is much stronger than we find here. For example, Trujillo et al. (2004), assumed an exponential star formation history model, and concluded that only 1/4 the tilt was due to stellar populations. In fact, we would have come to a similar value (30%), had we adopted the EXP model (see Table 4.2). The EXP model is, however, inconsistent with the observed dynamical mass-to-light ratios, as we have shown (Section 4.4).

Padmanabhan et al. (2004) based their scaling analyses on the star formation models of Kauffmann et al. (2003), which are combinations of the EXP and FR models, and found a strong scaling of dynamical mass with stellar mass. A similar conclusion was reached by Gallazzi et al. (2006), who found $M_{\rm dyn}/M_* \propto M_*^{0.28}$, and Hyde & Bernardi (2009b), who found $M_{\rm dyn}/M_* \propto M_{\rm dyn}^{0.17}$, both based on models similar to those of Kauffmann et al. (2003). As a result the assumed star formation history, these studies will overestimate the stellar mass at low masses and hence will overestimate the strength of the DM scaling. For the SSP model, there is essentially no FP tilt due to DM. For the AQ model, the scaling is weak: $M_{\rm dyn}/M_* \propto M_*^{0.06}$.

These results have important consequences for estimating the contributions of mergers and dissipation in forming the FP. For example, dry mergers predict a scaling $M_{\rm dyn}/M_* \propto M_*^{0.12-0.25}$ (Boylan-Kolchin et al., 2006). Robertson et al. (2006) studied dissipational mergers and argued that the tilt of the FP is due to a varying amount of dissipation in mergers along the sequence as a function of mass. If this interpretation is correct, a consequence of our study is that there is little, if any, variation in dissipation as a function of mass.

One might assume that the tilt of the FP in the near-infrared would be less sensitive to the effects of stellar populations, and hence that the K-band FP tilt should reflect primarily the effects of dark matter and non-homology. However, this is approximately valid only in mostly-old SFH models, which cannot simultaneously match line indices and the absolute mass-to-light ratio. For SSP or AQ models, the K-band tilt can be strongly affected by stellar population variations.

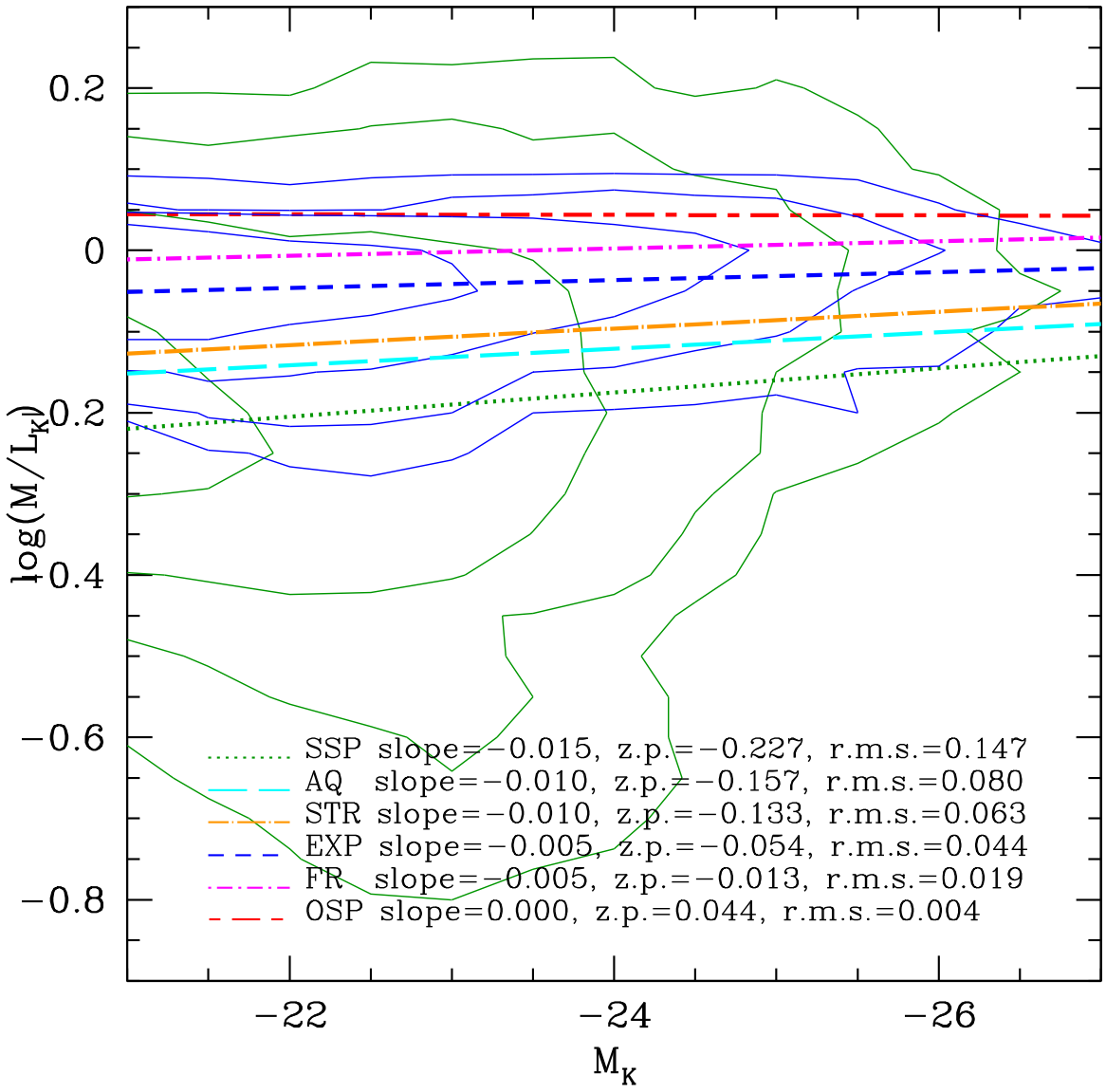

Figure 6.1 M/L_K vs M_K. Best fit lines are calculated for those galaxies below $M_K < -21$, where the data are complete is $\log(\sigma)$. We have overlaid the contours for the SSP and EXP case, to illustrate that the scatter in $\log(\sigma)$ is diagonal, and also to show the very different scatters in $\log(M/L_K)$ between models. The quoted zero-points (z.p.) are measured at $M_K = -24$ (L_*). Line styles and colours as in Fig. 3.1. Green and blue contours are for the SSP and EXP populations, and levels are as in Fig. 3.2. Notice the larger scatter in the SSP case, which decreases the mean mass-to-light ratio.

6.5 Implications for Stellar Masses and the Stellar Mass Density of the Universe in Red Galaxies

We have found that models that are "mostly-old" are ruled out: for small mass systems, their stellar M/L ratios exceed the total dynamical M/L ratios by factors of $\sim 1.45 - 1.7$. This class of models, which includes exponential star formation histories and "frosting" scenarios, have often been used to model the star formation histories of galaxies (Cole et al., 2001; Kauffmann et al., 2003; Bell et al., 2003; Gallazzi et al., 2006). While this may be a reasonable model for late-type or blue galaxies, we have found that it is not a good fit for RSGs. Consequently, the stellar masses of red galaxies have been overestimated by this assumption.

If we assume a different star formation history model, we will arrive at different conclusions, even at bright magnitudes. This is because the dependence of M_*/L_K on age is quite strong for e.g. the SSP model, and hence the scatter in M_*/L_K is also quite large. Thus many galaxies which are bright in K are actually galaxies with relatively small stellar mass that are quite young, boosting their K-band luminosity and lowering their mass-to-light ratio. Figure 6.1 shows the K-band mass-to-light ratio for the different star formation models. The ratios of the mean K-band mass-to-light ratios at $M_K = -24$ (the characteristic K-band luminosity) are 0.73:0.82:1 for SSP:AQ:EXP. Thus for the SSP case, the luminosity density in the early-type galaxies or RSGs as calculated from the K-band should be reduced by a factor of ~ 0.73. This would reduce the stellar mass density calculated by Bell et al. (2003) from 3.2 in units of $10^{-8} h M_\odot$ Mpc^{-3} to 2.3 in the same units, and would reduce the fraction of stellar mass in early-types (assuming that late-types are unaffected) from 60% to 50%. Repeating this calculation in the g-band, for example, the reduction in stellar mass in RSGs is similar to that found for morphologically-selected early-types in the K-band: a factor ~ 0.7. Thus the total fraction of all stellar mass which resides on the red-sequence, as derived by Bell et al. (2003), would be reduced from 70% to 60%.

6.6 Implications For The Build-Up of The Red-Sequence

Our results from comparisons to both low and high redshift data suggest a strong favourability to the SSP and AQ models, and to a lesser extent, the STR model. Our high redshift modeling probes the build-up of the red-sequence by increasing lookback time from the present day red-sequence, and observing its evolution. These three models generally tell a similar story: as galaxies are born they appear blue, and after their star formation is

shut off they migrate to the red-sequence. The AQ model predicts an extended existence in the blue-cloud before migration, whereas the SSP model migrates to the red-sequence immediately after formation. The bright end appears to build-up first, and the faint end build-up completing very recently. This agrees well with conclusions drawn by De Lucia et al. (2007); Lu et al. (2009), which suggest a large fraction of the faint end of the red-sequence was populated recently. Our emulation of the Treu et al. (2005) study showed little mass dependence between the redshifts $0.4 < z < 0.9$, assuming no selection effect. If we were to focus this analysis to more recent times, $0 < z < 0.4$, we can see a very rapid build up at low mass, or faint magnitudes. This is shown in the left panel of Figure 6.2. Note here we are considering all progenitors of today's red-sequence, without a magnitude limit. Compare this with the right panel (identical to bottom right panel of Figure 5.9) which represents the unbiased measurements between $0.4 < z < 0.9$ and we see quite different evolution over the quoted redshift ranges. This further agrees with De Lucia et al. (2007); Lu et al. (2009) in their hypotheses of recent faint end build-up of the red-sequence, as well as our conclusion that only the intermediate age models produce evolutionary build-up.

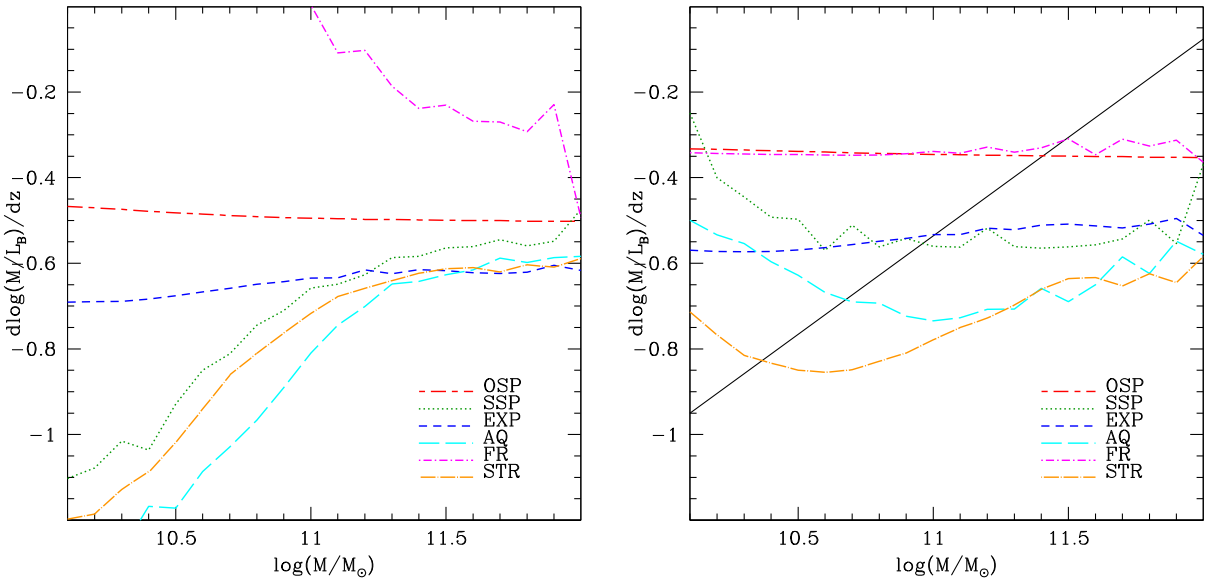

Figure 6.2 Left panel shows low redshift ($0 < z < 0.4$) mass-to-light ratio evolution of the progenitors of today's red-sequence as a function of mass. Right panel shows the same but for higher redshifts ($0.4 < z < 0.9$) as seen in Figure 5.9 in comparison to Treu et al. (2005). At low redshifts we see a much steeper evolution in the intermediate age models, suggesting a recent build up of the faint end of the red-sequence in agreement with the studies of De Lucia et al. (2007); Lu et al. (2009).

Chapter 7

Conclusions

We have constructed six parametric star formation models, each representing a distinct star formation history. The modeled Lick indices were fit to observed linestrength data in the Shapley supercluster, and sets of best-fit model parameters were constructed for each velocity dispersion bin for each model. Synthetic cluster populations were then constructed based on the statistical distributions of each stellar population parameter, and mass-to-light ratios were derived from the stellar populations. The predicted evolutions of dwarf-to-giant ratios, colour-magnitude relations and mass-to-light ratios were calculated.

Our main results are as follows:

1. From the fits to linestrength indices, we find that in all models there exists a "downsizing" trend in luminosity weighted-age age for galaxies with $\sigma > 70 \mathrm{km\,s^{-1}}$. Lower-$\sigma$ galaxies also tend to be less metal rich and α-enhanced. We find that, based on the fits to the Lick indices alone, the OSP model is strongly rejected. This agrees with previous studies (Nelan et al., 2005). The EXP and FR models are poorer fits to the linestrength data than the SSP model, but cannot be rejected from this test alone.

2. The linestrength data suggest that the "downsizing" effect stops at $\sigma \sim 70$ $\mathrm{km\,s^{-1}}$ below which luminosity-weighted stellar ages either stop decreasing or begin to increase. This is not a selection effect, which would tend to bias the data in the opposite sense.

3. The derived stellar mass-to-light ratios from the models were compared to dynamical mass-to-light ratios from the FP and from Cappellari et al. (2006). The "mostly-old" class of star formation models (OSP, EXP and FR) have Kroupa-IMF *stellar*

mass-to-light ratios that are larger than the observed dynamical mass-to-light ratios for low-σ galaxies, by factors 1.45–1.7. For these models, the addition of dark matter would make the agreement worse, thus these "mostly-old" models are ruled out. We conclude that the ~ 6 Gyr luminosity-weighted ages of low-mass RSGs do indeed reflect the "intermediate" ages of the bulk of the stellar population, as parameterized by the SSP or AQ models.

4. The "intermediate-age" models show strong evolution from the blue cloud to the red-sequence, whereas the "mostly-old" models have a well-populated red-sequence at all lookback times. Consequently, the favoured "intermediate-age" models suggest a recent build-up of the faint end of the red-sequence, consistent with observation.

5. We have shown that, for the "intermediate-age" scenarios, the scaling of stellar mass-to-light ratio with mass is strong, both in the optical bands and in the K-band. Consequently, stellar populations explain most of the FP tilt in the optical bands, and, for the SSP case, at least 50% of the tilt in the K-band. This leaves much less room for tilt due to variations in the dark-to-stellar mass along the red-sequence.

6. For the SSP model, the stellar masses are considerably reduced, particularly at low velocity dispersions, compared to the star formation histories assumed in previous studies. As a consequence, the stellar mass density in red galaxies may be as much as 30% lower than previously assumed.

In terms of the *average* star formation histories of red-sequence galaxies, based on the reproducibility of observables at various redshifts, we conclude that the star formation was rapidly quenched either after a long period of star formation or immediately following a single immense star burst. A hybrid of the SSP and AQ, in which, for example, the bulge of the system formed in a short intense burst, while the disk was quenched at a later time, would likely fit all of the data well. It is unlikely that the average star formation rate trailed off gradually, or that an ancient population was 'frosted' by recent star formation.

In Section 1.1 we discussed a few processes that could shut off star formation. These findings may also suggest the average preferential mechanism of quenching star formation in RSGs. Because our models prefer when quenching happens rapidly (SSP, AQ), this suggests the cold gas is stripped from the galaxies rapidly. We can conclude that ram pressure stripping through a mechanism like cluster infall is preferred over an extended 'gas exhaustion'-type scenario (EXP). If star formation had progressed for some time before an exponential decline in star formation rate began, we have shown the STR to be a reasonable model and thus the strangulation mechanism is also possible. This mechanism

is less preferred however, because of the blurred bimodality of the CMR and its evolution does not agree as well with observations.

Generally speaking, these models we have introduced and explored are somewhat naive. Realistically, all cluster galaxies will not experience an identical star formation history. We have suggested here some preferential mechanisms and possible hybrid models. Perhaps exploring more complex star formation histories which exhibit a deliberate mix of our models could be more realistic.

However, the problem with this type of analysis is the degeneracy involved. By our method, each observed galaxy has a single associated spectrum. This spectrum represents the average properties of the entire stellar population of the galaxy, whose fit ages will always be weighted towards the most recent starburst and blurs the line between star formation epochs. There are a few options to help disentangle this in the future:

1. Integral Field Units (IFU). If a representative sample of 'pure' ellipticals is observed with fibre bundles, in theory we could reproduce our analysis for multiple projected regions. Different regions could be isolated and ages of different components could be disentangled. This could provide a higher resolution and insight into the true star formation history on a galaxy-by-galaxy basis. Similarly, long-slit spectra can allow the resolving of stellar populations within a galaxy. For example, a disk/bulge system could be observed separately, and thus the overall star formation history can become a variable 2 component model. The problem with IFU analysis is the sheer cost of observing time required. This increases with the number of galaxies required to overcome the intrinsic scatters in parameters.

2. High redshift spectra. Quite simply, a sample of high redshift cluster galaxies could be spectroscopically observed and our analysis applied. This would help understand, and perhaps alter our assumptions. The problem with this method is the extensive cost to get acceptable signal-to-noise ratios for this analysis.

The goal of these above methods is simply to help narrow down the evolution of stellar populations and help understand more complex and perhaps realistic star formation histories. For example, recent studies have suggested that galaxy mergers incite a burst of star formation before it is shut off. This is seen in so-called $H\delta$-strong galaxies, with deep Balmer lines indicative of young ages which appear to have been in a recent merger. Our current models would weight the overall age of the galaxy towards that recent burst. Any number of more exotic models could be assumed, such as an EXP with various mixed SSPs. These more complex methods of observation would all help in disentangling these

degeneracies. The main setback that these face is the overwhelming cost and observing time they require. In the future of 30m telescopes these would be far more efficient and far less expensive, although the Thirty-Meter-Telescope (TMT) project itself is not cheap ($1 billion USD to construct). Future observations will surely help narrow down these problems and issues, as well as create better stellar population models in which we can model star formation histories with absorption linestrengths.

Bibliography

Adelman-McCarthy, J. K. e. a. 2008, ApJS, 175, 297 14

Aragon-Salamanca, A., Ellis, R. S., Couch, W. J., & Carter, D. 1993, MNRAS, 262, 764 59

Baldry, I. K., Glazebrook, K., Brinkmann, J., Ivezić, Ž., Lupton, R. H., Nichol, R. C., & Szalay, A. S. 2004, ApJ, 600, 681 4, 62

Balogh, M. L. & Morris, S. L. 2000, MNRAS, 318, 703 4

Barkhouse, W. A., Yee, H. K. C., & López-Cruz, O. 2007, ApJ, 671, 1471 70

Barnes, J. E. & Hernquist, L. 1992, ARA&A, 30, 705 3

Bell, E. F., McIntosh, D. H., Katz, N., & Weinberg, M. D. 2003, ApJS, 149, 289 6, 10, 63, 87

Bell, E. F., Wolf, C., Meisenheimer, K., Rix, H.-W., Borch, A., Dye, S., Kleinheinrich, M., Wisotzki, L., & McIntosh, D. H. 2004, ApJ, 608, 752 62, 81

Bender, R., Burstein, D., & Faber, S. M. 1992, ApJ, 399, 462 10, 47

Bernardi, M., Sheth, R. K., Nichol, R. C., Schneider, D. P., & Brinkmann, J. 2005, AJ, 129, 61 6, 22, 62

Blanton, M. R., Hogg, D. W., Bahcall, N. A., Baldry, I. K., Brinkmann, J., Csabai, I., Eisenstein, D., Fukugita, M., Gunn, J. E., Ivezić, Ž., Lamb, D. Q., Lupton, R. H., Loveday, J., Munn, J. A., Nichol, R. C., Okamura, S., Schlegel, D. J., Shimasaku, K., Strauss, M. A., Vogeley, M. S., & Weinberg, D. H. 2003, ApJ, 594, 186 4

Blanton, M. R. e. a. 2001, AJ, 121, 2358 72

Blumenthal, G. R., Faber, S. M., Primack, J. R., & Rees, M. J. 1984, Nature, 311, 517 2, 3

Bolton, A. S., Treu, T., Koopmans, L. V. E., Gavazzi, R., Moustakas, L. A., Burles, S., Schlegel, D. J., & Wayth, R. 2008, ApJ, 684, 248 38, 55

Bower, R. G., Lucey, J. R., & Ellis, R. S. 1992, MNRAS, 254, 601 10, 59, 62, 68

Boylan-Kolchin, M., Ma, C.-P., & Quataert, E. 2006, MNRAS, 369, 1081 56, 85

Bruzual, G. & Charlot, S. 2003, MNRAS, 344, 1000 5, 68, 70, 72

Butcher, H. & Oemler, A. 1978, ApJ, 219, 18 63

—. 1984, ApJ, 285, 426 63

Caldwell, N., Rose, J. A., & Concannon, K. D. 2003, AJ, 125, 2891 6, 34

Cappellari, M., Bacon, R., Bureau, M., Damen, M. C., Davies, R. L., de Zeeuw, P. T., Emsellem, E., Falcón-Barroso, J., Krajnović, D., Kuntschner, H., McDermid, R. M., Peletier, R. F., Sarzi, M., van den Bosch, R. C. E., & van de Ven, G. 2006, MNRAS, 366, 1126 10, 22, 38, 50, 52, 53, 90

Chabrier, G. 2003, PASP, 115, 763 55

Coelho, P., Bruzual, G., Charlot, S., Weiss, A., Barbuy, B., & Ferguson, J. W. 2007, MNRAS, 382, 498 44, 46

Cole, S., Norberg, P., Baugh, C. M., Frenk, C. S., Bland-Hawthorn, J., Bridges, T., Cannon, R., Colless, M., Collins, C., Couch, W., Cross, N., Dalton, G., De Propris, R., Driver, S. P., Efstathiou, G., Ellis, R. S., Glazebrook, K., Jackson, C., Lahav, O., Lewis, I., Lumsden, S., Maddox, S., Madgwick, D., Peacock, J. A., Peterson, B. A., Sutherland, W., & Taylor, K. 2001, MNRAS, 326, 255 87

Cole, S., Percival, W. J., Peacock, J. A., Norberg, P., Baugh, C. M., Frenk, C. S., Baldry, I., Bland-Hawthorn, J., Bridges, T., Cannon, R., Colless, M., Collins, C., Couch, W., Cross, N. J. G., Dalton, G., Eke, V. R., De Propris, R., Driver, S. P., Efstathiou, G., Ellis, R. S., Glazebrook, K., Jackson, C., Jenkins, A., Lahav, O., Lewis, I., Lumsden, S., Maddox, S., Madgwick, D., Peterson, B. A., Sutherland, W., & Taylor, K. 2005, MNRAS, 362, 505 2

Crampin, J. & Hoyle, F. 1961, MNRAS, 122, 27 5

De Lucia, G., Poggianti, B. M., Aragón-Salamanca, A., Clowe, D., Halliday, C., Jablonka, P., Milvang-Jensen, B., Pelló, R., Poirier, S., Rudnick, G., Saglia, R., Simard, L., & White, S. D. M. 2004, ApJL, 610, L77 70

De Lucia, G., Poggianti, B. M., Aragón-Salamanca, A., White, S. D. M., Zaritsky, D., Clowe, D., Halliday, C., Jablonka, P., von der Linden, A., Milvang-Jensen, B., Pelló, R., Rudnick, G., Saglia, R. P., & Simard, L. 2007, MNRAS, 374, 809 61, 62, 63, 64, 68, 69, 70, 81, 88, 89

Dekel, A. & Silk, J. 1986, ApJ, 303, 39 3

di Serego Alighieri, S., Lanzoni, B., & Jørgensen, I. 2006, ApJL, 652, L145 78

Djorgovski, S. & Davis, M. 1987, ApJ, 313, 59 10

Dressler, A. & Gunn, J. E. 1990, in Astronomical Society of the Pacific Conference Series, Vol. 10, Evolution of the Universe of Galaxies, ed. R. G. Kron, 200–208 59

Dressler, A., Lynden-Bell, D., Burstein, D., Davies, R. L., Faber, S. M., Terlevich, R., & Wegner, G. 1987, ApJ, 313, 42 10, 47

Dressler, A., Smail, I., Poggianti, B. M., Butcher, H., Couch, W. J., Ellis, R. S., & Oemler, A. J. 1999, ApJS, 122, 51 61

Edwards, L. O. V., Hudson, M. J., Balogh, M. L., & Smith, R. J. 2007, MNRAS, 379, 100 3

Ellis, R. S., Smail, I., Dressler, A., Couch, W. J., Oemler, A. J., Butcher, H., & Sharples, R. M. 1997, ApJ, 483, 582 62, 68

Faber, S. M. & Jackson, R. E. 1976, ApJ, 204, 668 10

Fabian, A. C. 1994, ARA&A, 32, 277 3

Fall, S. M. & Efstathiou, G. 1980, MNRAS, 193, 189 2

Ferrarese, L. & Merritt, D. 2000, ApJL, 539, L9 3

Frei, Z. & Gunn, J. E. 1994, AJ, 108, 1476 14

Fukugita, M., Shimasaku, K., & Ichikawa, T. 1995, PASP, 107, 945 72

Gallazzi, A., Charlot, S., Brinchmann, J., & White, S. D. M. 2006, MNRAS, 370, 1106 34, 62, 85, 87

Gerhard, O., Kronawitter, A., Saglia, R. P., & Bender, R. 2001, AJ, 121, 1936 10

Gilbank, D. G. & Balogh, M. L. 2008, MNRAS, 385, L116 36, 37, 70, 72, 73

Gilbank, D. G., Yee, H. K. C., Ellingson, E., Gladders, M. D., Barrientos, L. F., & Blindert, K. 2007, AJ, 134, 282 70

Graves, G. J., Faber, S. M., Schiavon, R. P., & Yan, R. 2007, ApJ, 671, 243 41

Gunn, J. E. & Gott, J. R. I. 1972, ApJ, 176, 1 4

Hansen, S. M., Sheldon, E. S., Wechsler, R. H., & Koester, B. P. 2009, ApJ, 699, 1333 70

Harker, J. J., Schiavon, R. P., Weiner, B. J., & Faber, S. M. 2006, ApJL, 647, L103 6

Heavens, A., Panter, B., Jimenez, R., & Dunlop, J. 2004, Nature, 428, 625 34

Hoekstra, H., Mellier, Y., van Waerbeke, L., Semboloni, E., Fu, L., Hudson, M. J., Parker, L. C., Tereno, I., & Benabed, K. 2006, ApJ, 647, 116 2

Hogg, D. W., Blanton, M. R., Brinchmann, J., Eisenstein, D. J., Schlegel, D. J., Gunn, J. E., McKay, T. A., Rix, H.-W., Bahcall, N. A., Brinkmann, J., & Meiksin, A. 2004, ApJL, 601, L29 62

Hopkins, A. M. & Beacom, J. F. 2006, ApJ, 651, 142 33

Hyde, J. B. & Bernardi, M. 2009a, MNRAS, 394, 1978 17

—. 2009b, MNRAS, 396, 1171 85

Jørgensen, I., Chiboucas, K., Flint, K., Bergmann, M., Barr, J., & Davies, R. 2006, ApJL, 639, L9 74, 76, 77, 81

Jorgensen, I., Franx, M., & Kjaergaard, P. 1996, MNRAS, 280, 167 47

Kauffmann, G., Heckman, T. M., White, S. D. M., Charlot, S., Tremonti, C., Peng, E. W., Seibert, M., Brinkmann, J., Nichol, R. C., SubbaRao, M., & York, D. 2003, MNRAS, 341, 54 6, 63, 85, 87

Kelson, D. D., Illingworth, G. D., Franx, M., & van Dokkum, P. G. 2006, ApJ, 653, 159 41

Kodama, T. & Arimoto, N. 1997, A&A, 320, 41 59, 63

Komatsu, E., Dunkley, J., Nolta, M. R., Bennett, C. L., Gold, B., Hinshaw, G., Jarosik, N., Larson, D., Limon, M., Page, L., Spergel, D. N., Halpern, M., Hill, R. S., Kogut, A., Meyer, S. S., Tucker, G. S., Weiland, J. L., Wollack, E., & Wright, E. L. 2009, ApJS, 180, 330 2

Kormendy, J. 1985, ApJ, 295, 73 17

Kroupa, P. 2001, MNRAS, 322, 231 38, 55

La Barbera, F., Busarello, G., Merluzzi, P., de la Rosa, I. G., Coppola, G., & Haines, C. P. 2008, ApJ, 689, 913 10

Larson, R. B. 1974, MNRAS, 169, 229 3

Larson, R. B., Tinsley, B. M., & Caldwell, C. N. 1980, ApJ, 237, 692 4

López-Cruz, O., Barkhouse, W. A., & Yee, H. K. C. 2004, ApJ, 614, 679 7, 14, 62

Lu, T., Gilbank, D. G., Balogh, M. L., & Bognat, A. 2009, ArXiv e-prints 60, 61, 63, 68, 70, 72, 73, 81, 88, 89

Maraston, C. 1998, MNRAS, 300, 872 4, 5, 18, 38

Maraston, C. 2003, in Extragalactic Globular Cluster Systems, ed. M. Kissler-Patig, 237–+ 5

—. 2005, MNRAS, 362, 799 5, 18, 38, 44, 68

Maraston, C., Strömbäck, G., Thomas, D., Wake, D. A., & Nichol, R. C. 2009, MNRAS, 394, L107 45

Matković, A. & Guzmán, R. 2005, MNRAS, 362, 289 17, 47

McIntosh, D. H., Zabludoff, A. I., Rix, H.-W., & Caldwell, N. 2005, ApJ, 619, 193 7, 62

Mei, S., Holden, B. P., Blakeslee, J. P., Ford, H. C., Franx, M., Homeier, N. L., Illingworth, G. D., Jee, M. J., Overzier, R., Postman, M., Rosati, P., Van der Wel, A., & Bartlett, J. G. 2009, ApJ, 690, 42 62, 69, 70, 71

Nelan, J. E., Smith, R. J., Hudson, M. J., Wegner, G. A., Lucey, J. R., Moore, S. A. W., Quinney, S. J., & Suntzeff, N. B. 2005, ApJ, 632, 137 6, 14, 20, 22, 33, 34, 60, 90

Padmanabhan, N., Seljak, U., Strauss, M. A., Blanton, M. R., Kauffmann, G., Schlegel, D. J., Tremonti, C., Bahcall, N. A., Bernardi, M., Brinkmann, J., Fukugita, M., & Ivezić, Ž. 2004, New Astronomy, 9, 329 85

Pahre, M. A., de Carvalho, R. R., & Djorgovski, S. G. 1998, AJ, 116, 1606 10

Peng, C. Y., Ho, L. C., Impey, C. D., & Rix, H.-W. 2002, AJ, 124, 266 14

Percival, S. M., Salaris, M., Cassisi, S., & Pietrinferni, A. 2009, ApJ, 690, 427 46

Perlmutter, S., Aldering, G., Goldhaber, G., Knop, R. A., Nugent, P., Castro, P. G., Deustua, S., Fabbro, S., Goobar, A., Groom, D. E., Hook, I. M., Kim, A. G., Kim, M. Y., Lee, J. C., Nunes, N. J., Pain, R., Pennypacker, C. R., Quimby, R., Lidman, C., Ellis, R. S., Irwin, M., McMahon, R. G., Ruiz-Lapuente, P., Walton, N., Schaefer, B., Boyle, B. J., Filippenko, A. V., Matheson, T., Fruchter, A. S., Panagia, N., Newberg, H. J. M., Couch, W. J., & The Supernova Cosmology Project. 1999, ApJ, 517, 565 1

Pickles, A. J. 1998, PASP, 110, 863 45

Poggianti, B. M., Smail, I., Dressler, A., Couch, W. J., Barger, A. J., Butcher, H., Ellis, R. S., & Oemler, A. J. 1999, ApJ, 518, 576 4

Poggianti, B. M., von der Linden, A., De Lucia, G., Desai, V., Simard, L., Halliday, C., Aragón-Salamanca, A., Bower, R., Varela, J., Best, P., Clowe, D. I., Dalcanton, J., Jablonka, P., Milvang-Jensen, B., Pello, R., Rudnick, G., Saglia, R., White, S. D. M., & Zaritsky, D. 2006, ApJ, 642, 188 61

Prugniel, P. & Simien, F. 1996, A&A, 309, 749 10

Rakos, K. D. & Schombert, J. M. 1995, ApJ, 439, 47 59

Rawle, T. D., Smith, R. J., Lucey, J. R., & Swinbank, A. M. 2008, MNRAS, 389, 1891 31

Renzini, A. 2006, ARA&A, 44, 141 10, 11

Riess, A. G., Filippenko, A. V., Challis, P., Clocchiatti, A., Diercks, A., Garnavich, P. M., Gilliland, R. L., Hogan, C. J., Jha, S., Kirshner, R. P., Leibundgut, B., Phillips, M. M., Reiss, D., Schmidt, B. P., Schommer, R. A., Smith, R. C., Spyromilio, J., Stubbs, C., Suntzeff, N. B., & Tonry, J. 1998, AJ, 116, 1009 1

Robertson, B., Cox, T. J., Hernquist, L., Franx, M., Hopkins, P. F., Martini, P., & Springel, V. 2006, ApJ, 641, 21 85

Salpeter, E. E. 1955, ApJ, 121, 161 55

Sánchez-Blázquez, P., Gorgas, J., Cardiel, N., & González, J. J. 2006, A&A, 457, 809 35

Sandage, A. & Visvanathan, N. 1978, ApJ, 223, 707 10

Schawinski, K., Khochfar, S., Kaviraj, S., Yi, S. K., Boselli, A., Barlow, T., Conrow, T., Forster, K., Friedman, P. G., Martin, D. C., Morrissey, P., Neff, S., Schiminovich, D., Seibert, M., Small, T., Wyder, T. K., Bianchi, L., Donas, J., Heckman, T., Lee, Y.-W., Madore, B., Milliard, B., Rich, R. M., & Szalay, A. 2006, Nature, 442, 888 3

Schiavon, R. P. 2007, ApJS, 171, 146 34

Schlegel, D. J., Finkbeiner, D. P., & Davis, M. 1998, ApJ, 500, 525 14

Serra, P. & Trager, S. C. 2007, MNRAS, 374, 769 6

Shen, S., Mo, H. J., White, S. D. M., Blanton, M. R., Kauffmann, G., Voges, W., Brinkmann, J., & Csabai, I. 2003, MNRAS, 343, 978 17

Sheth, R. K., Bernardi, M., Schechter, P. L., Burles, S., Eisenstein, D. J., Finkbeiner, D. P., Frieman, J., Lupton, R. H., Schlegel, D. J., Subbarao, M., Shimasaku, K., Bahcall, N. A., Brinkmann, J., & Ivezić, Ž. 2003, ApJ, 594, 225 36, 37, 60

Skrutskie, M. F., Cutri, R. M., Stiening, R., Weinberg, M. D., Schneider, S., Carpenter, J. M., Beichman, C., Capps, R., Chester, T., Elias, J., Huchra, J., Liebert, J., Lonsdale, C., Monet, D. G., Price, S., Seitzer, P., Jarrett, T., Kirkpatrick, J. D., Gizis, J. E., Howard, E., Evans, T., Fowler, J., Fullmer, L., Hurt, R., Light, R., Kopan, E. L., Marsh, K. A., McCallon, H. L., Tam, R., Van Dyk, S., & Wheelock, S. 2006, AJ, 131, 1163 14

Smith, R. J., Hudson, M. J., Lucey, J. R., Nelan, J. E., & Wegner, G. A. 2006, MNRAS, 369, 1419 6, 14

Smith, R. J., Lucey, J. R., & Hudson, M. J. 2007, MNRAS, 381, 1035 13, 31, 34, 35

Smith, R. J., Lucey, J. R., & Hudson, M. J. 2008, in IAU Symposium, Vol. 245, Formation and Evolution of Galaxy Bulges, 411–414 24, 28

—. 2009a, MNRAS, submitted 6, 22, 84

Smith, R. J., Lucey, J. R., Hudson, M. J., Allanson, S. P., Bridges, T. J., Hornschemeier, A. E., Marzke, R. O., & Miller, N. A. 2009b, MNRAS, 392, 1265 6, 14, 34, 35

Sparke, L. S. & Gallagher, III, J. S. 2000, Galaxies in the universe : an introduction, ed. L. S. Sparke & J. S. Gallagher, III 7, 9

Stott, J. P., Smail, I., Edge, A. C., Ebeling, H., Smith, G. P., Kneib, J.-P., & Pimbblet, K. A. 2007, ApJ, 661, 95 70

Tegmark, M., Blanton, M. R., Strauss, M. A., Hoyle, F., Schlegel, D., Scoccimarro, R., Vogeley, M. S., Weinberg, D. H., Zehavi, I., Berlind, A., Budavari, T., Connolly, A., Eisenstein, D. J., Finkbeiner, D., Frieman, J. A., Gunn, J. E., Hamilton, A. J. S., Hui, L., Jain, B., Johnston, D., Kent, S., Lin, H., Nakajima, R., Nichol, R. C., Ostriker, J. P., Pope, A., Scranton, R., Seljak, U., Sheth, R. K., Stebbins, A., Szalay, A. S., Szapudi, I., Verde, L., Xu, Y., Annis, J., Bahcall, N. A., Brinkmann, J., Burles, S., Castander, F. J., Csabai, I., Loveday, J., Doi, M., Fukugita, M., Gott, J. R. I., Hennessy, G., Hogg, D. W., Ivezić, Ž., Knapp, G. R., Lamb, D. Q., Lee, B. C., Lupton, R. H., McKay, T. A., Kunszt, P., Munn, J. A., O'Connell, L., Peoples, J., Pier, J. R., Richmond, M., Rockosi, C., Schneider, D. P., Stoughton, C., Tucker, D. L., Vanden Berk, D. E., Yanny, B., & York, D. G. 2004, ApJ, 606, 702 2

Thomas, D., Maraston, C., & Bender, R. 2002, ApSS, 281, 371 6

—. 2003, MNRAS, 339, 897 5, 18, 44, 60

Thomas, D., Maraston, C., Bender, R., & de Oliveira, C. M. 2005, ApJ, 621, 673 5, 6, 34, 38, 55, 78, 84

Thomas, D., Maraston, C., & Korn, A. 2004, MNRAS, 351, L19 18, 44

Tinsley, B. M. 1968, ApJ, 151, 547 5

Toomre, A. 1977, in Evolution of Galaxies and Stellar Populations, ed. B. M. Tinsley & R. B. Larson, 401–+ 2

Toomre, A. & Toomre, J. 1972, ApJ, 178, 623 3

Trager, S. C., Faber, S. M., & Dressler, A. 2008, MNRAS, 386, 715 33, 35

Trager, S. C., Faber, S. M., Worthey, G., & González, J. J. 2000, AJ, 120, 165 6, 22, 24, 60

Tremaine, S., Gebhardt, K., Bender, R., Bower, G., Dressler, A., Faber, S. M., Filippenko, A. V., Green, R., Grillmair, C., Ho, L. C., Kormendy, J., Lauer, T. R., Magorrian, J., Pinkney, J., & Richstone, D. 2002, ApJ, 574, 740 3

Treu, T., Ellis, R. S., Liao, T. X., van Dokkum, P. G., Tozzi, P., Coil, A., Newman, J., Cooper, M. C., & Davis, M. 2005, ApJ, 633, 174 74, 78, 79, 80, 81, 88, 89

Trujillo, I., Burkert, A., & Bell, E. F. 2004, ApJL, 600, L39 10, 85

van den Bosch, F. C., Aquino, D., Yang, X., Mo, H. J., Pasquali, A., McIntosh, D. H., Weinmann, S. M., & Kang, X. 2008, MNRAS, 387, 79 63

van der Marel, R. P. & van Dokkum, P. G. 2007, ApJ, 668, 756 52

van Dokkum, P. G. 2008, ApJ, 674, 29 55

van Dokkum, P. G. & Franx, M. 2001, ApJ, 553, 90 61, 62

van Dokkum, P. G., Franx, M., Kelson, D. D., Illingworth, G. D., Fisher, D., & Fabricant, D. 1998, ApJ, 500, 714 62, 68

van Dokkum, P. G. & van der Marel, R. P. 2007, ApJ, 655, 30 74, 75, 76, 78

White, S. D. M. & Rees, M. J. 1978, MNRAS, 183, 341 2, 3

Worthey, G. 1994, ApJS, 95, 107 5, 24